Puffs turbulents en conduites carrées : rayonnement acoustique et effets de courbure

Leonardo Rigo

HESAM UNIVERSITÉ

Arts et Métiers Sciences et Technologies

ÉCOLE DOCTORALE SCIENCES ET MÉTIERS DE L'INGÉNIEUR
Laboratoire Dynfluid - Campus de Paris

THÈSE

présentée par : **Leonardo Rigo**
soutenue le : **16 Novembre 2020**

pour obtenir le grade de : **Docteur d'HESAM Université**

préparée à : **École Nationale Supérieure d'Arts et Métiers**
Spécialité : **Mécanique**

Turbulent puffs in square duct flow: acoustic radiation and effects of curvature

THÈSE dirigée par : Xavier Gloerfelt
et co-encadrée par : Damien Biau

Jury

M.	**Régis MARCHIANO**	Professeur, Sorbonne Université	Président
Mme	**Laurette TUCKERMAN**	Directeur de Recherche, CNRS	Rapporteure
M.	**Christophe SCHRAM**	Professeur, VKI	Rapporteur
M.	**Yohann DUGUET**	Chargé de Recherche, LIMSI	Examinateur
M.	**Xavier GLOERFELT**	Professeur, ENSAM	Examinateur
M.	**Damien BIAU**	Maître de Conférences, ENSAM	Examinateur

THÈSE

Il est très difficile d'établir si quelque chose est vraie,
il est plus facile d'établir si quelque chose est fausse.
Et alors le faux c'est une façon de s'approcher à la vérité.

Umberto Eco

Acknowledgments

Je souhaite remercier tous les membres du jury pour avoir accepté d'évaluer mon travail, j'espère vivement que sa lecture ait été la plus agréable possible. Je tiens à remercier mes directeurs de thèse Xavier et Damien. Merci pour m'avoir fait confiance alors que j'étais juste un jeune plein d'espoir avec une idée vague de ce qu'était la recherche scientifique. Merci Damien pour les longues discussions, pour les idées, la collaboration et surtout pour la patience.

Un grand merci à tout le laboratoire pour les nombreux moment conviviaux et les pauses cafés, votre compagnie a rendu le travail beaucoup plus agréable pendant ces 3 ans. Merci à la tribu des doctorants pour les discussions, les blagues et les bières, j'espère vous revoir tous au Papagallo, mais plus de Chouffe! Un merci spécial à Cosimo pour le soutien et les longues discussions. Avoir partagé les moments de désespoir, qui ont été nombreux, a été indispensable pour ma santé mentale.

Grazie a Massimo, mamma e papà, lontani ma presenti nell'incoraggiarmi e farmi credere nel futuro, con delle belle parole e qualche incoraggiamento gastronomico. Speriamo di vederci presto a Parigi, Monaco o ancora meglio in Selvis. Infine, un enorme grazie a Viviana. Per avermi appoggiato, anche con fatica, nella mia scelta di lasciare l'Italia, per aver sopportato i momenti difficili con determinazione e per avermi tenuto i piedi a terra mentre guardavamo lontano insieme.

Résumé

L'apparition de la turbulence dans une conduite à faible nombre de Reynolds se localise sous la forme de *puffs* turbulents. Dans la littérature, les *puffs* sont classiquement étudiés dans des conditions nominales, qui correspondent à un écoulement incompressible dans une conduite droite de section circulaire. Cette thèse vise à étudier l'influence de faibles variations par rapport à ces conditions nominales. En particulier, on considère une conduite de section carrée et on introduit une faible courbure d'une part et on étudie le rayonnement acoustique d'autre part. Dans une première partie les caractéristiques du *puff* dans une conduite carrée sans courbure et sans effet de compressibilité sont présentées. Dans une seconde partie, les effets de courbure sont analysés à partir d'un modèle d'équations obtenu par une analyse dimensionnelle. Le modèle est validé pour des écoulements laminaires; les comparaisons par rapport à des données numériques et expérimentales de la littérature sont satisfaisantes. Le *puff* turbulent est calculé en utilisant deux systèmes d'équations couplés basés sur une séparation d'échelles. Les caractéristiques du *puff* turbulent sont qualitativement en accord avec les données publiées. Enfin, le bruit en champ lointain généré par le *puff* est calculé à l'aide d'une analogie acoustique, ce qui permet d'exclure un rôle possible de l'acoustique dans l'interaction à grande échelle entre les *puffs*. Cette étude fournit par ailleurs des résultats sur le rôle des contraintes visqueuses dans la génération de bruit. Cette configuration est en effets un cas très bien posé, car les effets des composantes visqueuses sur l'acoustique sont mieux visibles à faibles nombres de Mach et de Reynolds.

Keywords : puff turbulent, intérmittence, aéroacoustique, canal courbé

Abstract

The first occurrence of turbulence at low Reynolds number in pipe flows takes the form of streamwise localised patches named turbulent puffs. In the literature puffs are usually studied in the nominal conditions of incompressible flow in straight circular pipes. This thesis aims at investigating the influence that slight deviations from those nominal conditions have on puffs computed in a square duct configuration. For this purpose we introduce a slight curvature of the pipe on the one hand and we analyse the acoustic field of the puff on the other hand. Curvature effects are analysed by means of a laminar model obtained as an extension of the work by Dean. This model is validated against numerical and experimental literature data, providing satisfactory results. The turbulent puff in a curved pipe is computed with an additional set of equations based on scale separation, the curvature effects on turbulence are in qualitative agreement with the data available in the literature. The far-field noise field generated by a puff is computed by means of an acoustic analogy, in addition to characterising the acoustic field produced, this analysis excludes a role of acoustics in a hypothetical long range interaction between puffs. Moreover this study provides some elements to the literature concerning the role of the viscous stresses to the sound generation. This configuration provides a very well posed case for such analysis, since the effects of viscous stresses on acoustics are most visible at low Mach and Reynolds numbers.

Keywords: turbulent puffs, intermittency, aeroacoustics, curved duct

Sommario

La prima manifestazione della turbolenza in un condotto a basso numero di Reynolds è localizzata in zone turbolente (*puff*) separate da regioni laminari. In letteratura i *puff* sono sovente studiati nelle condizioni nominali di flusso incomprimibile, in tubi dritti, spesso di sezione circolare. Questa tesi ha come obiettivo l'analisi dell'influenza di lievi deviazioni rispetto alle condizioni nominali, in particolare consideriamo un condotto di sezione quadrata introducendo in primo luogo una piccola curvatura, analizzando successivamente la radiazione acustica. Nella prima parte presentiamo le caratteristiche di un *puff* turbolento in un canale quadrato senza curvatura e senza effetti di comprimibilità. Nella seconda parte si analizzeranno gli effetti della curvatura a partire da un modello di equazioni ottenuto da un'analisi dimensionale. Il modello sarà validato per flussi laminari rispetto a dati numerici e sperimentali di letteratura. Il *puff* in un canale curvo è calcolato utilizzando due sistemi di equazioni accoppiati basati su una separazione di scale, le caratteristiche della turbolenza sono qualitativamente in accordo con i dati disponibili. Infine, si calcolerà il rumore generato dal *puff* tramite un'analogia acustica, questa analisi permette di escludere un possibile ruolo dell'acustica nella comunicazione tra *puff* a lunga distanza, inoltre questo studio fornisce degli elementi che riguardano il ruolo del tensore degli sforzi viscosi nella generazione di rumore. Questa configurazione infatti è un caso molto ben posto, poichè gli effetti delle componenti viscose sull'acustica acquistano maggiore importanza a bassi numeri di Mach e di Reynolds

Contents

Chapter 1

Introduction

Table of contents of this chapter

The transitional flow in a pipe

The laminar flow in a pipe is linearly stable for any value of the Reynolds number $Re = U_b h/\nu$ both for round (Drazin and Reid, 1981) and square cross sections (Tatsumi and Yoshimura, 1990). This scenario is particular and radically differentiates this configuration from other problems, such as the Taylor-Couette flow between two co-rotating cylinders Taylor (1923), in which for a sufficiently large Re turbulence emerges via a series of bifurcations following the route to turbulence proposed by Ruelle and Takens (1971). In these cases a critical Reynolds number exists. Once past this value any perturbation starts a process that eventually leads to turbulence. In the pipe case transition is always subcritical, and cannot be triggered via a bifurcation cascade initiated by an infinitesimal perturbation. A sufficiently strong finite amplitude disturbance is required to "jump" to the turbulent manifold, even at very large Reynolds numbers. Nonetheless the Reynolds number plays a key role in turbulence transition in pipes, determining the evolution of the disturbed flow. In fact Reynolds (1883) himself reported the existence of intermittent turbulent regions, that he called 'flashes'. These

turbulent spots traveled downstream along the pipe and, provided that the flow parameter (that was later named the Reynolds number Re by Sommerfeld (1908)) was large enough, they grew in size to eventually fill the whole pipe with turbulence. Thus, depending on the Reynolds number, a finite amplitude disturbance applied locally in space and time to an otherwise laminar pipe flow can bring about three different scenarios. The threshold for the critical Reynolds was estimated by Reynolds himself, yet it was not until the remarkable work by the group of Hof (Avila et al., 2011) that the critical value of Re was established. For very low Re the excitation, if at all transmitted to the fluid parcels not directly forced, produces at best a non self-sustained local turbulent patch that is promptly dissipated. For high Re a finite disturbance gives rise to a self sustained turbulent region that expands to occupy the whole domain. The expanding turbulent region is named slug after Lindgren (1969). The high and low Re scenarios are sketched in figure 1.1. In an intermediate regime we have the formation of a self sustained turbulent patch that does not have a tendency to grow in size and is transported downstream with the flow bulk velocity. Wygnanski and Champagne (1973) called this spot of turbulence the turbulent puff.

Spatio-temporal intermittency in shear flows

Spatio temporal intermittency is not limited to pipe flow, in fact it is a key ingredient of transition to turbulence in wall bounded flows, when this occurs via a subcritical process. This condition is always verified in pipe flow, but can be found in other configurations such as plane Couette, counter-rotating Taylor-Couette or plane Pouiseuille flows, if the transition occurs at a Reynolds number where the flow is linearly stable. These configurations differ from the square duct flow by one main feature, i.e. the presence of one additional homogeneous direction. Takeishi et al. (2015) performed direct numerical simulations of localised turbulence in a rectangular duct of cross-sectional aspect ratio ranging from one (square duct) to 9. For the square duct case, they found a Reynolds number Re=1460 as the lowest value to observe a transiently sustained turbulent puff. Moreover, they observed the transition between puffs and spots for aspect ratios around 4. For very high aspect ratios a turbulent spot evolves to form a banded pattern, in which the turbulent bands are oriented along a direction tilted of an angle dependent on Re, or as shown in figure 1.2, along the two axes oriented with two opposite directions. The first observation of such stripes is due to Coles (1965); Coles and Van Atta (1966), who observed a helical turbulent state in Taylor Couette flow. Much later Prigent et al. (2003) observed a periodic

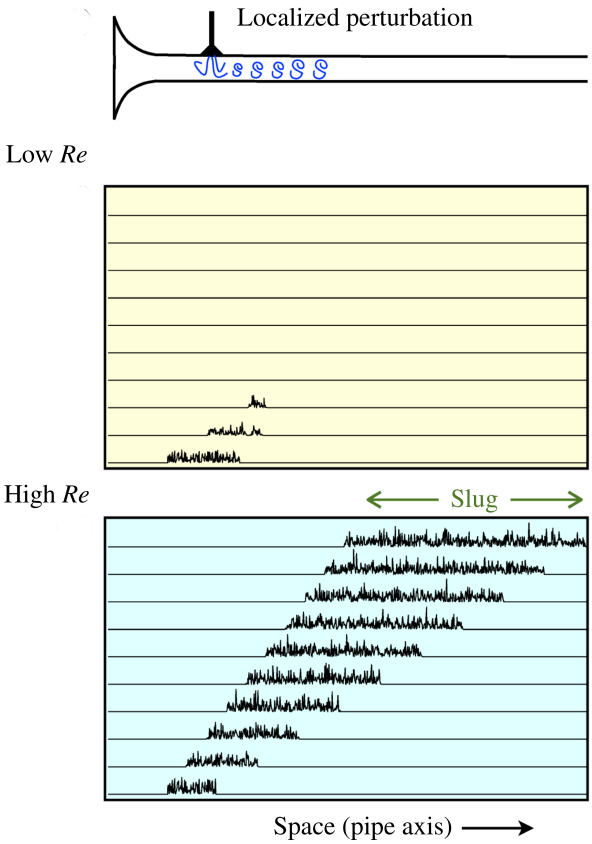

Figure 1.1: Sketch of the high and low Re response of an initially laminar pipe flow when an instantaneous, localised perturbation is applied. Adapted from Barkley (2016).

pattern of stripes, which only appears when the aspect ratio is very large. The large domain required to observe such phenomenon makes DNS a possible but costly tool, also because of the large spacing between the stripes, that are easily affected by the periodic boundary conditions in the streamwise and spanwise direction (if the computational domain is not large enough). A solution to this issue consists in aligning the computational domain not along the streamwise direction, but along a direction perpendicular to the stripes. This technique brings considerable savings in computational costs, and allowed the first DNS of such flow (Barkley and Tuckerman, 2005). Chantry et al. (2016) showed that a very similar effect is obtained in the Waleffe flow configuration, which is a free shear flow with a sinusoidal forcing that results in the generation of a shear layer at the center of the domain, as in Plane Couette flow. The domain tilting method however forces the flow to choose one direction of the turbulent stripes. The more straightforward, but computationally expensive technique is that of using a much larger domain aligned with the streamwise direction. In this case Duguet et al. (2010a)

observed a competition between the two equi-tilted directions, see figure 1.2. A reason for the existence of the angle is provided by Duguet and Schlatter (2013), who observed a non zero spanwise velocity component of the large scales. The small scale streamwise fluctuations are transported accordingly, resulting in a tilted development of the turbulent patches. For a much more extensive review on intermittency in wall bounded flows see Tuckerman et al. (2020).

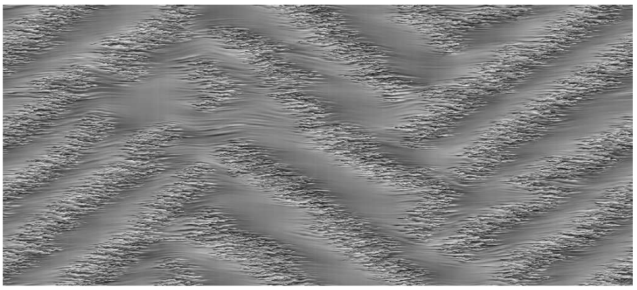

Figure 1.2: Center-plane, streamwise velocity field of Plane Couette Flow at $Re = 330$, adapted from Duguet et al. (2010a)

Turbulent puffs: the self-sustaining mechanism

Turbulence in wall bounded flows is able to self sustain via a mechanism proposed by Waleffe (1997). The formation of streamwise rolls generates an imbalance in the spanwise distribution of streamwise velocity, giving rise to streaks of low streamwise velocity near the walls. This generates a wake-like instability that results in the formation of three dimensional fluctuations. These grow in intensity to eventually produce non linear effects, one of which is that of re-energizing the streamwise rolls, closing the loop. The streaks are homogeneous in this description, thus the process cannot be directly transferred to the turbulent puff case, which is localised in the streamwise direction. Nonetheless Bandyopadhyay (1986) showed the presence of low speed streaks in the case of a turbulent puff in a pipe. These are commonly formed in wall turbulence and in this specific case they are observed only in correspondence of the turbulent core of the puff. Puffs move downstream with approximately the flow bulk velocity U_b (Wygnanski et al., 1975; Song et al., 2017). A low speed streak therefore is slower, and gradually moves towards the upstream front of the puff. Eventually a low speed streak encounters the upcoming laminar flow, giving rise to a localised shear layer and a shear instability similar to the Kelvin-Helmholtz (KH) instability. The roll ups formed are lifted towards the region close to the centerline, in which the velocity is higher than U_b. From the upstream front they are

thus transported downstream towards the puff core (Shimizu and Kida, 2009; Duguet et al., 2010b) and they eventually decay forming the turbulent region of the puff. The turbulence generated in this process is not capable of triggering the downstream fluid to transition due to the low Re; we have thus a very abrupt upstream front where turbulence is rapidly generated by the aforementioned mechanism, followed by a long region in which the turbulence generated is slowly dissipated, the downstream front. The formation of inflectional regions and KH vortices is intermittent, both in time and space. The generation of vortices never occurs in a contemporaneous fashion on the four walls, but rather at different times on different walls. Bandyopadhyay (1986) observed that for puffs in circular pipes the axisymmetric KH instability is never observed. This mechanism is somewhat similar to that proposed by Waleffe (1997) for sustained turbulence, with the specificity that the different phases occur in different areas of the flow, and the process is not continuous. Puffs are turbulent objects living on the edge of relaminarisation; a too long time without the generation of a suitable streak in the right spot, or a insufficiently clean laminar inflow can bring a sudden stop to the self sustaining process, determining the death of the puff. The life or death probability of puffs is strongly influenced by Re: for low Reynolds numbers the probability of relaminarisation is quite high whereas for slightly higher Re puffs tend to survive for long times (De Lozar and Hof, 2009).

Puffs and slugs: upstream and downstream fronts

The upstream front of a puff or a slug is sharp. This is linked to the subcriticality of the Hagen-Poiseuille flow: the two states (laminar and turbulent) are both possible and this makes that the upcoming laminar flow jump onto the turbulent branch thanks to the disturbance provided by the existence of the puff itself. It is common to call this kind of front a strong front, as opposed to the long, dissipative downstream front typical of puffs, that is called weak (Barkley et al., 2015). The downstream front of a slug can be strong or weak, depending on the Reynolds number (Duguet et al., 2010b). For low Re the front is weak, as for the puff, the disturbance produced is however able to trigger turbulence and the front gently propagates downstream, expanding the slug (see figure 1.3). In the case of puffs the downstream region shows a refractoriness towards turbulence. The generation of turbulence at the upstream front extracts too much energy from the mean flow, which is more blunt than the Hagen Poiseuille profile and is therefore no longer receptive. This is also the reason why when two puffs are placed too close together, the second tends to move away from the first, and in

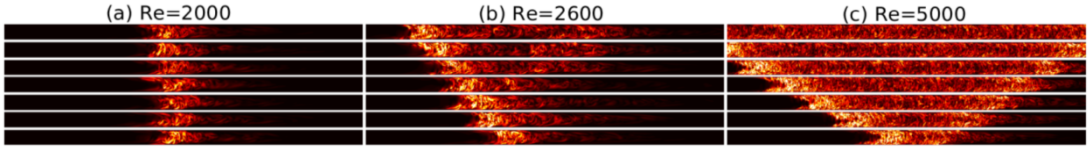

Figure 1.3: Contours of the turbulent fluctuations in round pipe flow for $Re = 2000, 2600, 5000$, adapted from Song et al. (2017). Frame of reference moving with the flow bulk velocity. The puff holds a constant length, whereas the slugs expands both upstream and downstream, for high Re both the upstream and downstream fronts are of the strong kind.

the process it presents lower energy levels (Mukund and Hof, 2018). Hof et al. (2010) exploited this mechanism to cause the relaminarisation of the flow in a pipe by supplying a constant perturbation. Shimizu and Kida (2009) observed that the roll ups formed in the upstream shear layer traveled faster than the puff velocity, eventually entering the turbulent region. This, together with the refractoriness of the flow along the downstream front leads to the formation of a constant sized puff. Duguet et al. (2010b) observed that for higher Re some of the vortices are transported downstream with velocities lower than that of the core turbulence. This results in an upstream movement of the front; the slug expands both upstream and downstream (in the moving frame of reference).

Puff sensitivity

The dependence of puff survival on the flow conditions is not trivial. Hof et al. (2010) showed that supplying additional turbulence may deform the base velocity profile, provoking immediate relaminarisation of a puff. In the following other studies used different methods to eliminate turbulence in pipes, such as wall movement (Kühnen et al., 2018) or a baffle (Kühnen et al., 2019; Ding et al., 2020) to eliminate even high Reynolds turbulence. As also pointed out by Trefethen et al. (1993) in the linear stability framework, very slight changes in the flow condition may provoke considerably large scale effects. This is why we investigate the influence of curvature and low Ma compressibility (acoustics). Many other effects may be considered, such as buoyancy due to temperature gradients or vibrations. These effects have not been analysed in the thesis and will be briefly discussed in the conclusion.

Organisation of the manuscript

The manuscript is divided into 3 main chapters. After this introduction, chapter 2 is concerned with the study of turbulent puffs in nominal conditions. The first part of the chapter gives the numerical details of the simulation of a puff in a straight duct of square cross section, while the second part contains some of the results of the computations. Along with presenting some classic and some new analyses, this part will hopefully allow the reader to better understand the particular features of turbulent puffs. Chapter 3 focuses on the analysis of the flow in a weakly curved duct. After a literature review we present a weak curvature model that is initially used to perform a study on the laminar flow in a bent duct. In the last part of the chapter we study the response of the puff when subjected to a weak curvature of the pipe. Chapter 4 concerns the study of the acoustic field produced by a puff. After a literature review and a theoretical and numerical introduction, we provide a characterisation of the far field noise generated by a puff. The last part of the chapter focuses on the role of the wall viscous stresses in sound generation.

Chapter 2

Turbulent puffs in a square duct: nominal conditions

Table of contents of this chapter

Equations and Numerics

We present here the equations that govern the nominal case of an incompressible flow in a straight duct of infinite length, with the details about the numerical solution. In the following chapters the equations will be modified to account for a small curvature (chapter 3) and for compressibility, more specifically computing the acoustic radiation of the puff (chapter 4). In the classical case the flow is governed by the Reynolds number, additional flow features are represented in the equations by new non dimensional quantities, namely the Dean number for curvature and the Mach number for acoustics.

Conservation equations

The flow in a duct is governed by the Navier Stokes equations. For relatively low speeds ($Ma < 0.3$) the compressibility effects have little influence on the hydrodynamic flow field and can be neglected, obtaining the incompressible form of the Navier-Stokes equations. The continuity and momentum equations in their dimensional form (indicated by the superscript *) read

$$\frac{\partial u^*}{\partial x^*} + \frac{\partial v^*}{\partial y^*} + \frac{\partial w^*}{\partial z^*} = 0 \tag{2.1a}$$

$$\frac{\partial u^*}{\partial t} + u^*\frac{\partial u^*}{\partial x} + v^*\frac{\partial u^*}{\partial y} + w^*\frac{\partial u^*}{\partial z} = -\frac{1}{\rho}\frac{\partial p^*}{\partial x} + \frac{1}{\nu}\left(\frac{\partial^2 u^*}{\partial x^2} + \frac{\partial^2 u^*}{\partial y^2} + \frac{\partial^2 u^*}{\partial z^2}\right) \tag{2.1b}$$

$$\frac{\partial v^*}{\partial t} + u^*\frac{\partial v^*}{\partial x} + v^*\frac{\partial v^*}{\partial y} + w^*\frac{\partial v^*}{\partial z} = -\frac{1}{\rho}\frac{\partial p^*}{\partial y} + \frac{1}{\nu}\left(\frac{\partial^2 v^*}{\partial x^2} + \frac{\partial^2 v^*}{\partial y^2} + \frac{\partial^2 v^*}{\partial z^2}\right) \tag{2.1c}$$

$$\frac{\partial w^*}{\partial t} + u^*\frac{\partial w^*}{\partial x} + v^*\frac{\partial w^*}{\partial y} + w^*\frac{\partial w^*}{\partial z} = -\frac{1}{\rho}\frac{\partial p^*}{\partial z} + \frac{1}{\nu}\left(\frac{\partial^2 w^*}{\partial x^2} + \frac{\partial^2 w^*}{\partial y^2} + \frac{\partial^2 w^*}{\partial z^2}\right) \tag{2.1d}$$

where ρ and ν indicate the fluid density and kinematic viscosity. The non dimensionalisation is performed using the bulk velocity U_b and the duct side length h as the reference velocity and length. Both the non dimensional bulk velocity $U_b = \iint_{y,z} u^* dydz$ (x is the streamwise direction) and h are unitary. The non dimensional variables are

$$u, v, w = \frac{u^*, v^*, w^*}{U_b} \qquad p = \frac{p^*}{\rho U_b^2} \qquad t = \frac{t^* U_b}{h} \qquad x, y, z = \frac{x^*, y^*, z^*}{h} \tag{2.2}$$

h indicates the duct side length (with constant value 1) and ρ is the fluid density. In their non dimensional form the equations read

$$\frac{\partial u}{\partial x} + \frac{\partial v}{\partial y} + \frac{\partial w}{\partial z} = 0 \tag{2.3a}$$

$$\frac{\partial u}{\partial t} + u\frac{\partial u}{\partial x} + v\frac{\partial u}{\partial y} + w\frac{\partial u}{\partial z} = -\frac{\partial p}{\partial x} + \frac{1}{Re}\left(\frac{\partial^2 u}{\partial x^2} + \frac{\partial^2 u}{\partial y^2} + \frac{\partial^2 u}{\partial z^2}\right) \tag{2.3b}$$

$$\frac{\partial v}{\partial t} + u\frac{\partial v}{\partial x} + v\frac{\partial v}{\partial y} + w\frac{\partial v}{\partial z} = -\frac{\partial p}{\partial y} + \frac{1}{Re}\left(\frac{\partial^2 v}{\partial x^2} + \frac{\partial^2 w}{\partial y^2} + \frac{\partial^2 w}{\partial z^2}\right) \tag{2.3c}$$

$$\frac{\partial w}{\partial t} + u\frac{\partial w}{\partial x} + v\frac{\partial w}{\partial y} + w\frac{\partial w}{\partial z} = -\frac{\partial p}{\partial z} + \frac{1}{Re}\left(\frac{\partial^2 w}{\partial x^2} + \frac{\partial^2 w}{\partial y^2} + \frac{\partial^2 w}{\partial z^2}\right) \tag{2.3d}$$

The Reynolds number Re is defined as

$$Re = \frac{U_b h}{\nu} \tag{2.4}$$

Boundary conditions

The momentum equations in 2.3 are elliptic PDEs; this will change in chapter 3, where we will use a different non dimensionalisation to neglect some of the terms of the NS equations. This will result in a set of parabolic PDEs (parabolic in the streamwise direction), decreasing the number of boundary conditions (BCs) required in that direction from two to one.

Concerning the velocity components the BC is the no-slip condition on the walls $u_i = u_{y,z=0} = u_{y,z=1} = 0$, while pressure is represented with a lower order polynomial (which will result in less Chebyshev points for the pressure grid) and no boundary condition is required (Botella, 1997).

In the streamwise direction we impose a periodic boundary condition, allowing the use of the Fourier transform. Periodic boundary conditions are not always transposable to real configurations (some counterexamples exist, such as turbomachines) yet in many applications periodicity is a powerful feature. For a memoryless process like turbulence the presence of periodicity allows the computation of sustained turbulence on a shorter domain, if compared to a case where the flow is randomly excited at the inflow. In the case of a turbulent puff, periodicity is also justified by the localisation; for a sufficiently long domain both the inflow and the outflow are (quasi) laminar. Physically, periodicity implies the presence of a train of identical puffs, set at an equal distance from each other.

Initial condition

The numerical representation of a transitional phenomenon such as the turbulent puff is deeply affected by the initial condition. The subcriticality of the problem implies that both the laminar and turbulent solutions can exist and the result depends on the perturbation intensity. For weak disturbances the flow eventually returns to the laminar state, whereas for strong enough perturbations it can transition. For intermediate Reynolds numbers however the turbulent state is different with respect to the generalised turbulence case, since turbulence exists only in patches separated by laminar regions. The laminar region upstream of a turbulent patch (puff) is vital for its existence. Kühnen et al. (2018) showed that forcing a basal level of turbulence in a pipe impedes the self sustaining process of puffs, resulting in a laminar flow. The initial condition required to obtain a turbulent puff is thus not only one in which the perturbation with respect to the laminar state is sufficiently strong, the shape of the disturbance also plays a critical role. Duguet et al. (2010b) computed the shape

of the edge states for slug genesis in pipe flow, which are localised in 3D, even if the final state is generalised turbulence. Obtaining a turbulent puff from scratch is a time consuming task. One can start from a laminar solution with an added random noise. This however will not always evolve to form a turbulent puff, most of the times the flow will re-laminarise. In an experimental case an initial random perturbation would probably give rise to a number of puffs along the pipe. Numerically we normally simulate a single puff and the odds that it forms and survives after the imposition of a random initial condition are dim. In practice, after imposing the initial condition one should closely look after the flow evolution, artificially increasing the fluctuations levels when the flow tends to become laminar. Another methodology consists in starting from a fully turbulent simulation and slowly decreasing the Reynolds number. At each step the simulation must be run until a statistically steady state is reached, a too steep decrease of Re would result in sudden relaminarisation. If the flow does not relaminarise, this process results in a localisation of turbulence, i.e. in a turbulent puff. Once an initial condition with a puff is available the process described above is no longer required. One may use the existing turbulent puff as the initial condition, saving a great deal of time.

Numerical solution of the incompressible Navier-Stokes equations

The non dimensional incompressible Navier Stokes equations are solved using a pseudo-spectral method that takes advantage of the Fourier transform in the streamwise direction, and uses Chebyshev collocation in the cross stream directions. The divergence free condition is enforced by means of the prediction-projection method and the time integration is performed using a 4^{th} order backward differentiation scheme. In this chapter we will provide details about each of these concepts.

Time discretisation

The momentum equations of (2.3), with the time derivative discretized on a 5 time-points stencil, and written in Einstein notation for brevity, become

$$\left(\frac{a_1}{\Delta t} - \frac{1}{Re}\frac{\partial^2}{\partial x_j^2}\right)u_i^n = \\ -\frac{1}{\Delta t}\left(a_2 u_i^{n-1} + a_3 u_i^{n-2} + a_4 u_i^{n-3} + a_5 u_i^{n-4}\right) - \frac{\partial p}{\partial x_i} + u_j\frac{\partial u_i}{\partial x_j} \tag{2.5}$$

We see here that we have a semi-implicit method: the time derivative and the viscous term are solved implicitly, whereas the non-linear term is left on the right hand side of the equation. The superscript n

indicates the solution at the present time-step, $n-1$ at the last time-step, and so on. The coefficients a_i used to weigh the solutions at the previous times are the classic finite difference coefficients for a regular grid centered at $n = 1$:

$$a_1 = \frac{25}{12} \quad a_2 = -4 \quad a_3 = 3 \quad a_4 = -\frac{4}{3} \quad a_5 = \frac{1}{4}$$

The velocities used to compute the non-linear term are extrapolated from the previous time-steps solutions using a 3^{rd} order extrapolation, whereas pressure is extrapolated with a 2^{nd} order extrapolation. This to improve the overall stability of the scheme, as pointed out by Botella (1997).

This equation is not used as is, but after performing a Fourier transform in the streamwise direction. For clarity we will write explicitly the 3 derivatives of a given velocity field $\widehat{u}_i$ (the superscript indicates the fact that it is expressed in Fourier space).

$$\left(\frac{a_1}{\Delta t} - \frac{1}{Re}\left(\frac{\partial^2}{\partial y^2} + \frac{\partial^2}{\partial z^2} - k^2\right)\right)\widehat{u}_i^n = \\ -\frac{1}{\Delta t}\left(a_2\widehat{u}_i^{n-1} + a_3\widehat{u}_i^{n-2} + a_4\widehat{u}_i^{n-3} + a_5\widehat{u}_i^{n-4}\right) - \frac{\partial \widehat{p}}{\partial x_i} + \widehat{u_j\frac{\partial u_i}{\partial x_j}} \tag{2.6}$$

The derivative in the streamwise direction has become a multiplication by the square of the wavenumber k because $(ik)^2 = -k^2$. The right hand side of the equation can be calculated using the solutions at the previous timesteps and the derivatives of the extrapolated velocity and pressure fields, using the Chebyshev differentiation matrices for the cross-stream directions and the Fourier transform in the streamwise direction (see sections 2.1.5.1 and 2.1.5.6). The multiplications needed to compute the nonlinear term are performed in the physical space, and the result is subsequently Fourier transformed. A multiplication in physical space corresponds to a convolution in Fourier space, that is more expensive than performing the inverse Fourier transform, multiplying in physical space and re-transforming. Equation (2.6) is a Helmholtz equation. The solution of this problem in a Chebyshev collocation framework is given in section 2.1.5.3.

The flow is forced to maintain a streamwise bulk velocity $U_b = 1$. This condition is enforced by adding to the 0 mode of the streamwise component of velocity a pressure gradient that corrects any deviation from $U_b = 1$. This pressure gradient is not linked with the hydrodynamic pressure gradient $\frac{\partial p}{\partial x_i}$, we call it $\frac{\partial P}{\partial x}$ (with the capital letter). The correct pressure gradient is found by means of an iterative method that consists in recursively solving the Helmholtz problem for the zero mode while adapting the $\frac{\partial P}{\partial x}$. The streamwise bulk velocity error can be contained close to machine precision.

Enforcing the divergence free condition. The prediction projection method

The incompressible Navier Stokes equations are composed of 4 equations for 4 unknowns, however the 3 momentum equations are decoupled from the continuity equation, which does not contain p, and therefore cannot be used to compute it. In order to enforce the divergence free condition and find a pressure field whose gradient is compatible with the velocity field we use a method very similar to the prediction-projection by Chorin-Temam (Chorin, 1968; Temam, 1968). We use for clarity a first order explicit Euler scheme in the following equations ($a_1 = 1$, $a_2 = -1$), the same considerations stand for higher order temporal schemes explicit or implicit. We can write two equations:

$$\frac{a_1 \tilde{u}_i^n + a_2 u_i^{n-1}}{\Delta t} = -\frac{\partial p^{n-1}}{\partial x_i} + rhs$$
$$\frac{a_1 {u_i}^n + a_2 u_i^{n-1}}{\Delta t} = -\frac{\partial p^n}{\partial x_i} + rhs$$

We can solve the first using the pressure field of the last iteration, the solution $\tilde{u}_i^n$ is compatible with the boundary conditions, but does not respect the divergence free condition. This step is called the prediction step. The second equation contains the solution u_i^n computed with the updated pressure field p^n. This solution is divergence free, but does not explicitly respect the boundary condition. Moreover we do not yet have access to the updated pressure field, thus we cannot calculate u_i^n. If we subtract the second to the first we have

$$a_1 \frac{\tilde{u}_i^n - u_i^n}{\Delta t} = \frac{\partial (p^n - p^{n-1})}{\partial x_i} \tag{2.7}$$

taking the divergence of the result we obtain

$$\frac{\partial^2 p^n}{\partial x_i^2} = \frac{\partial \tilde{u}_i^n}{\partial x_i} + \frac{\partial^2 p^{n-1}}{\partial x_i^2}$$

from which we can retrieve the updated pressure field

$$p^n = \iiint_V \frac{a_1}{\Delta t} \frac{\partial \tilde{u}_i^n}{\partial x_i} + \frac{\partial^2 p^{n-1}}{\partial x_i^2} dV \tag{2.8}$$

that we can now inject in (2.7) to find the projected velocity field u_i^n. This method is very similar to the one originally proposed by Chorin and Temam, the only difference being that we include p^{n-1} in the projection step, to improve the accuracy of the scheme. Another improvement in accuracy comes from modifying the pressure p^{n-1} in (2.8) into

$$p^{n-1} - \frac{1}{Re} \frac{\partial \tilde{u}_i^n}{\partial x_i}$$

A comprehensive review of these and other projection methods is provided in Guermond et al. (2006).

Spatial discretisation

The Chebyshev collocation scheme

We take a 2D square grid of side ranging from -1 to 1, with $N+1$ grid points per side. The grid points are placed in correspondence of the Chebyshev nodes

$$y_i = cos\left(\frac{i\pi}{N}\right) \qquad z_j = cos\left(\frac{j\pi}{N}\right)$$

with $i, j = 0, 1, ..., N$. Following Trefethen (2000) we can define a matrix D such that

$$\frac{\partial u}{\partial y} = D \cdot u$$

This reduces the operation to compute the derivative to a matrix multiplication that can be very rapidly performed using a linear algebra package (e.g. Lapack or MKL), also avoiding the use of for loops that are known to slow down Matlab or Python scripts. The downside of this method is that it makes it impossible to cut the domain into pieces for parallelisation purposes, since the stencil used to compute the derivative on a given point is as long as the computational domain. The entries of the differentiation matrix D are

$$\begin{aligned}
D_{00} &= \frac{2N^2+1}{6} \qquad & D_{NN} &= -\frac{2N^2+1}{6} \\
D_{jj} &= -\frac{x_j}{2(1-x_j^2)} \qquad & j &= 1, ..., N-1 \\
D_{ij} &= \frac{c_i}{c_j}\frac{(-1)^{i+j}}{x_i - x_j} \qquad & i \neq j \qquad & i, j = 1, ..., N-1
\end{aligned}$$

with

$$\begin{aligned}
c_i &= 2 \quad \text{for} \quad i = 0 \quad \text{or} \quad i = N \\
c_i &= 1 \quad \text{otherwise}
\end{aligned}$$

As for any finite difference stencil, the sum of the coefficients on a row of D should be zero. This condition is verified by (2.9) to the precision of the machine. The roundoff error, although very small, can accumulate. Bayliss et al. (1995) enforced this condition analytically by computing the values of the matrix on the diagonal as

$$D_{ii} = -\sum_{\substack{j=0 \\ j \neq i}}^{N} D_{ij}$$

which has also the advantage of being easier to implement. Once the differentiation matrix is found, we obtain the second derivative simply by squaring D:

$$\frac{\partial^2 u}{\partial y^2} = D_2 \cdot u = (D \cdot D) \cdot u$$

If we want to compute the derivative in the other direction (z) we should make the same coefficients multiply not the columns, but the rows of the velocity field u, hence:

$$\frac{\partial u}{\partial z} = u \cdot D^T$$

and for the second derivative

$$\frac{\partial^2 u}{\partial z^2} = u \cdot (D^T \cdot D^T) = u \cdot (D \cdot D)^T = u \cdot D_2^T$$

The velocity fields are approximated using $N+1$ points per side, hence with polynomials of order up to N on a $(N+1) \times (N+1)$ grid. The pressure field is approximated using lower order $N-2$ polynomials on a $(N-1) \times (N-1)$ grid. This produces a more stable solution avoiding the generation of spurious pressure fluctuations without the need of a second computational grid. It also means that we do not have access to the values of the pressure on the boundaries. The differentiation matrix for pressure is (Botella, 1997)

$$\begin{aligned} D_{ij}^p &= -\frac{1}{2} \frac{\sin^2\left(\frac{\pi j}{N}\right)}{\sin^2\left(\frac{\pi i}{N}\right)} \frac{(-1)^{i+j}}{\sin\left(\frac{\pi(i+j)}{2N}\right) \sin\left(\frac{\pi(i-j)}{2N}\right)} && \text{for } i \neq j,\ 1 \leq i,j \leq N-1 \\ D_{ij}^p &= \frac{3}{2} \frac{\cos\left(\frac{\pi i}{N}\right)}{\sin^2\left(\frac{\pi i}{N}\right)} && \text{for } i = j,\ 1 \leq i,j \leq N-1 \end{aligned} \tag{2.9}$$

Numerical treatment of the boundary conditions

We want to enforce a no-slip condition on the boundary in the non homogeneous directions:

$$u_0 = u_N = 0$$

This could be achieved simply by imposing the value $u = 0$ on the boundaries at each iteration. Another way to obtain the same result is to eliminate the first and last rows and columns of the whole problem: when computing a derivative in y the first and last element of each row of D is always multiplied by a value of u on the boundary, which is zero. Performing this calculation does not provide

any additional information, hence we can neglect the first and last columns of the matrix D. The first and last rows of the linear problem are used to compute the values of u on the boundary, which are 0 by hypothesis, hence we can neglect the first and last rows of D. What remains is a strictly equivalent problem of size $(N-1) \times (N-1)$. We should notice that this operation does not imply any loss of information, and we are left with a polynomial description of the velocity field of order N, with a grid of $(N-1)$ points per side, hence more information than the points should carry.

Pressure is instead approximated on a square of $(N-1)$ points per side, it is not defined on the physical boundaries and its value is not required in the calculation since the velocity field is imposed by the Dirichlet boundary condition; in the present case those points are not even explicitly stored.

Solution of a Helmholtz problem

The Helmholtz equation is the following

$$\left(\frac{\partial^2 u}{\partial x^2} - \alpha u\right) = f \tag{2.10}$$

with α, f scalars. The second derivative of the velocity (or pressure) field u is expressed in the Chebyshev collocation method as

$$\frac{\partial^2 u}{\partial x^2} = D_2 u$$

We can express (2.10) as

$$(D_2 u - \alpha I u) = f$$

or

$$(D_2 - \alpha I)u = f \tag{2.11}$$

D_2 is a linear operator whose eigenvalues Λ and eigenvectors Q satisfy the equation

$$D_2 Q = Q\Lambda \quad \text{or} \quad D_2 = Q\Lambda Q^{-1}$$

Λ is a diagonal matrix with the diagonal occupied by the eigenvalues of D_2. we can rewrite (2.11) as

$$Q(\Lambda - \alpha I)Q^{-1}u = f \tag{2.12}$$

We can now solve for $Q^{-1}u$, noticing that Λ and I are diagonal and therefore the inverse is simply obtained by inverting each element.

$$Q^{-1}u = Q^{-1}\frac{f}{(\Lambda - \alpha I)}$$

and finally

$$u = Q\left(Q^{-1}\frac{f}{(\Lambda - \alpha I)}\right) \tag{2.13}$$

further details on the method are found in Trefethen (2000); Haidvogel and Zang (1979); Haldenwang et al. (1984).

Double diffusion Helmholtz problem

We extend now the solution for a double diffusion problem written in the matrix form as

$$D_2 u + u D_2^T - \alpha I u = f \tag{2.14}$$

As above we determine the eigenvalues and eigenvectors of the operators, Q, Λ for D_2 and P, Γ for D_2^T.

$$\begin{aligned} D_2 &= Q\Lambda Q^{-1} & \Lambda Q^{-1} &= Q^{-1} D_2 \\ D_2^T &= P\Gamma P^{-1} & \Gamma P^{-1} &= P^{-1} D_2^T \end{aligned}$$

Following the procedure shown by Ehrenstein and Peyret (1989) we multiply (2.14) on the left by Q^{-1} obtaining

$$Q^{-1} D_2 u + Q^{-1} u D_2^T - Q^{-1}\alpha I u = Q^{-1} f$$

or

$$\Lambda(Q^{-1}u) + (Q^{-1}u)D_2^T - (Q^{-1}u)\alpha I = Q^{-1} f$$

and also

$$\left(Q^{-1}u\right)\left(\Lambda + D_2^T - \alpha I\right) = Q^{-1} f$$

We can now apply the same procedure used to obtain (2.13) to solve for $Q^{-1}u$ since Λ, I are diagonal.

$$\left(Q^{-1}u\right)\left(\Lambda + P\Gamma P^{-1} - \alpha I\right) = Q^{-1} f$$

can be written as

$$\left(Q^{-1}u\right) P\left(\Lambda + \Gamma - \alpha I\right) P^{-1} = Q^{-1} f$$

Multiplying on the right by P, $(\Lambda + \Gamma - \alpha I)^{-1}$ and P^{-1}, in this order, and then by Q on the left we obtain

$$u = Q\frac{Q^{-1} f P}{\Lambda + \Gamma - \alpha I} P^{-1} \tag{2.15}$$

3D diffusion with two inhomogeneous directions

The viscous term of the momentum equation (2.3) is composed by a double differentiation in the three directions multiplied by the inverse of the Reynolds number. The Helmholtz problem is

$$\left(-\frac{1}{Re}\left(\frac{\partial^2}{\partial y^2}+\frac{\partial^2}{\partial z^2}\right)+\frac{a_1}{\Delta t}+\frac{k^2}{Re}\right)\widehat{u}_i = rhs \tag{2.16}$$

The diagonal term is composed by the square wavenumber k^2 and the first coefficient of the backward differentiation scheme.

As we did above we express (2.16) in matrix notation using the Chebyshev operators

$$\left(-\frac{1}{Re}D_2\widehat{u}_i-\frac{1}{Re}\widehat{u}_i D_2^T\right)+I\left(\frac{a_1}{\Delta t}+\frac{k^2}{Re}\right)\widehat{u}_i = rhs$$

We make the following substitutions:

$$A=\frac{1}{Re}D_2 \qquad\qquad B=\frac{1}{Re}D_2^T$$

We have that

$$A=Q_A\Lambda_A Q_A^{-1} \qquad B=Q_B\Lambda_B Q_B^{-1}$$

Q_K, Λ_K being the respective eigenvectors and eigenvalues matrices. As in (2.15) the solution is

$$\widehat{u}_i = Q_A\frac{Q_A^{-1}rhsQ_B}{-\Lambda_A-\Lambda_B+I\left(\frac{a1}{dt}+\frac{k^2}{Re}\right)}Q_B^{-1} \tag{2.17}$$

FFT

When a problem is periodic it is often useful to treat it using the Fourier transform. This simplifies the computation of derivatives and makes them considerably faster compared to, say, a finite difference method, obtaining a higher (spectral) accuracy. This is linked to the fact that the stencil used to compute the derivatives in a given point is extended to the whole domain, whereas the rapidity is due to the fact that the differentiation is performed simply by multiplying each mode by its the wavenumber, without the need of accesssing other parts of the memory. Moreover due to the higher accuracy, less modes are needed. In a computational framework applying the Fourier transform results in performing the Discrete Fourier Transform (DFT). We consider a $3D$ field, $u(x,y,z)$ periodic in x.

$$\widehat{u}_k(y,z)=\sum_{n=0}^{N-1}u_n(y,z)e^{-\frac{i2\pi kn}{N}} \tag{2.18}$$

The $\widehat{\ }$ superscript indicates the Fourier transformed quantities, k is the wavenumber, N is the number of points in x. Conversely the inverse DFT

$$u_n(y,z) = \frac{1}{N}\sum_{n=0}^{N-1} \widehat{u}_k(y,z) e^{\frac{i2\pi kn}{N}} \tag{2.19}$$

In order to compute the DFT it is required to perform two nested loops, for n and k, which results in a number of computations of order $\mathcal{O}(N^2)$, in practice the Fourier transform is done using the Fast Fourier Transform (FFT), which reduces the number of operations to $\mathcal{O}(Nlog(N))$.

Dealiasing

The aliasing error introduced by the application of the Fourier transform is eliminated by using the zero-padding technique. In general the cutoff mode number is $K = N/2$, where N is the number of grid points. Zero padding consists in setting to zero all the mode numbers higher than K, hence half of the available modes. The high wavenumber terms are given by the non linear interactions between the modes. In the case of the Navier Stokes equations the only non-linearities are quadratic; Orszag (1971) pointed out that in order to cut-off all the non linear mode numbers higher than K it is sufficient to set to zero the highest 1/3 of the modes. This allows conspicuous savings in numerical resources, since the 2/3 of the computing points in the homogeneous direction are representative of a Fourier mode.

Change of coordinates

In the case of a turbulent puff it can be useful to have a frame of reference moving at the speed of the puff itself. Puffs move downstream roughly with the flow bulk velocity U_b (Wygnanski et al., 1975; Song et al., 2017).

We perform a substitution of the velocity u with a new velocity

$$\tilde{u} = u + U_b.$$

In the frame of reference co-moving with the bulk velocity, at the boundary we have

$$\tilde{u} = 0 \qquad \text{thus} \qquad u = -U_b$$

We write the momentum equations in (2.3) not as they appear but with the nonlinear term in all the momentum equations modified as follows

$$\frac{\partial u}{\partial t} + (u - U_b)\frac{\partial u}{\partial x} + v\frac{\partial u}{\partial y} + w\frac{\partial u}{\partial z} = -\frac{\partial p}{\partial x} + \frac{1}{Re}\left(\frac{\partial^2 u}{\partial x^2} + \frac{\partial^2 u}{\partial y^2} + \frac{\partial^2 u}{\partial z^2}\right) \tag{2.20a}$$

$$\frac{\partial v}{\partial t} + (u - U_b)\frac{\partial v}{\partial x} + v\frac{\partial v}{\partial y} + w\frac{\partial u}{\partial z} = -\frac{\partial p}{\partial y} + \frac{1}{Re}\left(\frac{\partial^2 v}{\partial x^2} + \frac{\partial^2 v}{\partial y^2} + \frac{\partial^2 v}{\partial z^2}\right) \tag{2.20b}$$

$$\frac{\partial w}{\partial t} + (u - U_b)\frac{\partial w}{\partial x} + v\frac{\partial w}{\partial y} + w\frac{\partial u}{\partial z} = -\frac{\partial p}{\partial z} + \frac{1}{Re}\left(\frac{\partial^2 w}{\partial x^2} + \frac{\partial^2 w}{\partial y^2} + \frac{\partial^2 w}{\partial z^2}\right) \tag{2.20c}$$

thus solving for $\tilde{u}$. It is crucial that the transformation is performed with a constant velocity, otherwise an acceleration term should be added.

We modified the equation and kept the same boundary condition, the flow computed has 0 velocity at the boundary and $2U_b$ at the laminar centerline. However the puff does not flow out of the computational domain, since we are in a reference frame moving with U_b.

The turbulent flow in a duct of square cross section

The square duct flow configuration has drawn considerable attention in the past, both because of its geometrical simplicity and for its presence in practical applications, such as ventilation systems, nuclear reactors, heat exchangers among others. One of the particular features of turbulence in square (or, more generally, rectangular) ducts is the presence of secondary motions in the cross stream plane, that were first reported by Prandtl (1927) and later by Nikuradse (1930). These appear as a cross stream flow directed towards the four angles, generating as well 4 pairs of counter rotating vortices. These structures are much less energetic than the bulk streamwise flow, but play an important role in redistributing friction and heat flux along the perimeter. For a comprehensive review on the literature on the secondary motions see Pirozzoli et al. (2018). For increasing Reynolds numbers the secondary motions occupy a smaller and smaller fraction of the section, being increasingly confined near the corner. The streamwise vorticity level instead increases with increasing Re, while the position of the maximum moves towards the corner.

The study of secondary motions is normally performed on high Re cases (Pinelli et al., 2010; Pirozzoli et al., 2018; Modesti et al., 2019), but the secondary motions are not only observed in high Re flows. Figure 2.1 shows the secondary motion pattern of a low Reynolds DNS ($Re = 1500$) in

which turbulence is present in the form of a turbulent puff. The left part of the figure shows the time and streamwise averaged field, in which the 8 vortices are clearly visible and occupy a large part of the section, which is consistent with the low Reynolds number of the flow. In the right part of the figure is the instantaneous, streamwise averaged pattern. The structures are visible, but are strongly distorted when compared to the classic 8 vortices pattern. Moreover we observe a stronger activity on the lateral walls, with stronger vortices generating a motion towards the center of the domain, almost absent in the vertical direction. This observation is compatible with the time history of the viscous stresses ($\tau = \mu \frac{\partial u}{\partial n}$, with n the wall normal direction) reported in figure 2.2, in which we clearly see that the wall shear stress strongly oscillates with time and the activity is highly variable from a wall to another, at a given time. Associated to this variation in activity among the walls is the time dependence of the global wall viscous stress, represented in figure 2.3 as the streamwise pressure gradient dP/dx required to ensure a unitary bulk velocity. It is worth pointing out that the instantaneous sum of the shear stresses at the walls is balanced by the streamwise pressure gradient (forcing). In our definition of τ we neglected the spanwise velocity gradients, which however marginally contribute to the total drag. From the time history in the left part of the figure one may guess a period of around 60 time units, compatible with the observation by Rinaldi et al. (2019) in the case of a slug at $Re = 3300$. The spectrum does not reveal such a frequency, a longer simulation may be required.

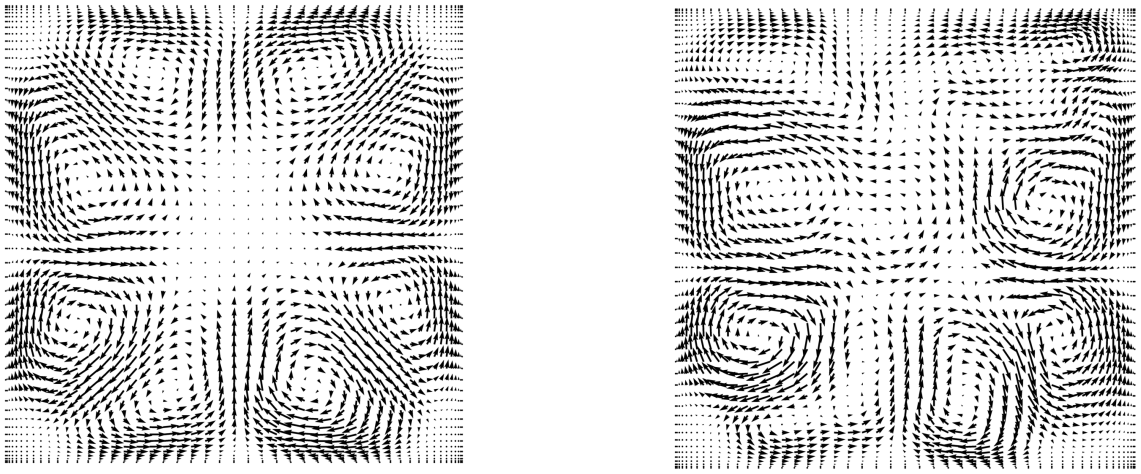

Figure 2.1: Cross stream velocity vector plot, turbulent puff $Re = 1500$, Time and streamwise averaged (left), instantaneous, streamwise averaged (right). The secondary motions are well visible and occupy a large part of the cross section, due to the low Reynolds number.

Figure 2.4 shows the vorticity field of a turbulent puff on the center plane. The fluid travels from

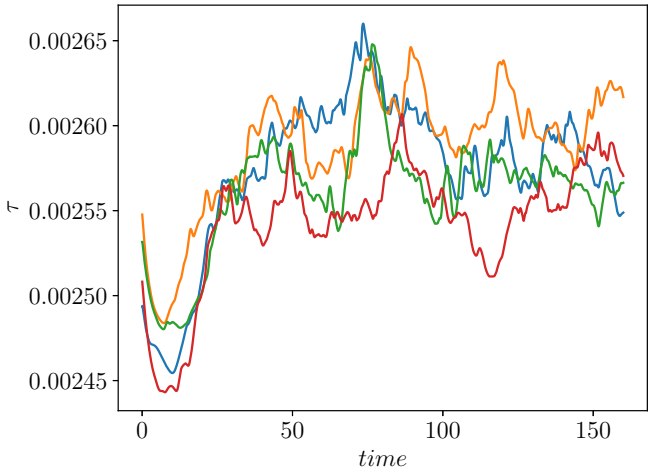

Figure 2.2: Time evolution of the surface averaged viscous stresses computed on the 4 walls, turbulent puff $Re = 1500$.

left to right, the generation of vortical structures is very sudden between $x = 30$ and 33. We observe a couple of roll ups at $x \sim 33.5$ and 34.5, these structures are very similar to Kelvin-Helmholtz vortices and are the equivalent of the roll ups observed by Bandyopadhyay (1986) and later studied by Shimizu and Kida (2009); Duguet et al. (2010b) in the circular pipe case. These roll ups are formed by the shear between the upcoming laminar flow and the low speed streaks near the wall formed in correspondence of the turbulent core of the puff. These are slower than the flow bulk velocity (U_b) and therefore move towards the upstream front of the puff. A proof of the presence of regions in which the flow is slower than the bulk velocity can be found in figure 2.5, in which we plot the probability density function (PDF) of the wall shear stress for a puff computed at $Re = 1500$. The strongly oscillating part of the plot is polluted by the laminar contribution, as shown in figure 2.6. In a laminar flow each point on the wall sees only one value of τ. The various points in the PDF are therefore not well explored and the PDF is not smoothed in time, since its regularity depends only on the spatial resolution. In contrast, in the case of an even slightly turbulent flow the velocity fluctuations rapidly smooth the PDF. The left and rightmost branches are solely given by the turbulent contributions, the negative values of τ on the left are a signature of the low speed streaks moving upstream with respect to the puff; these are a visible feature, although not occurring very often. The point on the upstream front in which the flow starts to become rotational coincides with a minimum of the positive flow area A^+, defined as the fraction of the cross section in which the streamwise velocity is larger than the bulk velocity.

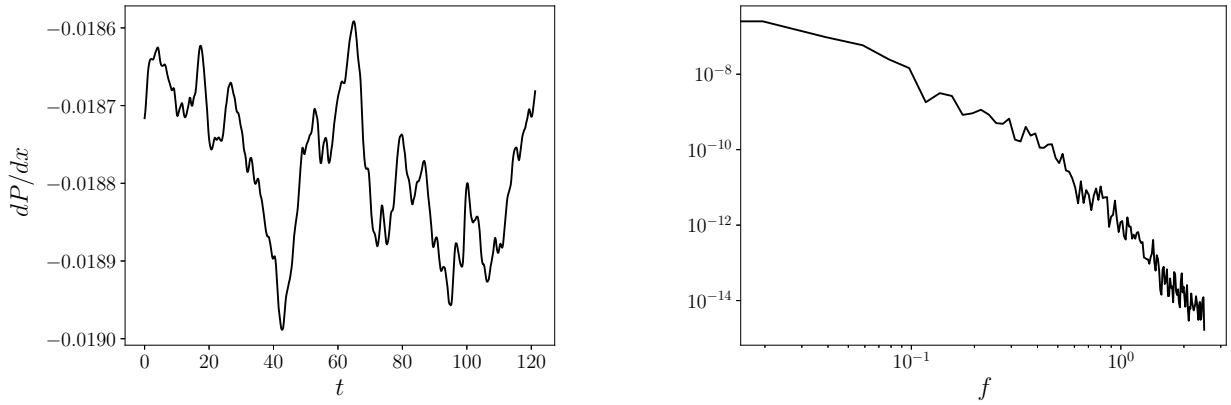

Figure 2.3: Time history (left) and PSD of the streamwise forcing, adapted to maintain a constant unitary non dimensional volume flow rate. The most prominent effect is given by the low frequency oscillations. Turbulent puff $Re = 1500$.

Figure 2.7 shows the variation of the instantaneous value of A^+ along x, for the same snapshot shown in figure 2.4. We see a clear minimum around $x = 45$, with an increasing attenuation of A^+ starting from $x \sim 40$, probably given by the influence of the low speed streak on the laminar flow, which is locally slowed down, but is not yet inflectional. The minimum is found at $x = 47$; after this point we observe a large roll up in figure 2.4 and a steep increase of A^+. As one would expect, the maximum lies around $x = 55$, in the most turbulent zone of the puff.

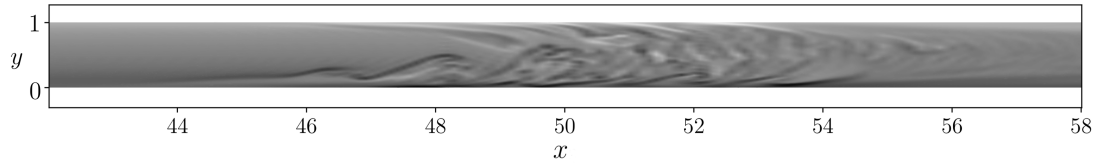

Figure 2.4: Vorticity contour (component perpendicular to the sheet) of a snapshot of a turbulent puff in a square duct at $Re = 1500$

Another way of looking at the localisation of turbulence consists in thinking in terms of Fourier modes. The intensity of the mode is not all that matters here; the phase plays a key role in the survival of the puff giving the spacial distribution required for the puff to self sustain. The upper half of figure 2.8 shows the cross surface averaged kinetic energy, plotted mode by mode. We clearly see a constructive interaction in correspondence with the upstream front in the lower half. The destructive interaction along the downstream front is globally there, but is less evident.

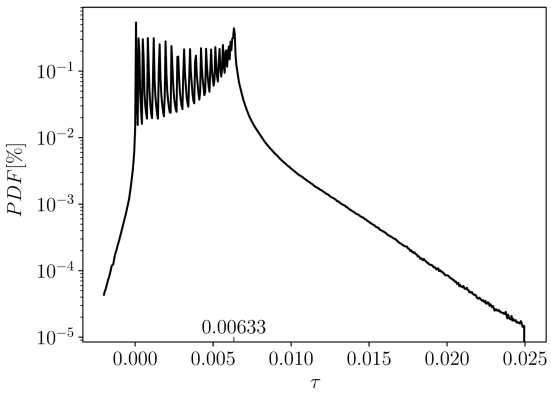

Figure 2.5: Viscous stress probability density function (PDF) of a turbulent puff in a square duct at $Re = 1500$, $N_y = 51$.

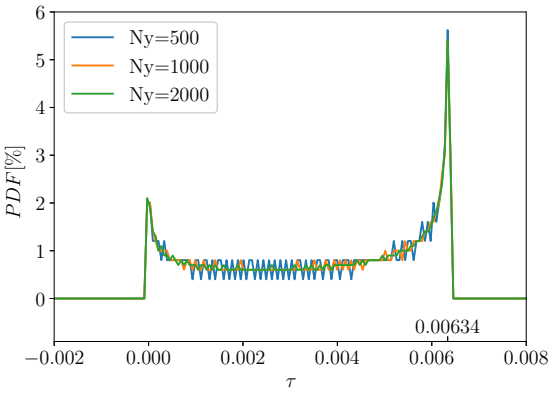

Figure 2.6: Viscous stress probability density function (PDF) and its convergence with varying number of grid points. Laminar flow in a square duct at $Re = 1500$

The inherent scales of puffs-particular features of puffs

The length of puffs

The puff length does not seem to be affected by the size of the computational domain, as seen in figure 2.9, in which we plot the y, z averaged kinetic energy for puffs computed at $Re = 1500$ and varying domain lengths. Depending on how the upstream and downstream front positions are defined we can retrieve slightly different puff lengths around $30h$. The lowest domain length ($L = 25h$) is close to the limit length for a puff to successfully self sustain. This limit is very close to the minimal length for circular ducts of 8π diameters found by Priymak and Miyazaki (2004) and later by Shimizu and Kida (2009). Figure 2.10 shows the spectra of the cross stream averaged energy plotted along the streamwise wavenumber $k_x = 2\pi n/L$ (with n the streamwise mode number). We notice two distinct behaviours, with an abrupt change at $k_x \sim 1$. For $k_x > 1$ the spectrum is typically turbulent, with an exponentially decreasing kinetic energy cascade. The exponent -0.17 is much lower than the -5/3 law (Kolmogorov, 1941) due to the low Reynolds number. At lower frequencies the tendency remains exponential, but the decrement is much stronger, with an exponent of -3.9. This behaviour is probably linked to the rapid energy transfer from the zero mode on which the forcing is applied to the turbulent scales. The $k_x = 1$ wavenumber corresponds to a wavelength of about $6h$, which is not one of the characteristic lengths of the puff. It is likely that this length is related to some turbulent structure

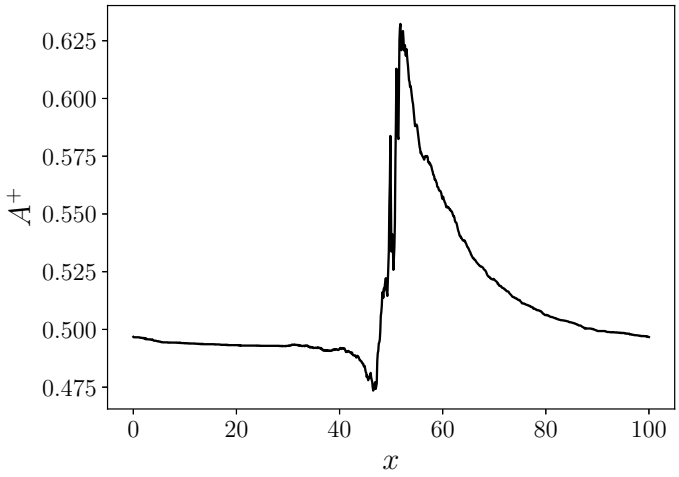

Figure 2.7: Instantaneous fraction of cross section with a positive streamwise velocity, computed on the same snapshot of figure 2.4.

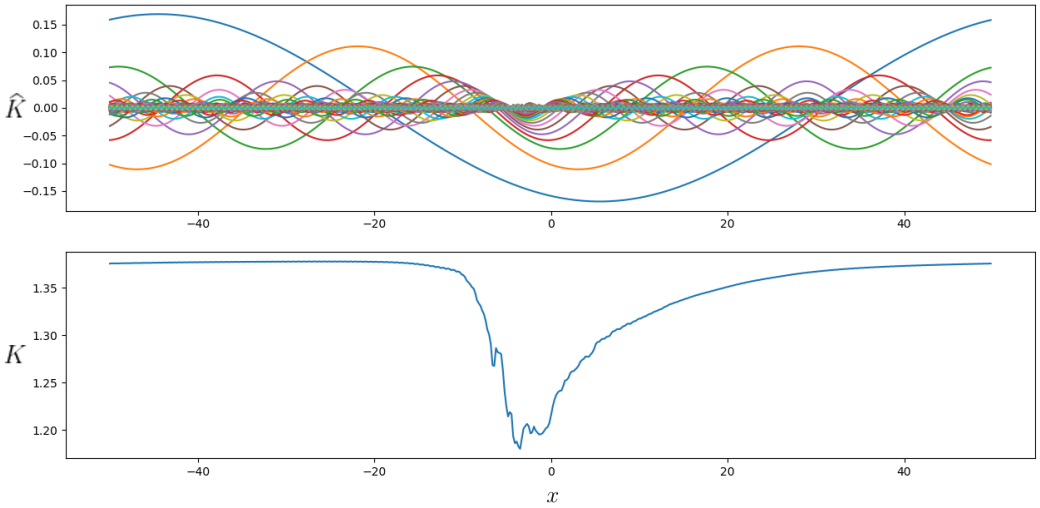

Figure 2.8: Section averaged kinetic energy of a turbulent puff, above the mode are plotted separately, below the modes are summed, giving the usual kinetic energy behaviour.

or feature of the puff, e.g. the upstream front, however this aspect remains unclear. For $L = 25h$ the energy levels are higher than those of observed for other lengths, due to the fact that the entire domain is occupied by turbulence, without much room for relaminarisation. If the domain is made even shorter the lack of a laminar inflow for the puff causes its disappearance and the flow settles on the laminar branch, compatibly with the observations and experiments by Hof et al. (2010); Kühnen

et al. (2018), who noticed that disturbances on the mean flow cause the relaminarisation of puffs.

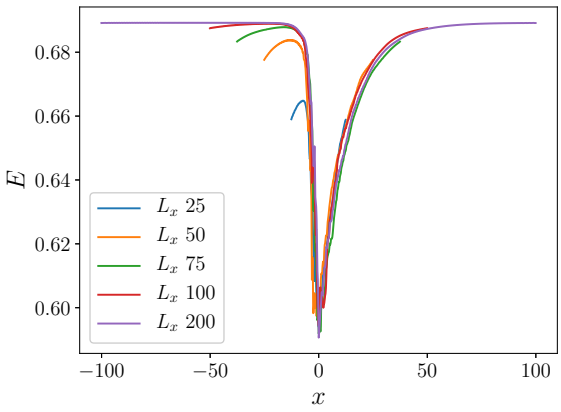

Figure 2.9: Instantaneous y, z averaged kinetic energy of turbulent puffs computed on domains of increasing lengths and $Re = 1500$.

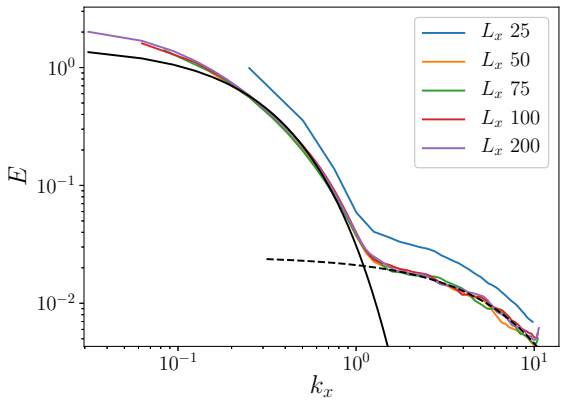

Figure 2.10: Time averaged spectra of the y, z averaged kinetic energy, computed on domains of increasing lengths and $Re = 1500$. The black dashed and continuous curves represent the functions $\exp(-0.17k_x)$ and $\exp(-3.9k_x)$, respectively

Large scale interaction: inter-puff distance

As we said above turbulent puffs need to be supplied with an upstream laminar flow. The velocity gradient has to be strong in a region where the velocity fluctuations can be sustained. If the flow is disturbed, artificially or by a preceding turbulent puff, the velocity profile is made more blunt, hence the mean velocity gradient is stronger close to the wall, where velocity fluctuations are less strong. The tail of puffs is therefore a refractory zone in which turbulence has a hard time surviving. Barkley (2016) proposed an analogy between puffs and neurons, that after the activation remain non-excitable during a certain time. If two puffs are close together, for instance right after a splitting event, the most downstream puff must survive on a limited amount of 'available production potential'. This results in a lower energy associated to the second puff. The downstream puff moves more downstream until it reaches a sufficient distance for its self sustaining process to function normally. In the case of circular pipes this distance is found to be around 100 diameters (Samanta et al., 2011; Barkley, 2016; Mukund and Hof, 2018). We performed a simulation in which two puffs were artificially put close together at a distance of $30h$ at $t = 0$, using a quite long domain ($L = 250h$) and $Re = 1500$. Figure 2.11 shows the evolution of the section averaged kinetic energy in x and time for the first 2400 time units.

The puffs are observed to move slower than the bulk velocity, thus shifting backwards in the frame of reference moving with U_b. The solution was repeatedly shifted to prevent the upstream puff from crossing the periodic boundary, which would have complicated the front tracking. Figure 2.12 shows the positions of the upstream fronts, with the shift removed in post-processing. The position of the front is not unambiguously defined in the literature. Shimizu and Kida (2009) proposed a criterion based on the very steep drop of the streamwise velocity at the front; we use here a criterion similar to the one proposed by Song et al. (2017), based on the kinetic energy of the fluctuations with respect to the laminar flow.

$$q(x) = \int_S (u - U_{lam})^2 + v^2 + w^2 dS \tag{2.21}$$

Figure 2.13 shows the value of q for a turbulent puff, with the threshold $q = 0.02$ indicated with a dot. The value of q remains zero outside of the puff, and has a rapid increase in correspondence to the upstream front. The threshold is placed in an interval of q that is not subject to strong variations. A higher value would end up in the more turbulent region of the puff resulting in fluctuations in position not due to the puff movement.

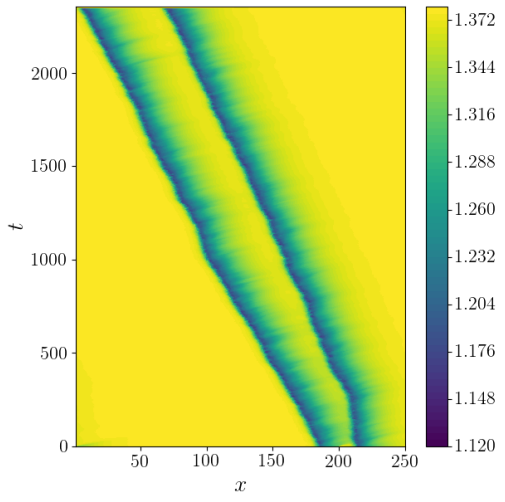

Figure 2.11: Section averaged kinetic energy evolution in x and time, up to $t \sim 2400$. Initial puff distance $30h$. The length of the computational domain is $L = 250h$.

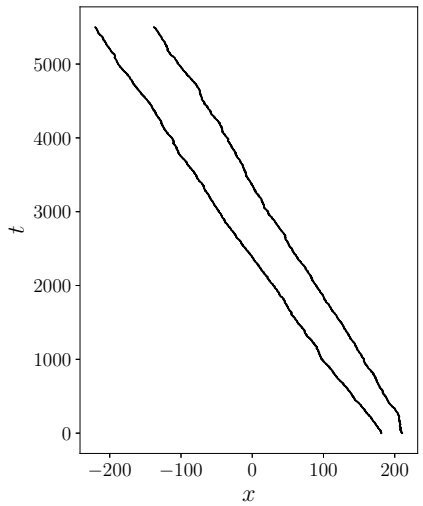

Figure 2.12: Evolution of the upstream fronts positions in time. Initial puff distance $30h$. The length of the computational domain is $L = 250h$.

We notice that the the second (downstream) puff is rapidly pushed downstream; then the separation is much slower but continues for a very long time at a constant rate, most probably until a steady state

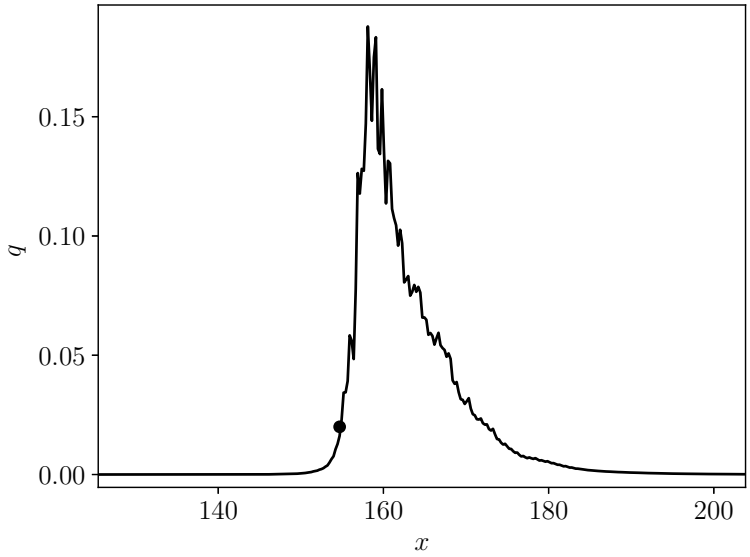

Figure 2.13: Value of q for a puff. The criterion $q = 0.02$ (solid circle) is used to determine the position of the upstream front.

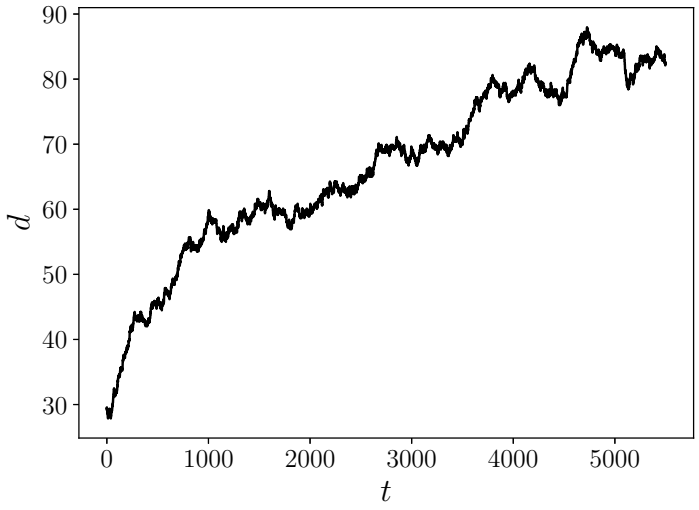

Figure 2.14: Evolution in time of the distance between two puffs, initially very close together. The average separation speed after the initial transient is about $5 \cdot 10^{-3} U_b$

is reached. This short range interaction is at the base of the direct percolation diagrams found by Avila et al. (2011) for puffs. This kind of scenario is found in very diverse problems, such as predator-prey models (Shih et al., 2016). The present simulation was not continued due to the very long time

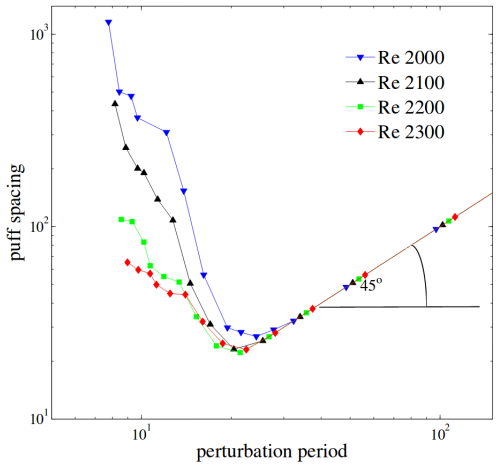

Figure 2.15: Dependency of puff spacing on injection period. Adapted from Samanta et al. (2011)

required. The separation would probably continue with the same rate, which does not change after the initial transient, see figure 2.14. The question now is to what steady state the system would converge, or in other words whether or not a long time equilibrium distance between puffs exists. Two cases can be hypothesised. It is possible that the distancing would continue until the disturbance given by the upstream puff is so small that it no longer affects the downstream puff, this would result in a distance given by a hydrodynamic phenomenon that would probably depend on Re. In the case of the present simulation it would result in the establishment of the minimal non-disturbance distance if the latter is less than half the duct length, or half the duct length itself if the domain is too short to host two sufficiently distanced puffs. This scenario would mean that a number of puffs in a very long duct at equilibrium can be separated by different distances, provided that these are sufficiently long. In other words a long range interaction between puffs does not exist. The second case is that an inherent equilibrium distance exists, and a number of puffs in a very long duct would increase the distance between them if this is shorter than the equilibrium distance, and decrease it otherwise. The investigation of this case would require at least 3 puffs and very long times. Samanta et al. (2011) performed an experiment in which turbulent puffs were injected with varying frequencies, measuring the distance between puffs at the end of the duct, 400 diameters after the injection. Figure 2.15 reports their results. For high frequencies the disturbances are too strong for all the puffs to survive, the distance increases with increasing frequency (or decreasing period). A minimum is found for a period of about 20 time units, meaning that starting from that point the distance covered by a puff in the interval between two injections is sufficient for the disturbance to be sufficiently small. After that

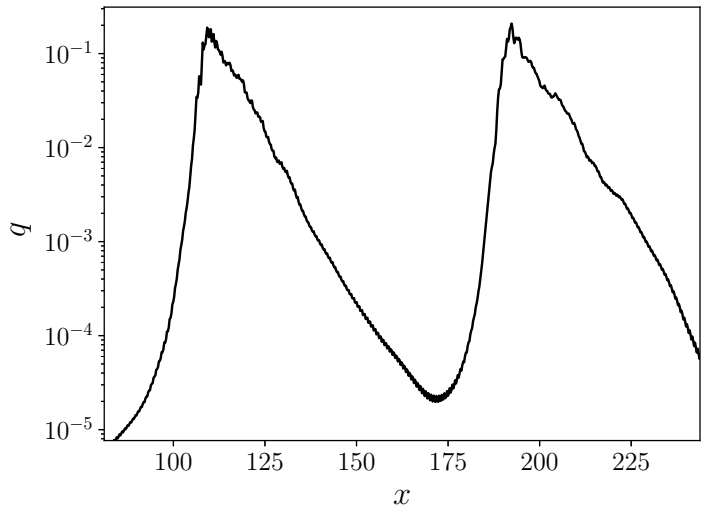

Figure 2.16: Section averaged turbulent fluctuations with respect to the laminar flow (q) for two puffs. The fluctuations vanish following a power law.

point a 45 degrees trend is found, meaning that no interaction is present. This observation suggests that while the short range interaction acts very quickly, determining the survival of puffs, the long range interaction, if at all present, can be observed only over very long times. This means that such a feature would be hard to observe, even experimentally, let alone with a DNS. The present calculation would therefore not be conclusive, even if it were run for very long times. Moreover, if such long range interaction is there, it may not be of hydrodynamic nature. Another possibility is that the interaction is acoustical. In this case the incompressible formulation used in the computation would not be able to capture the phenomenon. If the phenomenon existed, and were of acoustic nature, one may argue that the time required for a synchronisation between puffs based on an acoustic interaction would require long times. The 400 diameters used by Samanta et al. (2011) might not be sufficient. A method similar to the one used in Mukund and Hof (2018) in which the puffs are re-injected, simulating a periodic boundary, would probably be the most suitable, even if the times required would be very long. If a long range interaction were found it would mean that the direct percolation theory is not applicable to this case (Hinrichsen, 2000). Mukund and Hof (2018) investigated the long range interaction occurring via a number of short range interaction between several puffs, initially placed close to one another. The upstream puff pushes the downstream one and so on, in a wave like fashion. They observed puffs interact by clusters of around 5, but could not determine whether or not the hydrodynamic interaction

acts at further distances.

Another apparent aspect is that both puffs move consistently upstream throughout the whole simulation. The shifting speed is not very high (about $0.08U_b$) but produces a visible effect, the cause of which is not clear. Such phenomenon was not observed in the experiment by Mukund and Hof (2018), who used a velocity of the frame of reference equal to the speed of a single puff, exactly like in the present case. This, together with the continuous puff distancing phenomenon shows the high level of sensitivity of puffs with respect to perturbations. The hydrodynamic disturbance of the first puff on the second is very small, and decreases with increasing distance (see figure 2.16). This small perturbation is anyhow capable of producing visible effects on the puff large scale behaviour.

Sensitivity to structural perturbations

We can wonder how a turbulent puff would respond to a number of influences, such as a slight curvature of the pipe, an asymmetrical heating or duct vibration. In this context the structural perturbations are to be seen not as an external forcing, but rather as a slight change in the flow condition, showing as a change in the governing equations. The mathematical formulation expresses the nominal flow conditions, but the theoretical configuration is often not strictly reproduced in reality, even for very fine experimental campaigns. Let us consider an experiment involving turbulent puffs in a straight pipe, these experiments are currently performed using water and very long pipes (Avila et al., 2011; Mukund and Hof, 2018). The flow is incompressible and the pipe straight, and all efforts would be aimed at minimising any disturbances, for instance by choosing a very stiff pipe to limit vibrations, by placing a large number of supports to avoid excessive bending, and by using a small diameter pipe to limit the differences in temperature between the sides. We can wonder how sensitive a turbulent puff is to the these effects, and thus how critical these parameters are. A first objective of this work is to analyse the effect of curvature on turbulent puffs. To do this we develop a simplified model based on the concept by Dean and Hurst (1959) able to compute the laminar flow in a weakly curved duct. Then, by assuming a strict scale separation between the mean flow and the short, turbulent scales we use the model to predict the effects of curvature on the puff, finding a qualitative agreement with observations by Canton et al. (2016). Despite the typically low Mach number, the compressibility of the fluid might produce an effect, for instance in the inter-puff communication, potentially determining a long range equilibrium distance between puffs. In chapter 4 we investigate the acoustic field generated

by a turbulent puff looking for a low frequency selected wavelength that might be associated with a long range equilibrium distance. We anticipate here that no such wavelength is found, suggesting the non existence of this phenomenon, at least on acoustic grounds. This analysis however allows us to characterise the aeroacoustic field generated by a puff, both in a (hypothetical) unbounded domain in which the walls are permeable to acoustic waves, and in the real case in which the noise radiation is strongly affected by the presence of the duct. The puff proves to be a valuable case for a yet unsettled debate in aeroacoustics, namely the importance of the noise generated by the viscous stresses on the total noise generation. The only possibility for this contribution to be relevant is at low Mach and low Reynolds numbers. This problem had been tackled in the past in fully turbulent flows (Hu et al., 2003), or in the case of boundary layer transition (Wang et al., 1996a). Turbulent puffs represent the lowest limit of Re in which turbulence is able to self-sustain, in a realistic application this translates also to low Ma.

Chapter 3

The flow in a curved square duct

Table of contents of this chapter

The laminar solution of the flow in a straight duct is the Hagen-Poiseuille flow. This solution is known to be linearly stable for any Reynolds number, it is therefore unconditionally stable or in other words the critical Reynolds number goes to infinity (Tatsumi and Yoshimura, 1990), as in the round pipe case (Drazin and Reid, 1981). The scenario changes if the duct is bent along the streamwise direction, as in figure 3.1. Even for very small curvatures (very large R) the laminar solution is no longer the Hagen-Poiseuille flow, since the centrifugal force drives the flow towards the concave, outer wall, giving rise to two counter-rotating vortices that are known as the Dean vortices.

The appearance of symmetric counter rotating secondary vortices in pipe and duct flows was first observed experimentally by Eustice and Larmor (1910). A more quantitative understanding of the

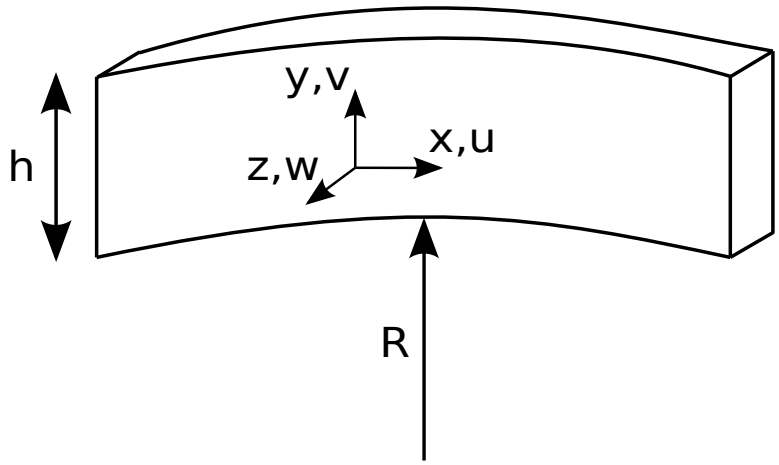

Figure 3.1: Sketch of the curved square duct, x, u are the streamwise dimension and velocity component, y, v and z, w are the wall normal directions and velocity components. The curvature radius R is aligned with y.

problem was provided by the works of W.R. Dean; his seminal study (Dean, 1927, 1928) laid the foundation for the analytical solution of the problem based on a perturbation method. This technique was used in the case of a steady laminar flow in a circular pipe with relatively weak curvature. Dean showed that the only control parameter was $Re\sqrt{h/R}$ (which he used squared), nowadays known as the Dean number, and that a cross-flow velocity field consists of two counter-rotating vortex cells where the flow in the center plane was directed toward the outer wall. These counter rotating vortices are nowadays called Dean cells or Dean vortices. In his first article, Dean (1927) used a first order expansion in the parameter k, that was later named the Dean number De and will be introduced later in this chapter. The first order however was not enough to evaluate the influence of curvature on the pressure drop. In his second paper (Dean, 1928) the expansion was brought to higher order showing a decreasing flow rate with increasing curvature. In a further study Dean and Chapman (1928) also considered the curved two-dimensional channel, i.e. unbounded in one span-wise direction. In this case the cross-flow vortices resulted from instability of the plane Poiseuille flow, associated to a critical Dean number. This represents a different scenario than the one observed for the pipe, where the cells' amplitude is proportional to the Dean number; the flow with its counter rotating vortices is to be seen as the new laminar solution rather than an instability. Dean and Hurst (1959) replaced the actual secondary motion by a uniform wall-normal stream in order to simplify the non linear terms and thus the analytical solution. Moreover with that simplification, results have a more general scope

and apply to any form of pipe, circular or square among others. More importantly for the present purpose, the equations were simplified, based on the narrow gap approximation that allows replacing the curvilinear coordinates with a Cartesian system.

Dean's series expansion method for the circular duct problem was later performed at higher order by Van Dyke (1978) thanks to the use of numerical tools, while McConalogue and Srivastava (1968) used an iterative method to solve the early Dean model (Dean, 1927, 1928). In a recent analytical effort Norouzi and Biglari (2013) calculated the solution for the flow in a curved duct of rectangular cross section using a perturbation method. Apart from the aforementioned studies, most of the following works relied on the rapidly developing computational resources to solve the full Navier-Stokes equations, very often using the lateral symmetry hypothesis. Some authors concentrated on the rectangular duct geometry (see for instance Cheng and Akiyama (1970); Joseph et al. (1975); Cheng et al. (1976)), others studied the circular duct (Dennis and NG, 1982; Yanase et al., 1989), finding qualitatively similar results. These studies showed the presence of an additional pair of counter-rotating vortices produced by the Görtler instability on the concave wall, placed at the outer part of the duct. This instability appears for high enough curvature and flow velocity through a subcritical bifurcation (Shanthini and Nandakumar, 1986). The subcriticality is strongly linked to the arbitrarily imposed lateral symmetry, as later shown by Winters (1987). In particular Cheng et al. (1976) performed a parametric study for different Dean numbers showing that for increasing De the flow evolved from 2 to 4 circulation cells, returning to a 2-cell structure and subsequently back to 4 cells, hence bearing a non trivial dependence on De. The 2-cell solution is in truth only observed for low De. Daskopoulos and Lenhoff (1989) noticed that the 2-cell solution presents instead 4 cells for De close to the critical one, even though the additional cells are rather weak. We will henceforth refer to the two solutions as the weak and strong 4-vortex solution. For a more extensive review on the early numerical and experimental works on the subject, see Ito (1969); Berger et al. (1983).

Winters (1987) largely contributed to the understanding of the Dean problem, specifically referring to the square duct case, clarifying some important aspects. He provided an early detailed study of the first bifurcations undertaken by the flow, also determining the linear stability of the branches. The only stable symmetric solutions were found to be the 2-vortex solutions (which we call the weak 4-vortex solution) below the first bifurcation and above the second. The (strong) 4-vortex solutions were instead revealed stable to symmetric perturbations, but unstable to asymmetric perturbations.

This result was confirmed by Yanase et al. (1988) in the curved pipe case. Winters (1987) gave a quantitative criterion for the distinction between low and high curvature, showing that for $h/R > 0.05$ the bifurcation scenario is governed by two independent parameters, the Reynolds number Re and the geometry h/R, whereas for $h/R < 0.05$ the curvature can be considered as weak and the dynamic is governed by a single control parameter, the Dean number De ($De = Re\sqrt{h/R}$). In addition his work shed light on the effect of the symmetry hypothesis, which was found to artificially stabilise the 4-vortex solution, thus altering the 2 to 4-cell bifurcation, which was earlier deemed subcritical (Shanthini and Nandakumar, 1986) but is in fact a supercritical bifurcation. Wang and Yang (2004) later confirmed these results and expanded the analysis to higher Dean numbers finding periodic oscillations after the symmetry breaking bifurcation and a chaotic behaviour for high De, as also seen in Mondal et al. (2007). In particular the work by Wang and Yang (2004) considers a forced convection problem, however no buoyancy effects are included in the momentum equations, making the results consistent with the present and other studies. Soh (1988) confirmed the existence in 3D of the dual solutions found in 2D, while the periodic oscillation was found by Sankar et al. (1988), who numerically studied the flow development problem, i.e. the evolution of a straight laminar flow entering in a curved section. The solution was obtained using the stationary cylindrical 3D Navier-Stokes equations neglecting the streamwise diffusion. For subcritical De the flow evolves towards the stationary 2D solution, in the supercritical regime the flow oscillates periodically along the streamwise direction between the two attractors. Bara et al. (1992) investigated experimentally the flow development problem comparing the results with those computed using the same code used by Sankar et al. (1988). They showed that the emergence of the streamwise periodic oscillations could be promoted by asymmetrically perturbing the flow, consistently with the 2D stability theory (see for instance Winters (1987)).

The presence of curvature is crucial not only for laminar flows, but has a substantial impact on turbulence. White (1929); G. I. Taylor (1929) experimentally demonstrated that it has a stabilising effect, increasing the critical Reynolds number with respect to the straight case. Sreenivasan and Strykowski (1983) showed that a turbulent flow entering in a coiled section becomes laminar and becomes again turbulent in the subsequent straight section. Recently the laminar to turbulent bifurcation was shown to change from subcritical, in the straight case, to supercritical for large enough curvatures, with a smooth transition to turbulence (Rinaldi et al., 2019; Canton et al., 2016; Kühnen et al., 2014, 2015; Barkley, 2019). For a complete review on the effects of curvature on turbulence the reader is referred

to the recent review by Kalpakli Vester et al. (2016).

Governing equations

The incompressible Navier Stokes equations, written in polar coordinates read

$$\frac{1}{r^*}\frac{\partial u^*}{\partial \theta} + \frac{1}{r}\frac{\partial (rv^*)}{\partial r^*} + \frac{\partial w^*}{\partial z^*} = 0 \tag{3.1a}$$

$$\frac{\partial u^*}{\partial t^*} + \frac{u^*}{r^*}\frac{\partial u^*}{\partial \theta^*} + v^*\frac{\partial u^*}{\partial r^*} + w^*\frac{\partial u^*}{\partial z^*} + \frac{u^* v^*}{r^*} = - \frac{1}{r^*}\frac{\partial p^*}{\partial \theta^*} + \nu\left(\frac{1}{r^{*2}}\frac{\partial^2 u^*}{\partial \theta^{*2}} - \frac{u^*}{r^{*2}} + \frac{1}{r^*}\frac{\partial}{\partial r^*}\left(\frac{\partial u^*}{\partial r^*}\right) - \frac{2}{r^{*2}}\frac{\partial v^*}{\partial \theta^*} + \frac{\partial^2 u^*}{\partial z^{*2}}\right) \tag{3.1b}$$

$$\frac{\partial v^*}{\partial t^*} + \frac{u^*}{r^*}\frac{\partial v^*}{\partial \theta^*} + v^*\frac{\partial v^*}{\partial r^*} + w^*\frac{\partial v^*}{\partial z^*} - \frac{u^{*2}}{r^*} = - \frac{\partial p^*}{\partial r^*} + \nu\left(\frac{1}{r^{*2}}\frac{\partial^2 v^*}{\partial \theta^{*2}} - \frac{v^*}{r^{*2}} + \frac{1}{r^*}\frac{\partial}{\partial r^*}\left(\frac{\partial v^*}{\partial r^*}\right) + \frac{2}{r^{*2}}\frac{\partial u^*}{\partial \theta^*} + \frac{\partial^2 v^*}{\partial z^{*2}}\right) \tag{3.1c}$$

$$\frac{\partial w^*}{\partial t^*} + \frac{u^*}{r^*}\frac{\partial w^*}{\partial \theta^*} + v^*\frac{\partial w^*}{\partial r^*} + w^*\frac{\partial w^*}{\partial z} = - \frac{\partial p^*}{\partial z} + \nu\left(\frac{1}{r^{*2}}\frac{\partial^2 w^*}{\partial \theta^2} + \frac{1}{r^*}\frac{\partial}{\partial r^*}\left(\frac{\partial w^*}{\partial r^*}\right) + \frac{\partial^2 w^*}{\partial z^{*2}}\right) \tag{3.1d}$$

u, v, w are the velocity components in the θ (tangential), r, z (radial and axial) directions. These coordinates will be transformed in the cartesian x (stream-wise) and y, z (span-wise) directions. The * symbol denotes the dimensional quantities. If the curvature radius R is large with respect to the channel width h we have:

$$\begin{aligned} y^* &= r^* + R \approx R \\ dy^* &= dr^* \\ x^* &= (r^* + R)\sin(\theta^*) \approx R\theta^* \end{aligned} \tag{3.2}$$

Equations 3.1 become, after some mathematical manipulations

$$\frac{\partial u^*}{\partial x^*} + \frac{\partial v^*}{\partial y^*} + \frac{v^*}{R} + \frac{\partial w^*}{\partial z^*} = 0 \tag{3.3a}$$

$$\frac{\partial u^*}{\partial t^*} + u^*\frac{\partial u^*}{\partial x^*} + v^*\frac{\partial u^*}{\partial y^*} + w^*\frac{\partial u^*}{\partial z} + \frac{u^* v^*}{R} = - \frac{\partial p^*}{\partial x^*} + \nu\left(\frac{\partial^2 u^*}{\partial x^{*2}} + \frac{2}{R}\frac{\partial u^*}{\partial x^*} - \frac{u^*}{R^2} + \frac{1}{R}\frac{\partial u^*}{\partial y^*} + \frac{\partial^2 u^*}{\partial y^{*2}} + \frac{\partial^2 u^*}{\partial z^{*2}}\right) \tag{3.3b}$$

$$\frac{\partial v^*}{\partial t^*} + u^*\frac{\partial v^*}{\partial x^*} + v^*\frac{\partial v^*}{\partial y^*} + w^*\frac{\partial v^*}{\partial z^*} - \frac{u^{*2}}{R} = - \frac{1}{\rho}\frac{\partial p^*}{\partial y*} + \nu\left(\frac{\partial^2 v^*}{\partial x^{*2}} - \frac{2}{R}\frac{\partial v^*}{\partial x^*} - \frac{v^*}{R^2} + \frac{1}{R}\frac{\partial v^*}{\partial y^*} + \frac{\partial^2 v^*}{\partial y^{*2}} + \frac{\partial^2 v^*}{\partial z^{*2}}\right) \tag{3.3c}$$

$$\frac{\partial w^*}{\partial t^*} + u^*\frac{\partial w^*}{\partial x^*} + v^*\frac{\partial w^*}{\partial y^*} + w^*\frac{\partial w^*}{\partial z^*} = - \frac{1}{\rho}\frac{\partial p^*}{\partial z^*} + \nu\left(\frac{\partial^2 w^*}{\partial x^{*2}} + \frac{1}{R}\frac{\partial w^*}{\partial y^*} + \frac{\partial^2 w^*}{\partial y^{*2}} + \frac{\partial^2 w^*}{\partial z^{*2}}\right) \tag{3.3d}$$

The non dimensionalization is performed using two reference velocities U_b, V_0 and two reference lengths L, h for stream-wise and span-wise velocities and lengths (U_b and h being the streamwise bulk velocity and the channel height). The main effect of curvature in a completely confined flow is the generation of vortices, therefore we can assume that the order of magnitude of the centrifugal term u^{*2}/R in 3.1c is the same as that of the non linear terms. We have

$$\frac{V_0^2}{h} \sim \frac{U_b^2}{R} \qquad \frac{U_b V_0}{L} \sim \frac{U_b^2}{R}$$

which leads to the scaling laws

$$\frac{V_0}{U_b} = \sqrt{\frac{h}{R}} := \varepsilon \qquad \frac{V_0}{U_b} = \frac{L}{R} = \varepsilon \tag{3.4}$$

We now assume that the curvature is low, i.e. $\varepsilon \ll 1$ and we neglect the terms of $\mathcal{O}\left(\varepsilon^2\right)$ or higher.

We obtain a minimal model for the flow in a weakly bent duct.

$$\frac{\partial u}{\partial x}+\frac{\partial v}{\partial y}+\frac{\partial w}{\partial z}=0 \tag{3.5a}$$

$$\frac{\partial u}{\partial t}+De\left(u\frac{\partial u}{\partial x}+v\frac{\partial u}{\partial y}+w\frac{\partial u}{\partial z}\right) \quad =-\frac{\partial P}{\partial x}+\frac{\partial^2 u}{\partial y^2}+\frac{\partial^2 u}{\partial z^2} \tag{3.5b}$$

$$\frac{\partial v}{\partial t}+De\left(u\frac{\partial v}{\partial x}+v\frac{\partial v}{\partial y}+w\frac{\partial v}{\partial z}-u^2\right)=-\frac{\partial p}{\partial y}+\frac{\partial^2 v}{\partial y^2}+\frac{\partial^2 v}{\partial z^2} \tag{3.5c}$$

$$\frac{\partial w}{\partial t}+De\left(u\frac{\partial w}{\partial x}+v\frac{\partial w}{\partial y}+w\frac{\partial w}{\partial z}\right) \quad =-\frac{\partial p}{\partial z}+\frac{\partial^2 w}{\partial y^2}+\frac{\partial^2 w}{\partial z^2} \tag{3.5d}$$

Where

$$De=Re\sqrt{\frac{h}{R}}, \qquad Re=\frac{U_b h}{\nu} \tag{3.6}$$

are the Dean and the Reynolds numbers and

$$\begin{array}{lll} u=\dfrac{u^*}{U_b} & v,w=\dfrac{v^*,w^*}{V_0} & p=\dfrac{p^* h}{\mu V_0} \\ t=\dfrac{t^* U_b^2}{\nu} & y,z=\dfrac{y^*,z^*}{h} & x=\dfrac{x^*}{L} \end{array} \tag{3.7}$$

are the non-dimensional variables.

Discussion on the equations

These equations are similar to those proposed by Dean and Hurst (1959) in the 2-dimensional limit. It is worth noticing however that in those works, the fact of neglecting some of the curvature terms in the equations is justified with heuristic arguments, without a proper dimensional study. Indeed the term uv/R of equation (3.1b) and most importantly the curvature term of the continuity equation (3.3a) are of the same order as the term u^2/R in (3.1c), when non dimensionalising using only one reference velocity and length. In this formulation we introduce two reference velocities and lengths. This allows us to neglect the curvature term in the continuity equation (hence permitting the use of a Cartesian solver) without being forced to neglect all the curvature terms in the momentum equations. We obtain a one parameter formulation, similar to the one by Dean, but overcoming the 2D limit (the Dean equations are 2D). Dean's inconsistency may be the reason why the works that followed (see the first part of the present chapter) used a higher order approximation, which had the advantage of

formally allowing some curvature terms, at the cost of a more complex numerical solution requiring an ad-hoc solver. The equations depended on two control parameters: a curvature parameter and a streamwise velocity related term which is often a pressure gradient. This work demonstrates that the same results can be achieved using Dean's model, and therefore that the additional numerical burden is not justified by better results, at least in the low curvature limit.

The equations that we obtain are parabolic in the streamwise direction and therefore can be solved using a parabolic solver without introducing further approximations. This approach has been adopted by Sankar et al. (1988), who used a parabolic approximation of the Navier-Stokes equations, showing a posteriori that the results were in good agreement with the experimental measurements. The present analysis provides a mathematical justification to the parabolic hypothesis.

The low curvature hypothesis

Winters (1987) gave a quantitative evaluation of the dependence of some observables on the curvature ε. The Dean numbers at which bifurcations occur are little affected for $\varepsilon > 0.05$, and the bifurcations tend to occur at higher De when the curvature is tighter. This implies that an analysis performed with a single control parameter is reliable only for small curvatures, for curvatures higher than the threshold a two control parameter model is required. Ito (1959) experimentally retrieved a dependency law of the friction factor on De, showing that the curves collapsed on top of each other for low curvatures. Cieślicki and Piechna (2012) performed various numerical simulations and experiments on circular ducts with different curvatures and torsions, noticing that the pressure losses collapsed to the same values for the same Dean number, when curvature was low enough. They also reported a dependency of the maximum curvature on De with a larger 'low curvature thresholds' for low De. They also retrieve a dependency law of the friction factor on De very close to the one by Ito (1959). Canton et al. (2017) claimed that a single control parameter is never sufficient to represent the flow in a bent pipe. To prove this they compared the value of the friction factor computed for a given De and curvatures ranging from 0 to 1. The friction factors do not collapse on a single curve (see figure 5 of Canton et al. (2017)), in contrast to what was shown in the previous literature (Cieślicki and Piechna, 2012; Ito, 1959), but lie instead on a rather large band. This analysis however is not conclusive. The comparison can only be relevant in the low curvature limit, since this is the hypothesis on which the single parameter case is based. The lowest curvature investigated is actually not 0, but $h/R = 0.1$,

which is double the threshold curvature proposed by Winters (1987) for the square duct case (Canton et al. (2017) define the curvature using the radius of the pipe, we convert the curvature of 0.05 used in the reference to be consistent with the present definition). With such a high threshold for the low curvature the argument by Canton et al. (2017) cannot be considered in the discussion.

Two dimensional flow

In this section we solve equations 3.5 in 2D, i.e. assuming that the flow is invariant in x. This analysis allows us to validate the model by comparing the present results with those reported in the literature. Moreover, to the best of our knowledge, a numerical solution of the Dean equation has never been shown in the literature. We demonstrate that not only can this model reproduce very closely the 2D results of the literature in terms of bifurcations and dynamics, but can also be regarded as a simple yet remarkably rich dynamical system.

Numerical method

The 2D solutions presented in this chapter are obtained by solving equations (3.5) using a program directly linked to the incompressible pseudo-spectral solver presented in chapter 2. The differences consist in assuming that the solution is invariant in x, hence $k = 0$, in adding a forcing term u^2 and multiplying the nonlinear terms by De. The grid is composed of 31×31 Chebyshev points, a finer grid of 101×101 points with a lower time step was used for validation and no significant differences were observed, as shown in table 3.1. A suitable time step is found to be $\Delta t = 1.2 \cdot 10^{-5}$ for all the cases presented. The full Python code, together with some additional details on the numerics is reported in appendix A.

Generalities about the flow at low De

Two counter rotating (Dean) vortices are observed for any non zero Dean number. For very low De the flow is stationary, as shown in the contour plots in figure 3.2. The vortices are elongated and the maximum of the streamwise centerline velocity is shifted towards the outer wall when De increases (Cheng and Akiyama, 1970).

Around $De = 128$ the flow ceases to be stationary. Periodic oscillations are observed between a

Table 3.1: Comparison between two calculations at $De = 150$ in $2D$, the quantities reported are averaged over one time period. The coarser space (N, number of grid points) and time discretisations (second line of the table) are those used in the rest of the paper, the finer simulation is used as a benchmark. Very little differences are observed in the results: the period T varies of a quantity compatible with the dt itself, the average pressure gradient dP/dx and the streamwise and spanwise dissipations ε_u,ε_{vw} exhibit very limited differences. The differences between the streamwise pressure gradient (equal to the energy injection if $U_b = 1$) and the streamwise dissipation indicate the level of convergence of the respective calculations.

$N_y \times N_z$	Δt	T	dP/dx	ε_u	ε_{vw}
101×101	$1 \cdot 10^{-6}$	0.20132	-44.5091	44.5066	11.43055
31×31	$1.2 \cdot 10^{-5}$	0.2013	-44.513	44.5130	11.43557

solution simiar to that at $De = 100$ and one showing two additional, smaller, high intensity, counter rotating vortices located close to the upper wall, as shown in figure 3.3. In truth a change in behaviour occurs before the loss of stationarity, at $De = 124$ we observe a second pair of vortices, very mild in intensity. These vortices have been often overlooked, even though they were observed early on by Daskopoulos and Lenhoff (1989) who named this solution the weak 4-vortex solution, as opposed to the strong 4-vortex solution that brings about the non stationarity. We will adopt the same naming convention in the following. The weak 4-vortex solution can be observed in figure 3.4. The vortices are barely visible in the streamplot on the right, whereas they are not visible in the contour plot due to the very low intensity. Wang and Yang (2004) observed a change in branch corresponding to the bifurcation between the 2 and the weak 4-vortex solution, but since both are stationary, they did not look at the differences between them. The fact of reproducing such a particular feature of the flow provides some degree of confidence towards the reliability of the simplified model at non trivial Dean numbers, a thorough validation will be nonetheless carried out in the following.

Bifurcation diagram

The solutions can be distinguished according to their symmetry in the wall normal direction (z):

- symmetric solutions

$$u(0.5 + z) = u(0.5 - z)$$
$$v(0.5 + z) = v(0.5 - z)$$
$$w(0.5 + z) = -w(0.5 - z)$$

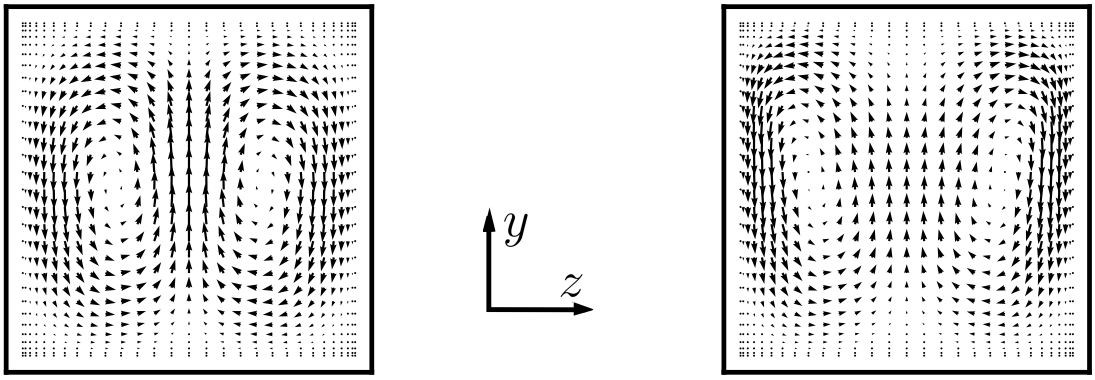

Figure 3.2: Contour plots of the 2D flow field at $De = 10$ (left) and $De = 100$ (right)

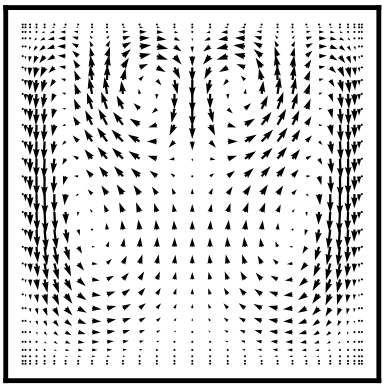

Figure 3.3: Contour plot of a snapshot of the 2D flow field at $De = 130$

- antisymmetric solutions

$$u(0.5 + z) = -u(0.5 - z)$$
$$v(0.5 + z) = -v(0.5 - z)$$
$$w(0.5 + z) = w(0.5 - z)$$

In order to determine whether the system is stationary, periodic, aperiodic or chaotic we use a Poincaré like section based on the three following criteria:

- $v = 0$
- $\frac{\partial v}{\partial t} < 0$
- $w < 0$

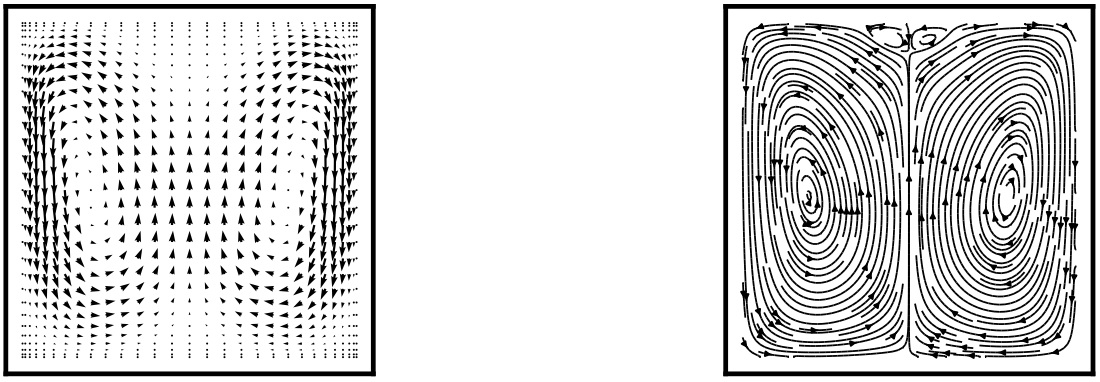

Figure 3.4: Contour plot (left) and stream-plot (right) of the 2D flow field at $De = 127$ (stationary, weak 4-vortex solution). The Görtler vortices are visible in the stream-plot at the top of the figure.

measured in a specific point located at the centerline close to the outer wall, specifically at $y = 0.9045, z = 0.5$. These conditions are met only once per period, thus if the oscillation is periodic the system will cross the section every T time units, and the numerical values will be the same.

The open circles in figure 3.5 indicate the values of the squared velocity 2-norm in the stationary regime. The first bifurcation from a steady regime to an unsteady, periodic regime occurs at $De = 128.32$. This specific Dean number will be henceforth be referred to as the critical Dean number De_c. In the same figure, the black dots represent the values of the squared 2-norm of the velocity vector at each crossing of the Poincaré-like section, for each De the simulation was run for at least 10 periods. Hence the periodic behaviour is represented by at least 10 superposed points, as can be seen for instance at $De = 130$.

In the following we will compare the bifurcation diagram with the one reported by Wang and Yang (2004). It is important to clarify that these authors use both the Dean number De, defined as in the present paper, and the pseudo Dean number D_k, defined differently. The comparisons are reported here only in terms of De, the same authors provide a conversion table between D_k and De (see table 3 of the reference).

The system holds its periodicity until $De \approx 193$, where it becomes aperiodic. Wang and Yang (2004, 2005) also observed a change in behaviour in that Dean number range, a slight increase and then a decrease in the period, but they did not mention to observe aperiodicity. The aperiodic regime is only observed over a narrow range of De, already at $De = 195$ the system is complex enough to

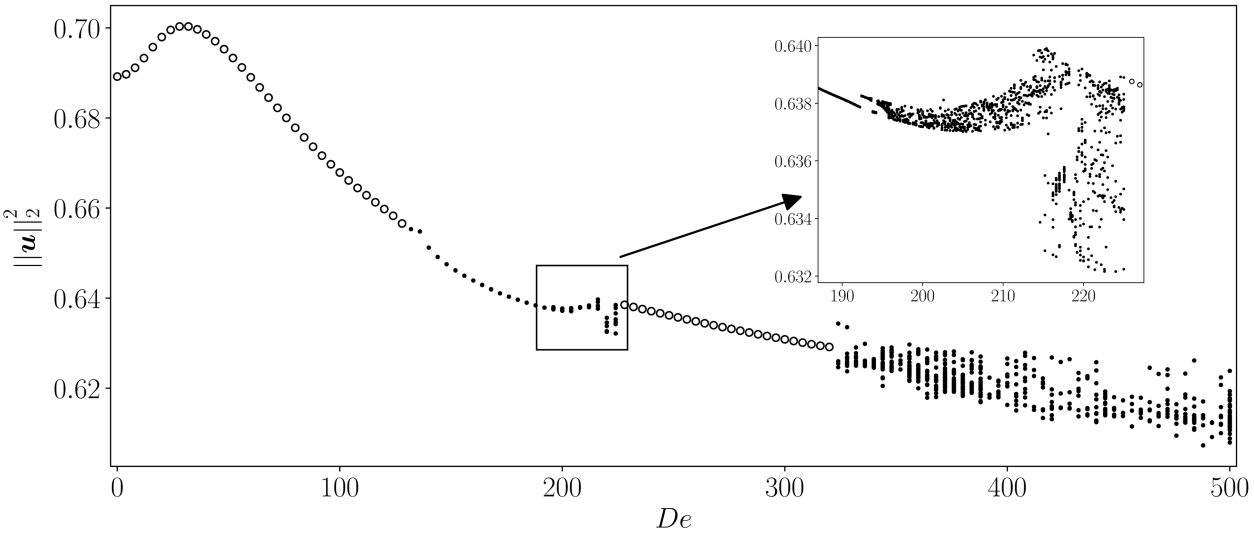

Figure 3.5: Filled circles: values of the squared 2-norm of the velocity vector at the instants when the Poincaré section is crossed. Open circles: values of the square of the 2-norm of the velocity vector in the stationary cases. The first bifurcation from a steady regime to an unsteady, periodic regime occurs at $De = 128.32$. Starting from $De \approx 193$ we observe two periods which are incommensurable, characteristic of the aperiodic regime. Then the system quickly evolves into chaos from $De \approx 195$. For $De \in [227, 318]$ the system is again stationary. After a narrow periodicity interval the system becomes again chaotic at $De = 324$. A magnification of the bifurcation diagram for $De \in [190, 230]$ is shown in the inset

be considered as chaotic. Analysing the magnified part in figure 3.5, we notice the presence of a new solution branch to which the system abruptly jumps back and forth. The increase in complexity is then very rapid. Between $De = 125$ and 214 the system is chaotic with values of the velocity norm that remain enclosed in the envelope of the two former branches. Between $De = 214$ and 227 the values no longer lie within the same envelope, probably due to the presence of a third branch (which was indeed observed by Wang and Yang (2004)). For $De > 227$ the system very quickly returns to a stationary regime, which lasts until $De = 318$, where very mild, periodic oscillations are observed up to $De = 323$. For higher Dean numbers the system rapidly becomes again chaotic. No stationary or periodic regimes were observed for higher Dean numbers.

The changes in regime observed for the present model are in very good agreement with the literature. In particular the critical Dean number given by the model, $De_c = 128.32$, is in excellent accordance with the $De_c = 128.22$ by Wang and Yang (2004), which is one of the most accurate studies available, or $De_c = 129.71$ by Winters (1987). Both these results were obtained by solving the

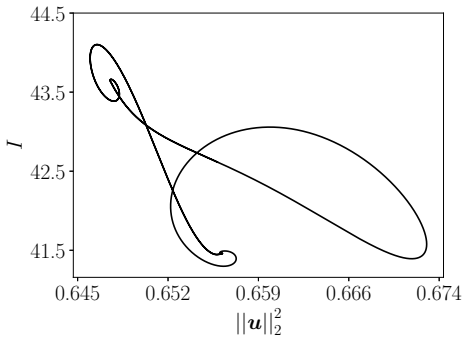

(a) $De = 130$

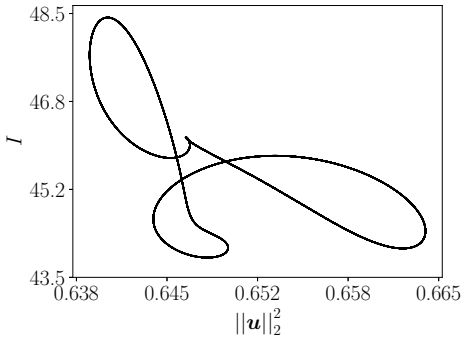

(b) $De = 160$

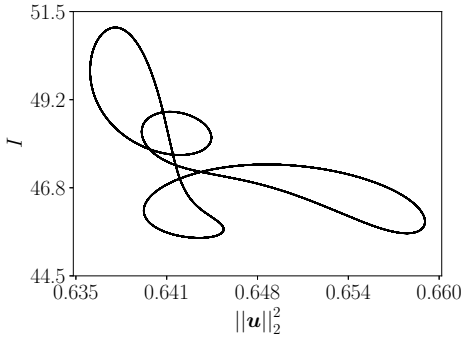

(c) $De = 180$

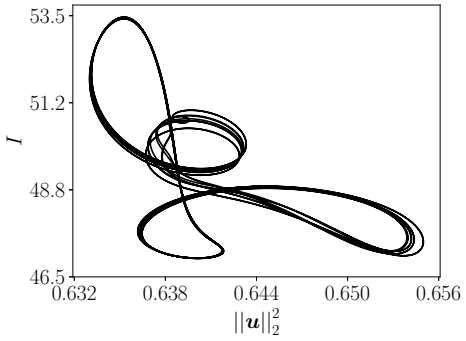

(d) $De = 200$

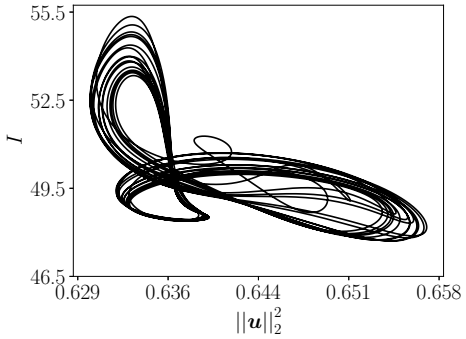

(e) $De = 220$

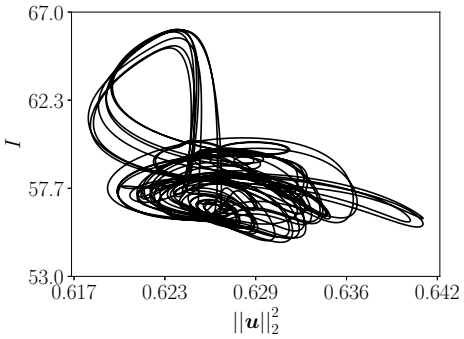

(f) $De = 350$

Figure 3.6: Energy injection-velocity phase portraits for increasing Dean numbers. For $De = 130$ the system is periodic and oscillates between 3 attractors, at $De = 160$ a new attractor starts to emerge, becoming more evident for $De = 180$, where the oscillation remains periodic. The flow is already mildly chaotic at $De = 200$, the complexity increases for $De = 220$. After a stationary region ($227 < De < 318$) the system suddenly becomes violently chaotic.

full 2D Navier Stokes equations in polar coordinates without low curvature approximation, thus with two control parameters. The bifurcation to the new steady state occurs at $De = 227$ with our model,

which is slightly above the value obtained in Wang and Yang (2004), $De = 217$. The agreement is better for the next bifurcation to chaos, which is observed at $De = 323$ for both models. Nonetheless a difference is observed at the end of the stationary region: in the section between $De = 318$ and 323 our model produces slight periodic oscillations, while Wang and Yang (2004) report an aperiodic oscillation from $De = 312$ until the beginning of the chaotic region at $De = 323$.

The same pattern is observed analysing the injection-velocity phase portraits in figure 3.6. The energy injection is defined as $I = U_b\, dP/dx$, with $U_b = 1$ in the present case. The low De periodicity is characterised by 3 attractors, two of them being the weak and strong 4-vortex solution, as clarified in the following section. Increasing the Dean number we observe more and more clearly the emergence of a fourth attractor. The shape of the envelope remains globally the same, even when the flow enters the chaotic regime (for $De = 200, 220$). After the subsequent stationary part of the bifurcation diagram (between $De = 227$ and 318) the system is again chaotic. In this region we hardly observe the previous envelope, we can nonetheless see the influence of the strong 4-vortex and the high energy attractors.

The periodic regime

Figure 3.7 shows the dependence of the oscillation period on De in the periodic regime. The open circles represent the time intervals between two crossings of the Poincaré section, i.e. the period. As for figure 3.5, the symbols are the superposition of several circles, onto one position for a periodic signal, and two or more in the aperiodic or chaotic regime. At $De > 193$ there is a progressive separation in two different set of circles. This identifies the aperiodicity seen in figure 3.5. Wang and Yang (2004) report $T = 0.159$ at $De = 182.2$, retrieved with the full NS equations while the present model gives $T = 0.1579$ at the same De. Between De_c and $De = 150$ the period dependence on De follows the law:

$$T = \frac{1.013}{(De - De_c)^{0.53}}$$

which is represented with a dashed curve in the figure and is close to a -0.5 power law. This exponent is compatible with a SNIPER bifurcation, which is consistent with the saddle nature of the 2 and 4-vortex fixed points (see Tuckerman (2020) for a detailed discussion). In fact, the computed exponent approaches the theoretical value of -0.5 when the curve fitting is restricted to Dean numbers close to the critical value, in agreement with the weakly non linear framework for the theoretical -0.5 value.

The trajectory approaches and leaves periodically the vicinity of two equilibrium states, where the

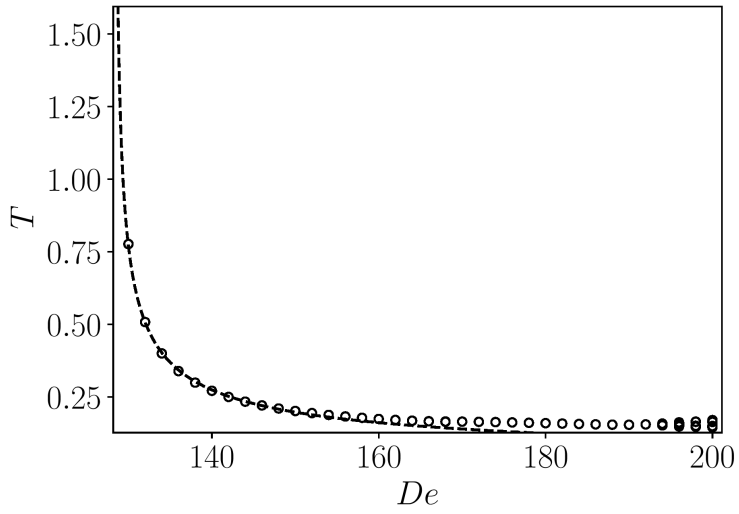

Figure 3.7: The oscillation period follows the law: $T \propto (De - De_c)^{\gamma}$, represented by dashed line, with $\gamma = 0.53$, and $De_c = 128.32$. Above $De \approx 193$ we observe the first part of the aperiodic regime, which gives rise to higher complexity for higher De, see also figure 3.5. dashed curve: 0.962/(De-128.371)**0.5

fluid dynamics slows down and the velocity field resembles that of the equilibrium points. These two equilibria are symmetric with respect to the spanwise direction (z) and are sometimes referred to as the 2 and 4-vortex solutions (Cheng and Akiyama, 1970; Joseph et al., 1975; Winters, 1987; Yanase et al., 1989). The vector fields of these two solutions are shown on the left part of figure 3.9. However the 2 or 4-vortex classification can be misleading, because for $De > 122.5$ the 2-vortex solution presents in truth 4 cells, even if the additional cells are much less intense than those observed in the 4-cell case. This was also observed by Daskopoulos and Lenhoff (1989); Watanabe and Yanase (2013) who named the solutions the weak and the strong 4-vortex solutions.

These streamwise vortices are the result of two different physical mechanisms. First, for confined curved flow, as in a duct or pipe, the acceleration ($-De \cdot u^2$ which is non-homogeneous in the spanwise direction) is in equilibrium with the radial pressure gradient ($\partial p/\partial y$). As a consequence there is a spanwise pressure gradient ($\partial p/\partial z \neq 0$) which induces spanwise flow ($w \neq 0$). This mechanism is responsible for the so-called Dean vortices (Dean, 1927, 1928; Dean and Hurst, 1959) which correspond to the 2-vortex steady solution mentioned above. Secondly, for a flow over a concave wall, when the wall-normal pressure gradient ($\partial p/\partial y$) is strong enough, it can give rise to streamwise counter-rotating

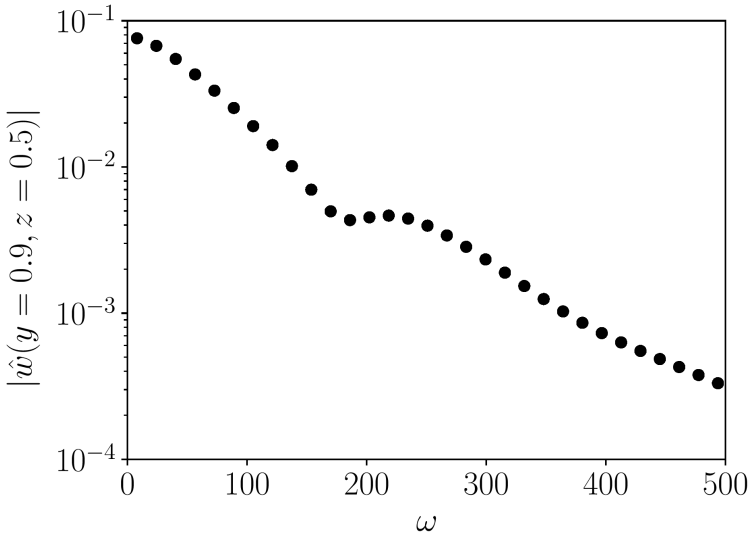

Figure 3.8: Cross stream velocity w spectrum, $De = 130$. The dynamics is dominated by the first mode, which corresponds to a period $T = 0.7764$. Consistently with the observations and the symmetry of the problem, the zero mode vanishes in the spectrum, since the average w vanishes

vortices. This phenomenon is known as the Taylor-Görtler instability. The spanwise wavelength increases with the Reynolds number. The concomitance of these two mechanisms leads to the complexity mentioned above, with the observation of 4 strong or weak cells (Watanabe and Yanase, 2013) and the possibility to observe 6 or more cells for higher Dean number.

Both the weak and strong 4-vortex steady solutions are observed even for subcritical Dean numbers. The strong 4-vortex solution is linearly unstable to non-symmetric perturbations and stable otherwise (Winters, 1987; Bara et al., 1992), whereas for $De < De_c$ the weak 4-vortex solution is linearly stable.

This can be shown by performing a linear stability analysis of those two equilibrium states at De_c, for details about the linear stability analysis and the numerical method the reader is referred to the annex C. The stability analyses are performed by imposing symmetric or anti-symmetric perturbations. Table 3.2 shows the eigenvalues of the most amplified mode for the weak and strong 4-vortex solutions and for symmetric and anti-symmetric perturbations. As in the literature previously mentioned, the strong 4-vortex solution is stable to symmetric perturbations and unstable to anti-symmetric ones. The weak 4-vortex solution is linearly stable to any perturbation in the subcritical regime.

Thus, when the system is non-symmetrically perturbed for $De < De_c$, it evolves close to the strong 4-vortex solution, which is a saddle point. The trajectory is ejected and the system eventually

Table 3.2: Eigenvalue of the most unstable eigenmode of the strong and weak 4-vortex solutions at $De_c = 128.32$, obtained by means of the linear stability analysis. The convergence was stopped when the change in value dropped below 10^{-4}. The eigenvalues can be considered as real, in other words the pulsation is numerically zero.

	Symmetry	Antisymmetry
Strong 4-vortex	$-40.20 + 0i$	$+44.215 - 4.5 \cdot 10^{-4}\ i$
Weak 4-vortex	$-0.540 - 4.6 \cdot 10^{-4}\ i$	$-22.371 - 4.6 \cdot 10^{-4}\ i$

returns to the weak 4-cell solution, which is the global attractor. This is the reason why the latter is the solution observed in direct numerical simulations or experiments in the subcritical regime. When the system is non-symmetrically perturbed for $De > De_c$, the weak 4-vortex solution being linearly unstable; a perturbation will therefore initiate a cycle between the two solutions. The periodic orbit of the system at $De = 130$ is depicted in figure 3.9 in a state space diagram spanned with the energy injection and squared velocity 2-norm. The system follows the direction indicated by the small arrow in the center of the figure. Starting in the proximity of the weak 4-vortex solution (indicated with the black circle at the bottom left) the flow evolves towards the strong 4-vortex solution (indicated with the black square at the top left). The system then loses its symmetry, which is consistent with the instability to asymmetric perturbations of this solution. The two upper vortices collapse into one lateral vortex, producing a burst. The system then rapidly returns to a symmetric state, namely the weak 4-vortex solution.

The trajectory is attracted by the stable manifold (symmetric) of the strong 4-vortex equilibrium, it then leaves this region along the unstable manifold (antisymmetric) and heads to the second equilibrium state (weak 4-vortex). If $De > De_c$, then the trajectory follows the second heteroclinic orbit along the unstable manifold (symmetric) of the weak 4-vortex equilibrium. It then heads to the strong 4-vortex equilibrium state, closing the cycle. These two heteroclinic orbits between the two equilibria constitute a heteroclinic cycle which can be suppressed by imposing lateral symmetry.

High Dean regime, De = 10^4

For Dean numbers of $\mathcal{O}(10^2)$ or lower the complexity of the system is strictly temporal. The spatial patterns always present two main Dean cells, possibly with the additional (2 or more) Görtler vortices. The evolution in time can give rise to aperiodic or chaotic patterns, among quite regular spatial solutions. In this section we introduce a relatively high Dean number simulation, at $De = 10^4$.

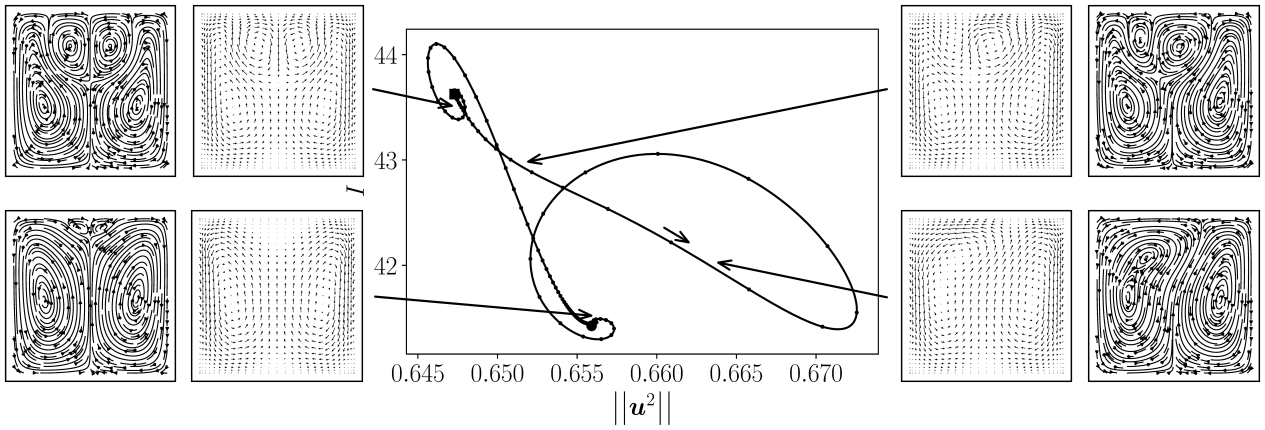

Figure 3.9: Injection-velocity norm phase diagram at $De = 130$. The system follows a periodic orbit passing close to the 2 stationary solutions, indicated by the solid circle ($I \approx 41.5, ||\boldsymbol{u}||_2^2 \approx 0.655$) and the solid square (($I \approx 43.5, ||\boldsymbol{u}||_2^2 \approx 0.647$)). The long arrows indicate the instantaneous states of the system. The flow evolves following the small arrow: from the weak 4-cell, symmetric state to the symmetric strong 4-cell one. When symmetry is broken a kinetic energy burst is observed. The system then returns to a weak 4-cell state regaining its symmetry.

The numerical parameters needed to be adapted $Ny = Nz = 501$, $\Delta t = 10^{-8}$. Figure 3.10 shows a snapshot of isocontours of the streamwise velocity u. As can be seen the topology changes drastically as compared to the 2 or 4-cell solutions observed so far at much lower Dean number (figure 3.9). Such a high De in a 2D configuration makes this case a purely theoretical problem, since we can expect to have a turbulent state in a full 3D pipe at this Dean (and thus Reynolds) number. It is nonetheless interesting to observe such a level of complexity deriving from a single forcing term in an otherwise stationary problem.

Three dimensional flow

Orders of magnitude

The hypotheses on which the present formulation is based are those presented in (3.4). The integral term in the continuity equation (3.3a) is neglected, thus

$$\frac{v}{R} \sim \frac{V}{R} \ll \frac{U_b}{L} \sim \frac{\partial u}{\partial x}$$

rearranging the expression and dividing both terms by h we obtain

$$\frac{L}{h} \ll \frac{U_b}{V}\frac{R}{h}$$

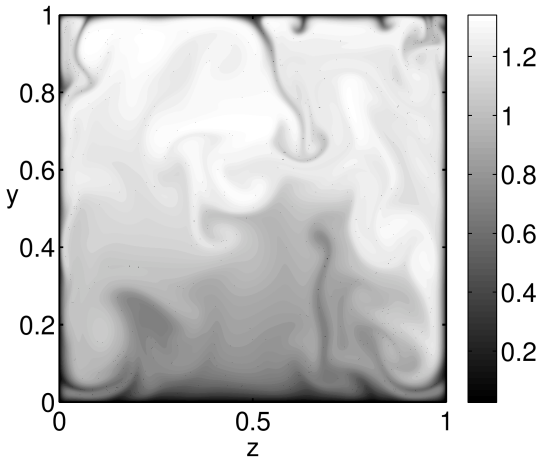

Figure 3.10: Isocontour of the streamwise velocity u. Snapshot of simulation at $De = 10^4$

using the scaling laws in 3.4

$$\frac{L}{h} \ll \varepsilon^{-3} = \left(\frac{Re}{De}\right)^3$$

This means that for the model to be applied the non dimensional domain length must be small with respect to ε^{-3}. For the Dean and Reynolds numbers involved in these analyses this hypothesis does not represent a major constraint. For a puff at $Re = 1500$ and a supercritical Dean number $De = 150$ we have $L \ll 1000h$. A length of $100h$ is sufficient for all the cases presented in this thesis, and complies with the requirement given by the low curvature hypothesis.

Entry flow development

An interesting application for the present model concerns the flow development problem, namely a straight, laminar flow entering in a curved section. Since curved tubes in engineering applications are often too short for flows to reach the fully developed state, the formulation of transport mechanisms should portray developing conditions. The parabolic equations are solved using a parabolic adaptation of the code that uses the McCormack scheme (MacCormack, 2003), which is described in appendix B. We use a no-slip boundary condition at the walls and we impose the straight laminar flow profile at the inlet. No boundary condition is required at the outflow due to the convective nature of the equations. The simulations are performed considering a domain of length $16.5h$ on a grid composed of 101 Chebyshev points in both wall normal directions and 200 equispaced points in the streamwise direction. The time-step is $dt = 1 \cdot 10^{-5}$ non dimensional time units. The divergence free condition is

enforced by means of the prediction-projection scheme by Chorin-Temam (see section 2.1.4.1), however due to the parabolic nature of the equations this method is not very effective. The divergence does not reach machine precision but remains within reasonable limits (of order 10^{-7}).

Figure 3.11 shows the variation of the streamwise velocity u along the streamwise direction at $y = 0.74$, $z = 0.5$, hence towards the middle of the top half of the domain in the radial direction y, and in the centre in the span-wise direction z. The circles represent the experimental measurements by Bara et al. (1992), for consistency the streamwise direction is rescaled to obtain the azimuthal coordinate $\theta = x/R$, using the same $h/R = 1/15.1$ ratio employed in the reference. At $De = 125$ the 2D flow is stable, except for an initial adaptation over about 50 degrees the 3D flow assumes a constant profile, which is invariant in x and corresponds to the stable, weak 4-vortex branch. At $De = 137$ or 150 the 2D flow is unstable, this results in an oscillation in 3D between the weak and the strong 4-vortex solutions, this time occurring along the streamwise coordinate, as also observed in Sankar et al. (1988). The strong 4-vortex solution is characterised by a lower streamwise velocity in the point examined compared to the weak 4-vortex solution, due to the presence of the vortices themselves, hence the lower velocity branch corresponds to the strong 4-vortex attractor, the upper branch is the weak 4-vortex solution. Bara et al. (1992) compare the experimental results with those obtained numerically with a parabolic solver (not shown in the figure for clarity). The agreement of the present results with the experiment lies within the difference between the model by the authors and the experiments, furthermore, we notice that many of the differences between the calculations and the experiments shown in the reference are almost perfectly reproduced by the present model, this quite evident for the case $De = 137$ at $\theta \sim 200$, the discrepancy between experiments and model observed in figure 3.11 is equally observed in reference Bara et al. (1992).

The parabolic solver used in the reference had been previously employed by Sankar et al. (1988), it solves the steady-state cylindrical Navier-Stokes equations, the only neglected terms are the streamwise diffusion terms, dropped to ensure the parabolicity of the problem. The very good accordance between the models and with the experiment demonstrates that the Dean model is capable of capturing all of the laminar flow features, eliminating the complexity of solving the cylindrical Navier Stokes equations by allowing the use of a cartesian solver. As well as the model by Sankar et al. (1988) the present model can be used for spirals, or S-like geometries just by providing the desired law of dependece $De(x)$. Moreover the present model is time dependent, as such it can be readily employed to solve

problems with moving or elastic walls (Dean varying with x and time) or with time dependent inflow conditions.

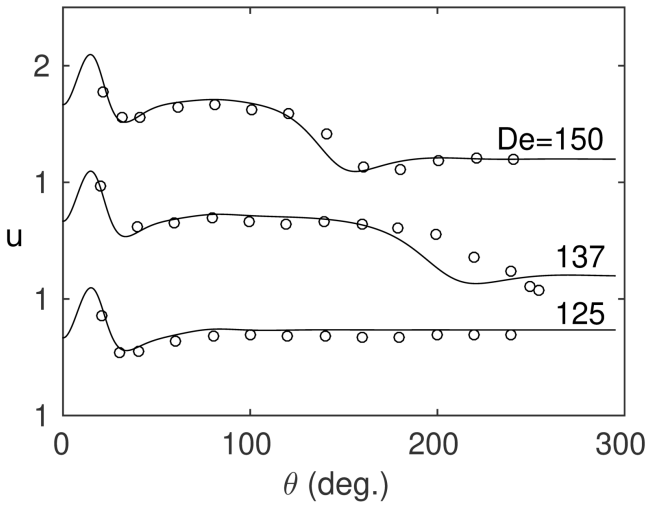

Figure 3.11: Streamwise velocity at $y = 0.74, z = 0.5$ for $De = 125, 137, 150$, 3D flow development problem with straight, laminar inflow. Computed with the present parabolic model (lines), compared with the experiments by Bara et al. (1992) (circles)

The traveling wave solution

Equations (3.5) are solved in 3D using the very same spectral, streamwise periodic solver described in chapter 2, and not the MacCormack solver mentioned above, which has been used for the flow development solutions. The spectral solver has been adapted with little modifications consisting specifically in adding De that multiplies the nonlinear term, in dropping the diffusion term and the pressure gradient in x. A traveling wave in curved square duct flows has been described by Mees et al. (1996), but an early observation of laminar oscillations in coiled ducts dates back to G. I. Taylor (1929). The numerical solution of the present model also results in a travelling wave in the same range in which in 2D we observed periodic oscillations. Figure 3.12 shows an isosurface of the absolute value of the local streamwise helicity

$$H = \sqrt{\left[\left(\frac{\partial v}{\partial z} - \frac{\partial w}{\partial y}\right) u\right]^2}$$

very similar to the observations by Watanabe and Yanase (2013), who confirmed that the bifurcation from the steady state to the oscillating is supercritical.The flow goes from the bottom left to the top right of the figure, for most of the simulation it resembles closely the strong 4-vortex solution of the 2D

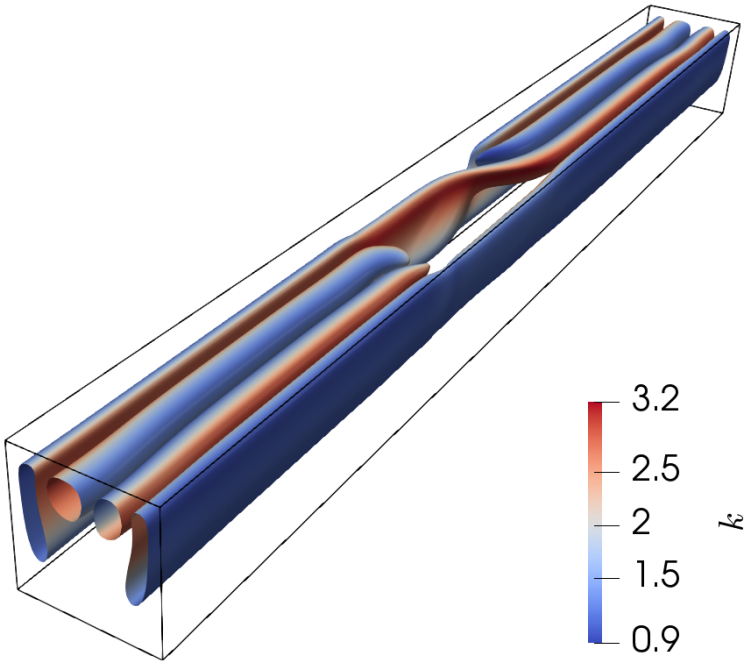

Figure 3.12: Constant helicity iso-surface, curved duct simulation $L = 2\pi$ in the periodic regime ($De = 130$), coloured with the flow kinetic energy. The flow goes from the bottom left to the top right of the figure.

case. The flow oscillates periodically towards the weak 4-vortex solution as we see towards the middle of the figure, to quickly regain the strong 4-vortex configuration. The travelling wave behaviour was also more recently reported by Canton et al. (2020); Kühnen et al. (2015), who in addition observed a supercritical transition to turbulence for large enough curvatures. However they did not clarify the relationship between their findings and the previously known travelling wave behaviour, in other words it is unclear if the supercritical transition is actually a supercritical departure from the laminar, oscillating flow of the travelling wave, or if the transition that they observe is instead the supercritical bifurcation towards the travelling wave regime, and the transition to turbulence is a further step, which at this point would be debatable to define supercritical.

Turbulent puffs in curved duct flows

The Dean model is limited to laminar flows due to the parabolic nature of the equations in 3D. In this section we make a further assumption, namely that for a weakly curved duct the turbulent scales

are not directly affected by curvature, which only acts on the zero mode. We write a perturbative version of the Navier-Stokes equations in which the velocity components

$$u_i = U_i + u_i'$$

U_i is the Dean flow, which is in general unsteady and is computed with the extended Dean model, in which $L = \sqrt{hR}$. The fluctuations u_i' are computed with the classic Reynolds non dimensionalisation where $L = h$. The turbulent flow is indirectly influenced by curvature via the deformation of the Dean flow. The mean streamwise pressure gradient this time is not adjusted to keep the bulk velocity to 1, but to 0, since this condition is already ensured by the Dean flow. Therefore the pressure gradient is given by the sum of the Dean pressure gradient, which is constant in the case of a subcritical Dean flow ($De < 128$), and the pressure gradient needed to balance the pressure drop due to the turbulent activity. We inject a turbulent puff at $Re = 1600$ on flows at different Dean numbers.

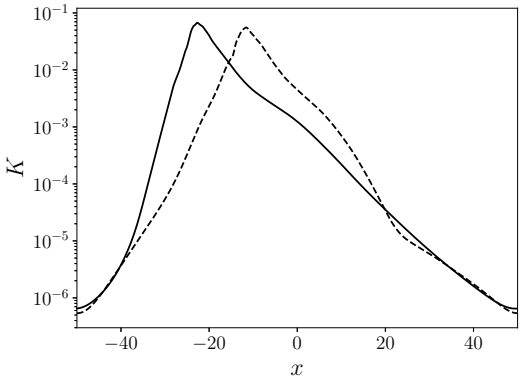

Figure 3.13: Cross section averaged turbulent kinetic energy along x, for De=0 (straight duct, continuous line) and De=30 (bent duct, dashed line).

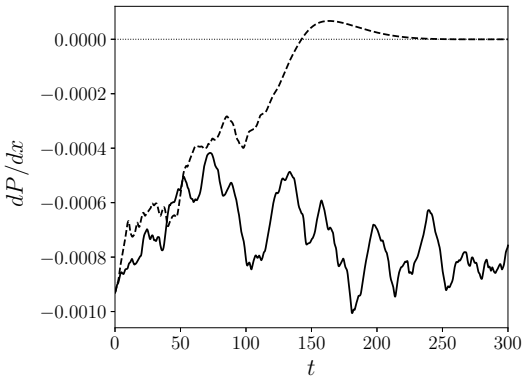

Figure 3.14: Turbulent pressure loss, for De=35 (continuous line) and De=40 (dashed line).

For $De < 128$ the Dean flow is stationary, the 'mean' flow of the perturbative equations is actually time invariant. It must be noted that this does not mean that the total zero mode is time invariant, since the turbulent fluctuations do have a zero mode component that can substantially modify the resulting zero mode. Only in the limit of an infinitely long duct is the zero mode constant and equal to the Dean component, since the fluctuations become negligible. The simulations were performed on a $51 \times 51 \times 1024$ points grid, with a stationary Dean component of the zero mode. The velocity components in the Dean flow have a different non dimensionalisation with respect to the turbulent

field, therefore they must be rescaled to comply with the scaling of the latter. The turbulent puffs in figure 3.13 are computed for $Re = 1600$ and $De = 0$ and 30. The presence of a curvature makes the upstream front less abrupt, and the turbulent energy peak lower (this is only slightly visible due to the log scaling) in qualitative agreement with the observation by Rinaldi et al. (2019) in a toroidal pipe of circular cross section. Figure 3.14 shows the time history of the streamwise pressure gradient of the turbulent component for a turbulent puff at $De = 35$ and $De = 40$. In the first case the puff survives for a very long time while in the second it relaminarises after about 150 time units. A zero turbulent pressure loss means that the total pressure loss equals the one of the Dean flow, thus the puff has relaminarised. The two simulations were run several times using different initial conditions, specifically the initial condition for both cases was the last available solution for $De = 35$. One might think that the cause for the death of the puff at higher De is due to the shock given by the sudden change in curvature. However the change in De is not very strong, moreover the puff survives for several time units before rapidly dying, enough to assume that the initial condition has been forgotten. The cause of the death of the puff is related to the presence of the Dean vortices. Figure 3.15 shows the $y = 0.5$ streamwise velocity of the stationary Dean flow at $De = 30$. The maximum in velocity is shifted towards the outer, convex wall and the whole profile is modified with respect to the straight case. The mean velocity gradients are thus less strong at the lower wall, where in addition the turbulent fluctuations tend to be transported away, towards the center of the domain. Close to the outer wall the gradients are stronger, this is probably the zone where most of the turbulent production takes place (Rinaldi et al. (2019) found that the linear and non linear optimal perturbations are concentrated in this zone). However such deformation of the mean velocity profile implies that the strong gradient is concentrated in a zone closer to the wall, when compared to the straight case. Therefore it is more difficult for sufficiently strong, hence not damped, turbulent fluctuations to be amplified by the mean velocity gradient, also considering that there is the possibility that such fluid parcel is washed away by the vortices. This mechanism is very similar to the one discussed in section 2.3.2, here however the mean profile is not modified by the non linear term and thus 'worn' by turbulence, but is instead modified by the Dean vortices. This phenomenon is present for any Dean number, but becomes more and more pronounced as De increases. In this sense, while the Reynolds number is a governing parameter that control the statistical probability of a puff to survive (Avila et al., 2011), the Dean number is a more deterministic quantity, in the sense that for a given Reynolds number we can control

the life and death of a puff within about 100 time units.

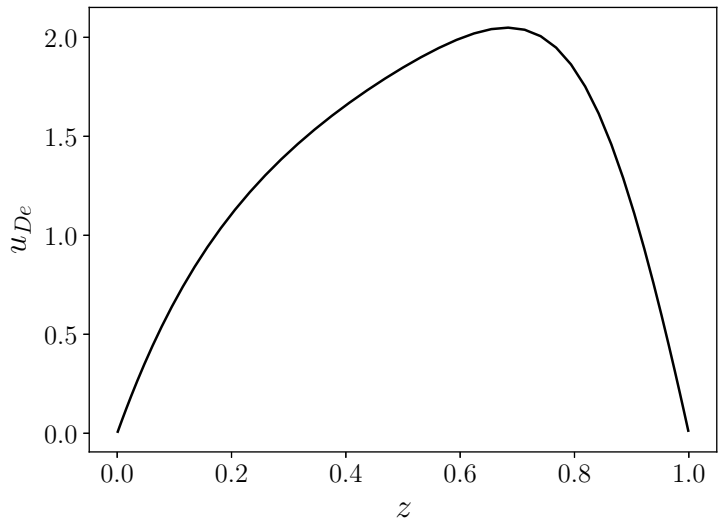

Figure 3.15: $y = 0.5$ streamwise velocity profile of the stationary Dean flow, $De = 30$.

The viscous stress probability density functions (PDF) in figure 3.16 for the straight case (dashed line) and $De = 30$ (continuous line) are qualitatively not very different from each other. The main differences are a change in slope in the high and low τ regions, with a faster decrease for the curved case. This implies a diminished turbulent activity in the near wall regions, probably due to the convective effect of the Dean vortices. The $\tau < 0$ region is particularly important, since it is necessary for the generation of the Kelvin-Helmholtz vortices. In the curved case the probability of having a low speed streak seems to be diminished, which might explain the death of the puff for $De = 40$. As per the discussion of figure 2.5, this highly peaked part of the PDF is given by the laminar portion of the flow. This region is larger in the curved case, which is explained by the fact that the two lateral walls produce an analogous PDF, while the upper and lower walls have different values of τ, thus occupying a larger part of the figure. Figure 3.17 shows the fraction of the section with $u > U_b$ for the curved and straight cases. It might appear surprising that the puff in the straight duct (dashed line) seems to have a longer downstream front. This is probably due to a localisation of the turbulent activity near the convex wall in the curved case, in which a part of the section shows less turbulent activity. Other differences are the A^+ fraction of the laminar region, which is higher in the curved case, and the shape of the upstream front. The front at $De = 30$ looks as abrupt as the one in the straight case, however from figure 3.13 we clearly see a difference in the turbulent energy slope exists.

The shorter downstream front, and the strong upstream front are somewhat inconsistent with the expectations and previous observations. These are probably due to a limit of this kind of analysis, which is binary, and does not quantitatively represent the turbulent activity. The low A^+ peak at the upstream front however is consistently present, even for the curved case. This might be used to less arbitrarily determine the position of the upstream front.

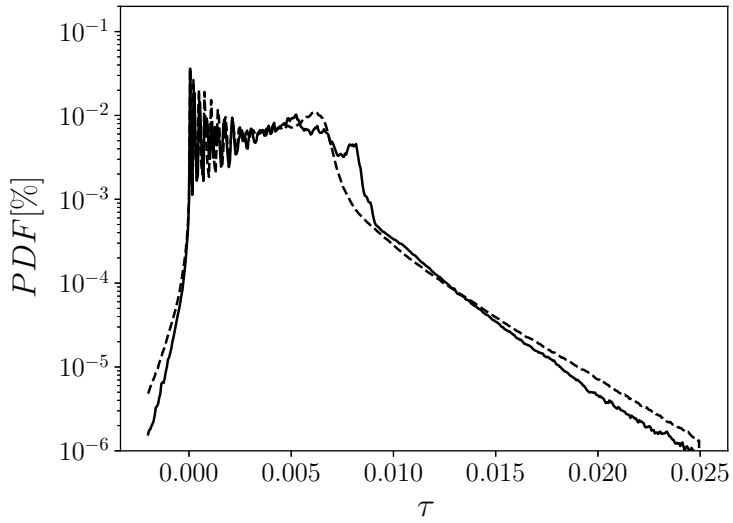

Figure 3.16: Probability density function (PDF) of the wall shear stress computed for a puff at $Re = 1600$ in a bent duct at $De = 30$ (continuous line) and a straight duct ($De = 0$, dashed line).

This model has the advantage of separating the laminar effects of Dean and the turbulent features governed by the Reynolds number. In recent years particular attention has been devoted to the study of turbulent puffs in curved pipes, both experimentally (Kühnen et al., 2014; Kühnen et al., 2015) and numerically (Rinaldi et al., 2019; Canton et al., 2020). However these studies use a given set of curvatures and vary the Reynolds number. This strategy is justified by the extra work needed to reconstruct the geometry for each variation in curvature, this can imply a considerable amount of work for a CFD study, and can be a very long and economically expensive task for an experimentalist. When using this approach however it is hard to discriminate the Dean and Reynolds effects. Increasing the Reynolds number for a given geometry impacts both the turbulent features and the shape of the underlying laminar flow, since also the Dean number varies ($De = Re\sqrt{h/R}$). Most importantly, some confusion may arise regarding the non stationarities. The travelling wave appears via a supercritical bifurcation, but the flow remains laminar. As long as the transition to turbulence is concerned, it

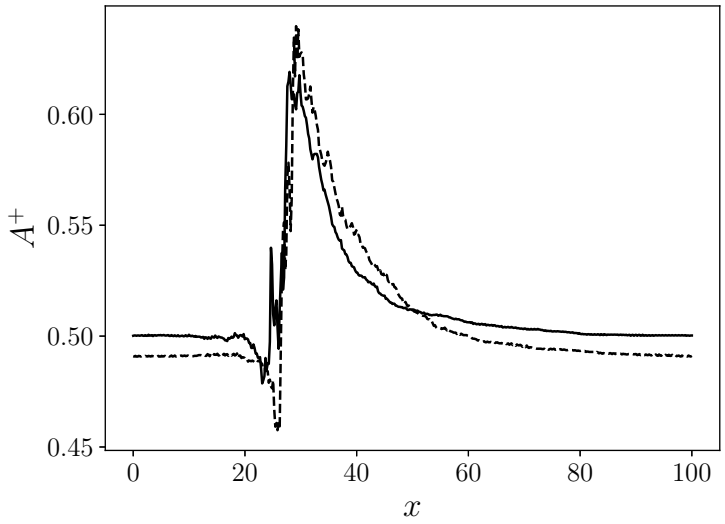

Figure 3.17: $u > U_b$ area fraction for a puff at $Re = 1600$ in a bent duct at $De = 30$ (continuous line) and a straight duct ($De = 0$, dashed line).

has not yet been clarified whether it is of subcritical or supercritical nature, since the Dean and the turbulent components are hard to separate in a DNS or in an experiment.

Chapter 4

The acoustic field generated by a turbulent puff

Table of contents of this chapter

Introduction

This chapter deals with the acoustic field generated by a puff. Acoustics is a compressible phenomenon, and is not included in the incompressible formulation used so far. The use of acoustic analogies (described in more detail in the following pages) allows us to relate the turbulent flow field with the radiated noise. In a few words, the acoustic analogy is a rearrangement of the compressible NS equations, the result being a inhomogeneous wave equation in which the right hand side contains all the flow quantities. If the incompressible solution is a good representation of the real flow, it can be used to compute the radiated sound (Crow, 1970).

The first motivation behind the work presented in this chapter is the question: is there an equilibrium distance between puffs? This subject has been presented in section 2.3.2. In brief, turbulent puffs are known to interact when they are too close together, the upstream puff 'pollutes' the laminar flow needed by the downstream puff to produce the turbulence it requires to survive. This can result in the death (relaminarisation) of the downstream puff, or in its migration further downstream, in a zone where the flow has had more room to recover the laminar profile, and the gradient of the mean velocity is more favorable for turbulent production. This process is hydrodynamical, and acts only at close range. It is unclear if a long range equilibrium distance exists. This would probably not be based on hydrodynamical processes. We want to investigate whether or not there exists an acoustic wavelength compatible with a long range inter-puff distance. Judging from the present calculations such a frequency does not seem to exist, suggesting that an equilibrium distance dependent on an interaction based on acoustics is not there.

The study of the aeroacoustic field of a turbulent puff may also provide some elements on the question concerning the importance of the wall viscous stresses in the noise radiated by turbulence. This subject has long been debated in the literature, the central problem is whether the viscous stress fluctuations are a source of sound or act only as a propagation effect (see section 4.1.2 for a review). The viscous contribution is often neglected since, at high Reynolds numbers, the importance of the viscous stresses can be expected to be small. However the noise intensity of the viscous contribution

decreases with the Mach number (Ma) much more slowly than the Eulerian noise (which is usually dominant). This means that there can be a -quite low- Mach number at which the viscous noise becomes dominant on the Eulerian noise. A low Reynolds number flow may be a good candidate for the study of such phenomenon, given the higher importance of viscous effects. Moreover in practical terms a low Re also means low Ma. The puff is the best example of low Re turbulence, as it survives on the edge of relaminarisation. Moreover the spatial localisation makes it a very handy case for the use of acoustic analogies, in which the turbulent region must be separated from the propagation zone. Hu et al. (2003) provided the only study on the aeroacoustics of sustained turbulence at low Ma in plane Poiseuille and plane Couette flows. Both these configurations have an infinite spanwise direction. Computing the noise of an infinitely large turbulent channel would give infinite radiated pressure (this problem is known as the Olber paradox); the authors effectively avoid the problem by computing the noise radiated per unit area. One of the reasons why the present configuration is well posed for aeroacoustics is that this inconvenient does not appear due to the localisation both in the spanwise and streamwise direction of the turbulent region.

Computing airborne noise

Only a small fraction of the energy of a turbulent flow is radiated as sound. This is the reason why acoustic waves, which are formally contained in the compressible Navier-Stokes equations, are not easy to detect even when relying on high fidelity and expensive numerical tools such as Large Eddy Simulation (LES) or Direct Numerical Simulation (DNS). Any filtering, such as artificial dissipation or numerical dispersion that would not affect the hydrodynamic fluctuations can result in the dissipation of the acoustic waves. A method aimed at directly calculating the noise radiated by turbulence requires that both the sound radiating turbulent flow region and at least a part of the sound propagating zone are included in the computational domain. Moreover particular attention must be paid to the boundary condition and to the possibility that any numerical fluctuation may represent a sound source stronger than the physical, turbulent source. For these reasons computing the noise generated by a turbulent flow directly from the NS equations is a very expensive and complex task. Direct Noise Computation (DNC) remains however a powerful tool for aeroacoustic research. Mitchell et al. (1995) computed directly the noise generated by a pair of co-rotating vortices, this work allowed a validation of the aeroacoustic theory developed in the early stages of research on airborne noise (Lighthill, 1952; Powell,

1964; Howe, 1975). Other techniques use the pressure fluctuations computed on a surface placed in the acoustic near field to extrapolate the noise radiated in the far field, either via the linearized Euler equations (Bailly and Juvé (2000)), or using Kirchhoff surface integral approach (an extensive review on the subject of the Kirchhoff extrapolation is provided by Lyrintzis (1994)). These techniques are known as wave extrapolation methods (WEM). Another approach is the use of hybrid methods. These methods use the hydrodynamic flow field to predict the radiated noise, which is thus not a direct result of the simulation. These techniques do not have the same grid requirements of the DNC, at the cost of an additional computing step. The key point consists in seeing the non linear turbulent field as the forcing term of a linear wave equation. The wave operator accounts for the sound wave propagation, therefore the compressibility effects are not required for the transport of the sound waves. It is thus possible to predict the noise of a low Ma turbulent flow computed using an incompressible formulation.

Sound radiation in low Mach flows

Most numerical studies of airborne noise neglect the dipolar and monopolar noise contributions considering only the quadrupolar noise related to the Reynolds stresses, as suggested by Lighthill (1952). Some authors however have investigated the role of viscosity in the noise generation. Mitchell et al. (1995) computed the noise radiated by a two co-rotating vortices at low Re. Due to the absence of walls the contribution of viscosity only appears in the quadrupolar term, which is associated to turbulent dissipation (Kambe, 1984) and is shown to be negligible in accordance with Obermeier (1985). A stronger contribution by the viscous effects may be expected in the dipolar term of a wall bounded flow. In the case of an infinite plane Powell (1960) showed that the dipolar term involving the pressure in Curle's analogy (Curle, 1955) was not a source of sound but represented instead the image quadrupoles (i.e. quadrupoles positioned by mirroring the volume quadrupoles with respect to the surface). By using a Green's function with vanishing normal derivative at the surface the dipolar term vanished, and one could compute the noise radiated by, say, a turbulent boundary layer only using the quadrupolar sources, and their mirrored image. This formulation is formally valid only for inviscid flows, since $\frac{\partial p}{\partial n} = 0$ at the surface due to the Green's function (Howe, 1979). Shariff and Wang (2005) showed that it remains valid even for viscous flows provided that the noise is not radiated at wall grazing angles. Wang et al. (1996b) computed the noise generated during the breakup of a laminar incompressible boundary layer, relating each phase of the transition to the corresponding radiated noise

by arguing that the dipolar contribution could be predominant at low Mach numbers. The acoustic intensity given by the dipolar contribution scales decreases with Mach with an exponent smaller by 2 with respect to the quadrupolar volume components, thus for low Ma the dipolar component intersects the quadrupolar one and becomes dominant. Hu et al. (2003) computed the noise generated by incompressible turbulent plane Poiseuille and plane Couette flows by means of an acoustic analogy finding a crossing point around $Ma = 0.01$ for the first and $Ma = 0.1$ for the second. Hu et al. (2006) later adapted the plane Poiseuille flow case to compare with the diffuser experiments by Greshilov and Mironov (1983) at $Ma = 0.008$, obtaining a reasonable agreement at high frequencies.

Interpretation of the viscous term

The interpretation of the dipolar term accounting for the noise generated by the fluctuating viscous stresses has long been a matter of debate. According to Howe (1979) the viscous stresses interfere with the propagation of sound waves acting as a damper. Their effect should be included in the propagation operator, but they are not per se an acoustic source. That study however does not include the surface viscous shear stress given by the turbulent motions among the noise sources, only considering them as acoustic modes given their low frequency. Nevertheless turbulent fluctuations can also have strong low frequency components, as reported by Wang et al. (1996b) in the case of a boundary layer breakup, or in the present case of sustained low Re turbulence (see for instance figure 4.12). Hariri and Akylas (1985) included both the acoustic and hydrodynamic components, finding an actual contribution of the viscous stresses in the sound generation. This is in accordance with Landahl (1975), who argued that the noise generation is linked with the hydrodynamic fluctuations near the wall. If this is the case we should be allowed to compute the noise generated by the fluctuating viscous stresses using a dipole distribution in the same way that we use a quadrupole distribution for the volumic term. In order to test the importance of the dipolar noise the investigation should be carried out at low Mach numbers. Thus the use of an incompressible formulation is advantageous, since the same computation is valid for any Ma, which can be included in post-processing. Later Morfey (2003) showed analytically that regarding the viscous stresses as source term of an acoustic analogy with an inviscid wave operator reproduces both the sound generation and the damping of incident acoustic waves in a plane boundary configuration. Shariff and Wang (2005) performed a numerical experiment with a moving surface, computing the noise directly from the Navier Stokes equations. The noise

generated was dipolar and in agreement with an analogy calculation.

Lighthill's analogy

Lighthill's equation

Ligthill's theory of airborne noise (Lighthill (1952)) consists in determining an analogy between a problem governed by the Navier-Stokes equations and the acoustic theory. Manipulation of the momentum and continuity equations allows to write an inhomogenous wave equation in which the right hand side contains the information concerning the turbulent flow.

We assume that the turbulent activity is concentrated in a given volume and that the listener is placed outside this volume, far enough to be in a zone where the flow is at rest. The Navier-Stokes equations are

$$\frac{\partial \rho}{\partial t} + \frac{\partial \rho u_i}{\partial x_i} = 0 \tag{4.1}$$

$$\frac{\partial \rho u_i}{\partial t} = -\frac{\partial \pi_{ij}}{\partial x_j} \tag{4.2}$$

Where

$$\pi_{ij} = p\delta_{ij} + \rho u_i u_j - \tau_{ij}$$

and

$$\tau_{ij} = \mu \left(\frac{\partial u_i}{\partial x_j} + \frac{\partial u_j}{\partial x_i} - \frac{2}{3} \frac{\partial u_k}{\partial x_k} \delta_{ij} \right)$$

is the viscous stress tensor. In the listener region we have

$$\pi_{ij}^{\infty} = (p - p_{\infty})\delta_{ij} = c_{\infty}^2 \left(\rho - \rho_{\infty}\right) \delta_{ij}$$

We can rewrite the momentum equation in the turbulent region as

$$\frac{\partial \rho u_i}{\partial t} = -\frac{\partial \pi_{ij}^{\infty}}{\partial x_j} - \frac{\partial}{\partial x_j} \left(\pi_{ij} - \pi_{ij}^{\infty} \right) \tag{4.3}$$

and also

$$\frac{\partial \rho u_i}{\partial t} + c_{\infty}^2 \frac{\partial \left(\rho - \rho_{\infty}\right)}{\partial x_i} = -\frac{\partial}{\partial x_j} \left(((p - p_{\infty}) - c_{\infty}^2(\rho - \rho_{\infty}))\delta_{ij} + \rho u_i u_j - \tau_{ij} \right) = -\frac{\partial T_{ij}}{\partial x_j} \tag{4.4}$$

Where T_{ij} is the Lighthill tensor. By differentiating in time (4.1) and subtracting the result to the divergence of (4.4) we obtain

$$\begin{array}{ll} \dfrac{\partial^2 (\rho - \rho_\infty)}{\partial t^2} + \dfrac{\partial}{\partial t}\dfrac{\partial \rho u_i}{\partial x_i} = 0 & - \\ \dfrac{\partial}{\partial x_i}\dfrac{\partial \rho u_i}{\partial t} + c_\infty^2 \dfrac{\partial^2 (\rho - \rho_\infty)}{\partial x_i^2} = -\dfrac{\partial^2 T_{ij}}{\partial x_i \partial x_j} & = \\ \hline \dfrac{\partial^2 \rho}{\partial t^2} - c_\infty^2 \dfrac{\partial^2 (\rho - \rho_\infty)}{\partial x_i^2} = -\dfrac{\partial^2 T_{ij}}{\partial x_i \partial x_j} & \end{array}$$

Which can be rewritten as the Lighthill equation

$$\left(\frac{\partial^2}{\partial x_i^2} - \frac{1}{c_\infty^2}\frac{\partial^2}{\partial t^2}\right)\left[c_\infty^2 (\rho - \rho_\infty)\right] = -\frac{\partial^2 T_{ij}}{\partial x_i \partial x_j} \tag{4.5}$$

or, in terms of pressure fluctuations, in the isentropic limit

$$\left(\frac{\partial^2}{\partial x_i^2} - \frac{1}{c_\infty^2}\frac{\partial^2}{\partial t^2}\right) p' = -\frac{\partial^2 T_{ij}}{\partial x_i \partial x_j} \tag{4.6}$$

This equation is exact, however it contains 5 unknowns and thus it cannot be solved unless some hypotheses are made. We will hypothesize that the listener is placed in a zone where the fluid is uniform and at rest, except for the linear density/pressure perturbations, which represent the acoustic field generated by the nonlinear turbulent region.

The Lighthill tensor are most of the times drawn from a numerical simulation of the flow. A well resolved DNS provides almost all the turbulent scales, but in the cases where one is interested in the noise produced by the large structures of turbulence a LES can be used. The Lighthill tensor can also be computed from experimental data, collected for instance by means of PIV, see Koschatzky et al. (2011). In the cases where very slow evolving turbulent structures are concerned even unsteady RANS simulations can be used (Bailly and Bogey (2004)).

Interpretation of the Lighthill tensor components

The Lighthill tensor can be divided in 3 components that represent sound sources of different nature

$$T_{ij} = \underbrace{\left[p - p_\infty - c_\infty^2(\rho - \rho_\infty)\right]\delta_{ij}}_{i} - \underbrace{\tau_{ij}}_{ii} + \underbrace{\rho u_i u_j}_{iii} \tag{4.7}$$

1. The entropic term. The double divergence of this term represents the convection of non uniformities in density or compressibility, which can be given for instance by combustion or heat transfer effects. In cases where such effects are not observed, this term is often neglected. Its effects have been studied by Morfey (1973).

2. The viscous term. Represents the noise production given by the fluctuations of the viscous stress tensor. It is often neglected at high Reynolds number or in the absence of walls. It can be a source of sound in particular situations (Morfey et al., 2012).

3. The non linear term. This is commonly the most important term, its double divergence represents the nonlinear convection of momentum.

Green's function

The Green's function is defined as the impulse response of a linear operator with given initial and boundary conditions. The general idea is that if we have a problem of the kind

$$Lu(x) = f(x)$$

with a linear operator L, if we define a Green's function G such that

$$LG(x-y) = \delta(x-y)$$

we can write

$$\int LG(x-y)f(y)dy = \int \delta(x-y)f(y)dy = f(x)$$

The operator L is linear and acts on x, therefore it can be taken out of the integral

$$L\int G(x-y)f(y)dy = f(x)$$

By comparing this equation with the starting problem we see that

$$u(x) = \int G(x-y)f(y)dy \tag{4.8}$$

is a solution of the problem. We should note that this solution is the convolution of G and f.

Green's function for the wave equation

In our case the linear operator is the wave operator

$$\frac{\partial^2}{\partial x_i^2} - \frac{1}{c_\infty^2}\frac{\partial^2}{\partial t^2}$$

We have, for an impulse occurring in y at the time τ, that the response G in x, at the time t is given by

$$\frac{\partial^2 G(\mathbf{x},t|\mathbf{y},\tau)}{\partial x_i^2} - \frac{1}{c_\infty^2}\frac{\partial^2 G(\mathbf{x},t|\mathbf{y},\tau)}{\partial t^2} = \delta(\mathbf{x}-\mathbf{y})\delta(t-\tau) \tag{4.9}$$

As is customary, we will henceforth denote with x_i and y_i the coordinates in the listener domain and the source domain, respectively. G also respects the boundary conditions at the edges of the domain, on the surface Σ, which has an externally directed normal $\mathbf{n}$. If Σ is placed at infinity we have the free space Green's function. If the boundary conditions of the Green function correspond to the boundary condition of the problem we have the exact, or tailored Green's function. In general we have

$$\frac{\partial G}{\partial \mathbf{n}} + \alpha G = 0 \tag{4.10}$$

Being G the response at time t to an impulse occurred at time τ, we have the causality conditions:

$$G = 0 \qquad \frac{\partial G}{\partial t} = 0 \qquad \text{for } t \leq \tau$$

Solution of a wave equation with a source term $Q(x,t)$

The general solution of the inhomogeneous wave equation

$$\frac{\partial^2 \psi(\mathbf{x},t)}{\partial x_i^2} - \frac{1}{c_\infty^2}\frac{\partial^2 \psi(\mathbf{x},t)}{\partial t^2} = Q(\mathbf{x},t)$$

is

$$\begin{aligned}\psi(\mathbf{x},t) = &\int_{t_0}^{t}\iiint_V Q(\mathbf{y},\tau)G(\mathbf{x},t|\mathbf{y},\tau)d\mathbf{y}d\tau \\ &- \int_{t_0}^{t}\iint_\Sigma \left(\psi\frac{\partial G}{\partial y_i} - G\frac{\partial \psi}{\partial y_i}\right)n_i dS(\mathbf{y})d\tau - \frac{1}{c_\infty}\left[\iiint_V \left(\psi\frac{\partial G}{\partial \tau} - G\frac{\partial \psi}{\partial \tau}\right)d\mathbf{y}\right]_{\tau=t_0}\end{aligned} \tag{4.11}$$

If we use a free space or a tailored Green's function the second integral is zero, since (4.10) applies. The third integral is nil if we take $t_0 = -\infty$.

In spectral space

We can follow the same procedure to retrieve a solution in spectral space. The wave operator in the spectral domain is the Helmholtz operator

$$\left(\frac{\partial^2}{\partial x_i^2} + k^2\right)$$

Where $k = \omega/c_\infty$ is the acoustic wavenumber. The forced wave equation is

$$\left(\frac{\partial^2}{\partial x_i^2} + k^2\right)\widehat{\psi}(\mathbf{x},\omega) = \widehat{Q}(\mathbf{x},\omega)$$

As we saw above, the Green function satisfies

$$\left(\frac{\partial^2}{\partial x_i^2} + k^2\right)\widehat{G}(\mathbf{x}|\mathbf{y},\omega) = \delta(\mathbf{x}-\mathbf{y})$$

and the solution for ψ in the absence of boundaries (free space) is

$$\widehat{\psi}(\mathbf{x},\omega) = \iiint_V \widehat{Q}(\mathbf{y},\omega)\widehat{G}(\mathbf{x}|\mathbf{y},\omega)d\mathbf{y}$$

Where the overscript $\widehat{\ }$ indicates that the quantity is expressed in Fourier space.

Solution of the Lighthill equation

The solution of (4.6) is found by convolution with a suitable Green's function. The problem can be treated as linear since we have assumed that the variations in pressure in the listener's domain are small. This is a fair assumption even when very high noise levels are concerned as in the case of turbo jets (Colonius and Lele, 2004). This assumption ceases to be valid for instance in the case of sonic booms; these cases however are out of the scope of this thesis. The Green's function for the wave equation in free space is

$$G = \frac{1}{4\pi r}\delta(g) \qquad \text{with} \qquad g = t - \tau - \frac{r}{c_\infty}$$

$t - r/c_\infty$ is the retarded time, i.e. the expression of the delay between the time t at which a density fluctuation is recorded at the listener point and the time at which it has been produced, at a distance r. The solution is obtained by performing the convolution

$$p' = -G \star \frac{\partial^2 T_{ij}}{\partial x_i \partial x_j} = -\frac{1}{4\pi}\iiint_V \int_{-\infty}^{\infty} \frac{1}{r}\delta(g)\,\frac{\partial^2 T_{ij}}{\partial y_i \partial y_j}(\mathbf{y},\tau)\,d\tau d\mathbf{y} \tag{4.12}$$

That gives

$$p'(\mathbf{x},t) = \frac{1}{4\pi}\iiint_V \frac{1}{r}\frac{\partial^2 T_{ij}}{\partial y_i \partial y_j}\left(\mathbf{y}, t - \frac{r}{c_\infty}\right) d\mathbf{y} \tag{4.13}$$

Thanks to the proprieties of convolution the derivatives can be moved outside the integral, or onto the Green's function. We can therefore obtain several formulations of the analogy which, although formally equivalent, can pose radically different problems when solved numerically.

Time formulation

By applying the transformation

$$\frac{\partial}{\partial x_i}\left(\frac{\delta(g)}{r}\right) = -\frac{1}{c_\infty}\frac{\partial}{\partial t}\left(\frac{r_i \delta(g)}{r^2}\right) - \frac{r_i \delta(g)}{r^3}$$

we can write the Lighthill analogy in time formulation, in this case with the derivatives with respect to the source

$$p'(\mathbf{x},t) = \frac{1}{4\pi}\iiint_V \left[\left(\frac{r_i r_j}{r^3}\frac{1}{c_\infty}\frac{\partial^2 T_{ij}}{\partial \tau^2}\right) + \left(\frac{3r_i r_j}{r^4} - \frac{\delta_{ij}}{r^2}\right)\frac{1}{c_\infty}\frac{\partial T_{ij}}{\partial \tau} + \left(\frac{3r_i r_j}{r^5} - \frac{\delta_{ij}}{r^3}\right) T_{ij}\right]\left(\mathbf{y}, t - \frac{r}{c_\infty}\right) d\mathbf{y} \tag{4.14}$$

Spectral formulation

We can write the Lighthill's equation (4.6) in frequency domain:

$$\left(\frac{\partial^2}{\partial x_i^2} + k^2\right)\widehat{p}'(\mathbf{x},\omega) = -\frac{\partial^2 \widehat{T}_{ij}}{\partial x_i \partial x_j} \tag{4.15}$$

where $k = \omega/c_\infty$ is the wavenumber. The Green's function in free space is

$$\widehat{G} = -\frac{e^{-ikr}}{4\pi r}$$

The solution, with the derivatives moved on the Green's function is

$$\begin{aligned}\widehat{p}'(\mathbf{x},\omega) &= \frac{1}{4\pi}\iiint_V \frac{\partial^2 \widehat{G}}{\partial y_i \partial y_j}\widehat{T}_{ij}(\mathbf{x},\omega) d\mathbf{y} \\ &= \frac{1}{4\pi}\iiint_V \left[k^2 \frac{r_i r_j}{r^3} + ik\left(\frac{3r_i r_j}{r^4} - \frac{\delta_{ij}}{r^2}\right) + \left(\frac{3r_i r_j}{r^5} - \frac{\delta_{ij}}{r^3}\right)\right] e^{-ikr}\widehat{T}_{ij}(\mathbf{y},\omega)\, d\mathbf{y}\end{aligned} \tag{4.16}$$

for a 3D case, or

$$\widehat{p}'(\mathbf{x},\omega) = \frac{i}{4\pi}\iint_S \left[k^2\frac{r_i r_j}{r^2}H_0^{(2)}(kr) - k\left(\frac{2r_i r_j}{r^3} - \frac{\delta_{ij}}{r}\right)H_1^{(2)}(kr)\right]\widehat{T}_{ij}\left(\mathbf{y},\omega\right)d\mathbf{y} \tag{4.17}$$

in a 2D case. $H_i^{(2)}$ is the Hankel function of the second kind of order i.

Acoustic analogy formulation for a puff in square duct flow

Curle's formulation and the exact Green's function

Curle (1955) extended the Lighthill analogy to account for compact and stationary surfaces in the volume, the case of moving surfaces was later included in the formulation by Ffowcs Williams and Hawkings (1969) (hereafter FWH). The quadrupolar volume sources radiation is computed with the free space Green's function, with the addition of a dipolar contribution representing the noise radiated at the surfaces. Schram (2009); Martínez-Lera et al. (2014) showed that in the case of non compact sources the wall dipoles radiate based on both the hydrodynamic and the acoustic components of pressure at the wall. Hence the sources computed with an incompressible solver are not well suited for Curle's analogy. We start from the general formulation by FWH to derive a new formulation in which both the quadrupolar and the dipolar radiations are computed with the tailored Green's function, hence allowing the use of the incompressible noise sources. The original equation is

$$\widehat{p}(\mathbf{x},\omega) = -\iiint_V \frac{\partial^2\widehat{G}}{\partial y_i \partial y_j}\widehat{T}_{ij}d\mathbf{y} - \iint_\Sigma \frac{\partial\widehat{G}}{\partial y_i}\widehat{F}_i\delta(f)d\Sigma - \iint_\Sigma i\omega\widehat{Q}\widehat{G}\delta(f)d\Sigma \tag{4.18}$$

it contains the Fourier transformed quadrupolar component T_{ij}, and the dipolar and monopolar components

$$F_i = -[\rho u_i(u_j - u_j^\Sigma) + p\delta_{ij} - \tau_{ij}]n_j$$

and

$$Q = [\rho(u_j - u_j^\Sigma) + \rho_\infty u_j^\Sigma]n_j$$

The monopolar term Q is zero, since the walls are stationary ($u_j^\Sigma = 0$) and because of the no-slip condition $u_j = 0$ at the wall. For the same reasons the first part of the dipolar term disappears, leaving only the pressure and viscous terms. We consider now the dipolar contribution on the walls with normal 1, the same applies for the wall normal 2, whereas no walls are present with wall normal

3 (see figure 4.1 for a sketch of the computational domain).

$$\frac{\partial G}{\partial y_1}F_1 + \frac{\partial G}{\partial y_2}F_2 + \frac{\partial G}{\partial y_3}F_3 = \frac{\partial G}{\partial y_1}(p\delta_{11} - \tau_{11})n_1 + \frac{\partial G}{\partial y_2}(p\underbrace{\delta_{12}}_{0} - \tau_{12})n_1 + \frac{\partial G}{\partial y_3}(p\underbrace{\delta_{13}}_{0} - \tau_{13})n_1 \tag{4.19}$$

No hypotheses have been made so far on the nature of the Green's function. Curle's and FWH analogies allow the use the free space Green's function to compute the noise in the presence of walls. This is a very powerful property since it allows the use of the analogy on any geometry without the need of a tailored (exact) Green's function, by computing explicitly the two additional terms in equation (4.18). We will assume here that G is the tailored Green function, defined with the boundary condition $\partial G/\partial n = 0$. Eliminating the nil terms and applying the boundary condition for G, equation (4.19) becomes

$$\frac{\partial G}{\partial y_1}F_1 + \frac{\partial G}{\partial y_2}F_2 + \frac{\partial G}{\partial y_3}F_3 = -\left[\frac{\partial G}{\partial y_2}\tau_{12} + \frac{\partial G}{\partial y_3}\tau_{13}\right]n_1$$

The normal viscous term vanishes, in accordance with Powell (1960). Moreover, in the specific case of the infinitely long square duct, no surface with a normal parallel to the streamwise direction 3 is present. The full dipolar contribution is given by the walls with normal n_1 and n_2 (no walls are present with normal n_3). The far field pressure is given by

$$\widehat{p}(\mathbf{x},\omega) = -\iiint_V \frac{\partial^2 \widehat{G}}{\partial y_i \partial y_j}\widehat{T}_{ij}d\mathbf{y} - \iint_\Sigma \left[\left(\frac{\partial \widehat{G}}{\partial y_j}\widehat{\tau}_{ij}\delta(f)\right)n_i d\Sigma\right]_{i=1,2;j\neq i} \tag{4.20}$$

This formulation computes the radiation of both the quadrupolar and dipolar contributions by the tailored Green's function, it can be used to compute the noise generated by an incompressible source without the need of adding the acoustic contribution on the wall dipoles. This solution is of course viable only if the tailored Green's function is available, but is much simpler than the methodology by Schram (2009), who used a boundary element method to compute the acoustic pressure at the wall starting from an incompressible field, and then used a modified version of Curle's analogy to compute the radiated noise using the free space Green's function.

Green's function in a duct of square cross section

Davies and Ffowcs Williams (1968) gave the Green's function for an infinitely long duct of square cross section, which is compatible with the present definition of the wave operator (4.6) when solving for pressure.

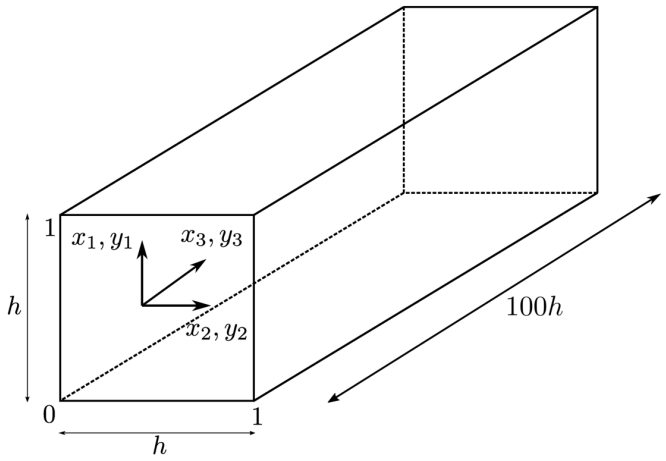

Figure 4.1: Sketch of the computational domain, the duct has a square cross section of side $h = 1$. The length is $100h$. The streamwise coordinates are indicated by the subscript 3, the wall normal directions are $1, 2$. x, y indicate the coordinates for the listener and source, respectively

$$G(\mathbf{x}, \omega) = -\frac{i}{2} \sum_{m,n=0}^{\infty} C_{mn}(x_1, x_2) \cos\left(\frac{m\pi y_1}{h}\right) \cos\left(\frac{n\pi y_2}{h}\right) \frac{\exp\left(ik_{mn}\left|x_3 - y_3\right|\right)}{k_{mn}} \tag{4.21}$$

with

$$\begin{aligned} C_{mn}(x_1, x_2) &= \frac{1}{h^2 \varepsilon_n \varepsilon_m} \cos\left(\frac{m\pi x_1}{h}\right) \cos\left(\frac{n\pi x_2}{h}\right) \\ \varepsilon_n &= 1 \qquad \text{if } \; n = 0 \\ \varepsilon_n &= \frac{1}{2} \qquad \text{if } \; n > 0 \\ k_{mn}^2 &= \frac{\omega^2}{c_\infty^2} - \left(m^2 + n^2\right) \frac{\pi^2}{h^2} \end{aligned} \tag{4.22}$$

The subscripts $1, 2$ indicate the cross-stream directions, 3 is the streamwise direction. m, n are the cross-stream wavenumbers, $m = 0$ indicates the plane mode in the direction 1. If both m, n are zero we have a plane wave. k_{mn} is the streamwise propagation wavenumber of the m, n cross-stream mode; it determines whether a mode is propagated or exponentially attenuated. If ω/c_∞ is large and m, n are small, then k_{mn} is real, hence the exponential term in (4.21) is complex and the mode propagates. For high cross stream wavenumbers we have that k_{mn} is imaginary, the exponent becomes real and negative. The mode is exponentially dissipated with distance. Such modes are said evanescent. As a consequence the high frequency cross-stream modes are more likely to be cut off at low streamwise wavenumbers. As the streamwise wavenumber increases, more and more cross stream modes are cut

in. The only mode that is always propagated is the plane wave mode, since $m = n = 0$. All the other modes, if propagated, are dispersive (Pierce (1989)), i.e. their signature is increasingly distorted with distance, or in other words the wavepacket with pulsation ω is more and more spread in space with increasing distance. This is due to the fact that a streamwise mode is composed by a sum of cross-stream modes with different wavenumbers and therefore different phase velocities ω/k_{mn}, with

$$\omega = \frac{2\pi n_s}{N\Delta t} \tag{4.23}$$

In order to compute the non dimensional sound speed at infinity c_∞ we use the definition of Ma

$$Ma = \frac{U_b}{c^*_\infty}$$

with c^*_∞ indicating the dimensional sound speed at infinity, we retrieve the non dimensional sound speed

$$c_\infty = \frac{c^*_\infty}{U_b} = \frac{1}{Ma}$$

The wavenumber is

$$k = \frac{\omega}{c_\infty}$$

Figure 4.2 shows the number of propagating cross-stream modes against the non dimensional frequency $f = \omega/2\pi$, for unitary bulk velocity and section side length, $Ma = 0.3$. For low streamwise wavenumbers only few cross-stream modes are cut in; when the streamwise mode is larger we have more propagating cross-stream modes. This analysis is also a tool for choosing the correct number of cross-stream modes to compute.

Explicit form of the Green's function derivatives

Equation (4.21) expresses the components of the Green's function for an infinite duct of square cross section. In order to compute the far field pressure fluctuations we will differentiate the Green's function as we did in (4.16). Such compact form for the 6 components is not easy to retrieve in the square duct case, for clarity we report them explicitly. k_{mn} and C_{mn} are calculated as in (4.22), the

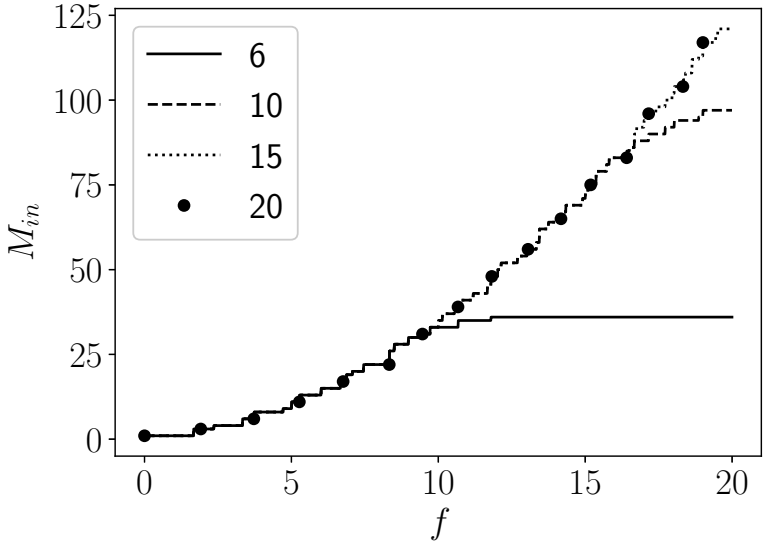

Figure 4.2: Example of dependence of the number of propagating (M_{in}) modes on frequency. Different lines correspond to different numbers of cross-stream modes. $h = 1$, $Ma = 0.3$, $U_b = 1$, $c_\infty = 3.33$

explicit dependency of C_{mn} on x_1, x_2 is dropped for brevity.

$$
\begin{aligned}
\frac{\partial^2 G}{\partial y_1 \partial y_1} &= +\frac{i}{2}\sum_{m,n=0}^{\infty} C_{mn}\left(\frac{m\pi}{h}\right)^2 \cos\left(\frac{m\pi y_1}{h}\right)\cos\left(\frac{n\pi y_2}{h}\right)\frac{\exp\left(ik_{mn}\left|x_3-y_3\right|\right)}{k_{mn}} \\
\frac{\partial^2 G}{\partial y_2 \partial y_2} &= +\frac{i}{2}\sum_{m,n=0}^{\infty} C_{mn}\left(\frac{n\pi}{h}\right)^2 \cos\left(\frac{m\pi y_1}{h}\right)\cos\left(\frac{n\pi y_2}{h}\right)\frac{\exp\left(ik_{mn}\left|x_3-y_3\right|\right)}{k_{mn}} \\
\frac{\partial^2 G}{\partial y_3 \partial y_3} &= +\frac{i}{2}\sum_{m,n=0}^{\infty} C_{mn}\cos\left(\frac{m\pi y_1}{h}\right)\cos\left(\frac{n\pi y_2}{h}\right)k_{mn}\exp\left(ik_{mn}\left|x_3-y_3\right|\right) \\
\frac{\partial^2 G}{\partial y_1 \partial y_2} &= -\frac{i}{2}\sum_{m,n=0}^{\infty} C_{mn}\left(\frac{nm\pi^2}{h^2}\right)\sin\left(\frac{m\pi y_1}{h}\right)\sin\left(\frac{n\pi y_2}{h}\right)\frac{\exp\left(ik_{mn}\left|x_3-y_3\right|\right)}{k_{mn}} \\
\frac{\partial^2 G}{\partial y_1 \partial y_3} &= -\frac{i}{2}\sum_{m,n=0}^{\infty} C_{mn}\left(\frac{m\pi}{h}\right)\sin\left(\frac{m\pi y_1}{h}\right)\cos\left(\frac{n\pi y_2}{h}\right)\frac{i\exp\left(ik_{mn}\left|x_3-y_3\right|\right)}{sign(x_3-y_3)} \\
\frac{\partial^2 G}{\partial y_2 \partial y_3} &= -\frac{i}{2}\sum_{m,n=0}^{\infty} C_{mn}\left(\frac{n\pi}{h}\right)\cos\left(\frac{m\pi y_1}{h}\right)\sin\left(\frac{n\pi y_2}{h}\right)\frac{i\exp\left(ik_{mn}\left|x_3-y_3\right|\right)}{\mathrm{sign}(x_3-y_3)}
\end{aligned}
\tag{4.24}
$$

The term $sign(x_3-y_3)$ has been written in the denominator for compactness. In calculating $\partial^2 G/\partial x_3 \partial x_3$ we have neglected the derivative of the sign function, which is zero everywhere, except for a singularity when $x_3 = y_3$, which never happens in the case of concern since we only compute the noise far from the non linear zone. Moreover, even in the cases where one computes the sound produced inside the

source zone the source points in the close vicinity of the listener point are neglected (Watrigant, 2010; Croaker et al., 2013). Therefore this assumption is always justified in aeroacoustics applications.

Database generation

We simulate the flow using the incompressible DNS solver described in chapter 2. The non dimensional duct side length h is unitary, the length of the duct is $L = 100h$. The computational grid is composed of 51 points in the two cross-stream directions and 1024 points in the streamwise direction and the non dimensional time step is $2 \cdot 10^{-3}$. A sketch of the computational domain is given in figure 4.1. The computational mesh is uniform in the stream-wise direction. In the inhomogeneous cross flow directions the grid spacing is given by the Chebyshev nodes, the grid is refined close to the wall. This produces very low error during the turbulent field computation Trefethen (2000), but is not convenient for the noise computation due to the large spacing, especially at the center of the domain. Therefore each snapshot is interpolated in the two cross-stream directions on a uniform grid of 70 points per side. We use a spectral interpolation method, consistent with the spatial discretization, therefore no additional numerical error is introduced during the interpolation and the spectral accuracy is conserved.

Turbulent puffs move downstream with a speed very close to the flow bulk velocity U_b (Song et al., 2017). The DNS is performed using a frame of reference moving with U_b, therefore the turbulent puff remains stationary, and specifically at the center of the computational domain throughout the whole calculation. Another method would consist in computing the DNS on a stationary reference frame, and recenter the snapshots before computing the acoustic pressure. This method however would artificially annihilate the natural velocity fluctuations of the puff and most likely give rise to some artificial frequency in the noise spectrum.

A turbulent puff is characterised by a steep upstream front; this is where the turbulence production mainly takes place, the turbulence generated is then slowly dissipated along the downstream front, which is much less definite. Thanks to the moving reference frame the puffs remain quasi stationary at this position in the streamwise coordinate. The database consists of 5000 snapshots saved every 20 iterations, i.e. separated by a time interval $\Delta t = 4 \cdot 10^{-2}$ non dimensional time units. In all the snapshots the puff is positioned at about the center of the domain, at $x \sim 0$. The time discretisation

parameters are thus

$$T = Ndt = 200 \qquad f_{Ny} = 12.5 \qquad \Delta f = 5 \cdot 10^{-3} \tag{4.25}$$

where T indicates the total non dimensional time, f_{Ny} the Nyquist frequency and Δf the frequency resolution.

Each file is then reprocessed to create one file for each point in the 2 wall normal directions, this results in generating $70 \times 70 = 4900$ files for each component of velocity, hence 14700 files. Each of these files is a $2d$ matrix representing the time evolution of all the points with constant y_1, y_2 coordinates. Although not practical from a file-managing point of view, this method makes the code parallelisation straightforward. The program is written in Fortran 90 and parallelised by MPI on 4900 processes. Each process computes the noise contribution of the points with a given y_2, y_3.

Numerical details

Analogy in Fourier space

The Lighthill's tensors are fourier transformed in time by *fft*, since time periodicity is not verified we apply a Tukey window with a tapering factor of 0.1. The effect of windowing are discussed in section 4.5.7. The only MPI communication is performed at the end of the execution to generate a single output file.

Analogy in time

An additional difficulty is added in this case due to the necessity of computing the time derivatives at retarded time. Moreover the initial time must be carefully chosen to maximise the number of snapshots that are included within the minimum and the maximum retarded times, this depends on the position of the listener, and thus changes for every probe. The components of the inviscid Lighthill tensor and their time derivative are computed at retarded time using a 4^{th} order Lagrange interpolation difference scheme and a 5 points stencil, using the same sources used for the analogy in Fourier space. The far field formulation obtained by neglecting the terms of $\mathcal{O}(1/r^2)$ and $\mathcal{O}(1/r^3)$ in equation (4.14) provides the same result.

Comparison between the time and frequency formulations

The solution is computed solving Lighthill's equations in frequency (4.16) and time formulation (4.14), imposing $Ma = 0.3$. Figure 4.3 shows the pressure spectra computed for an observer point positioned upstream with respect to the puff in the moving frame, at $x_3 = -100$, $x_{1,2} = 0.5$ by means of the frequency and time formulations. The spectra show a maximum at about $f = 2.5$, at lower pulsations it is approximately constant, and has a rapid, exponential decrease for $f > 3$. Both the calculations were performed on a shorter database of $N = 3000$ snapshots, hence the slight differences with respect to the results that follow, especially at low frequency. The two formulations bear rather radical differences in their implementation, and give nonetheless a very similar result (see also the comparison of the pressure time histories in figure 4.4), except at low frequencies due to the uncertain statistical convergence. This gives us a good deal of confidence regarding the validity of the results. All the calculations will henceforth be performed using the analogy in frequency formulation.

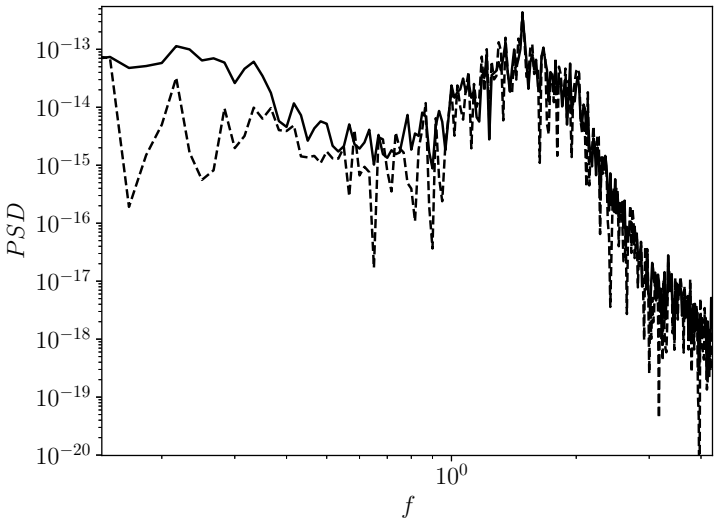

Figure 4.3: Pressure spectrum of the acoustic field generated by a turbulent puff in free space, at $x_3 = -100$, $x_{1,2} = 0.5$, computed using the frequency formulation (continuous line) and the time formulation (dashed line), using a shorter database of 3000 snapshots and $Ma = 0.3$

The influence of time windowing

The Fourier transform is defined for periodic signals, however such hypothesis is very often not verified, especially when turbulence is involved. It is common practice to multiply the signal by a

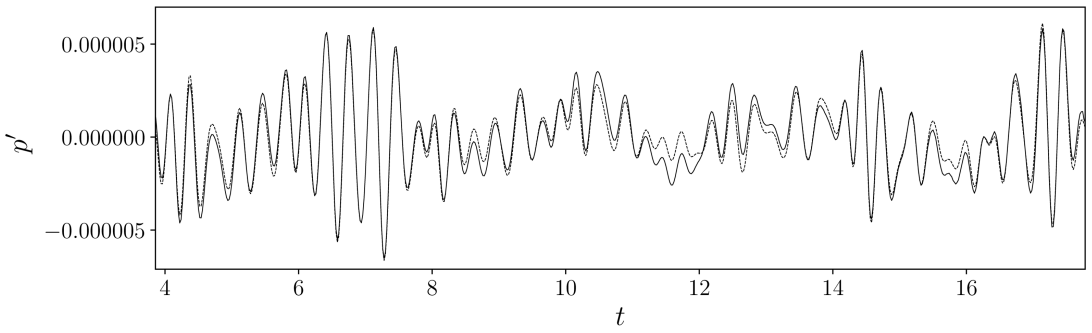

Figure 4.4: Comparison of the pressure fluctuation time signals computed with the frequency formulation (dashed line) and with the time formulation (continuous line) in free space, using a shorter database of 3000 snapshots and $Ma = 0.3$. Listener at $x_3 = -100$, $x_{1,2} = 0.5$

function whose value is zero at the ends of the domain to make a non periodic signal a periodic one. For a review on the use of windowing in signal processing see Harris (1978). Figure 4.5 shows the time signals of the noise generated by a puff in free space at $Ma = 0.3$, measured at $x_3 = -100$, $x_{1,2} = 0.5$, computed by means of the Lighthill analogy in frequency formulation without windowing, with the Tukey window and the values 0.1 and 0.5 of the shape parameter, and with the Hann window (or, equivalently, with the Tukey window and shape parameter 1). When no windowing is applied the signal presents strong disturbances localised at t close to 45. The effects of the other windows are located in the same zone. The Hann window strongly tapers the signal over a wide range of times while the effect of the Tukey window is much more contained, especially when the parameter is 0.1. Elsewhere the signals are equivalent to each other, testifying the consistency of the results with different windowings, where strong numerical effects are not observed. $t \sim 45$ corresponds to a mean retarded time. To draw the spectra we recenter the noise time signal by shifting it by the retarded time computed with respect to the centroid of the puff, which we locate at $x_3 = 50$. The shifted time signal is reported in figure 4.6. When defining the PSD we again apply a windowing, which successfully erases the numerical errors that are now relegated to the ends of the signal.

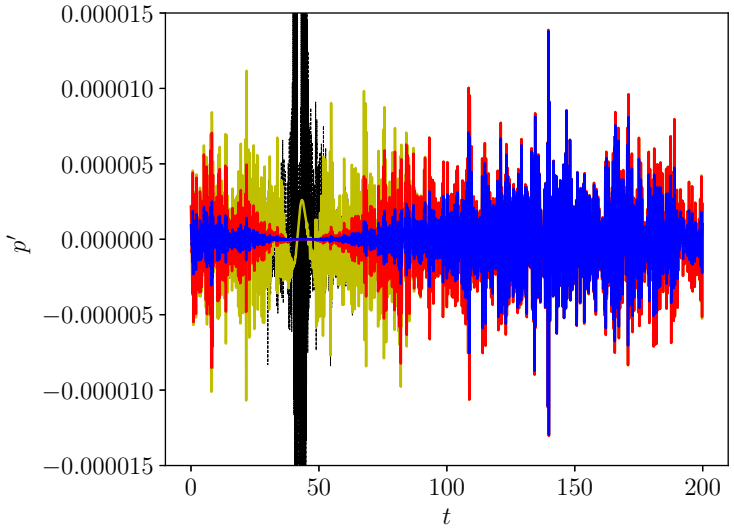

Figure 4.5: Influence of the time windowing. Time signals of the noise generated by a turbulent puff in free space, black: no windowing, yellow: Tukey window (shape parameter 0.1), red: Tukey window (shape parameter 0.5), blue: Hann window. Listener at $x_3 = -100$, $x_{1,2} = 0.5$

Analysis of the sources

A-priori: visual analysis

Figure 4.7 shows the contour plots of the double divergence of the Lighthill tensors

$$\frac{\partial^2 T_{ij}}{\partial x_i \partial x_j}$$

at the x_1 mid-plane. This quantity is the right hand side of the Lighthill's equation (4.6) and is directly related to the sound sources. These are contours of one instantaneous snapshot. Contour plots of x_1 and x_2 vorticity of the same snapshot at the same location are reported in figures 4.8 and 4.9 for comparison with the sound sources. We see near the top left corner of figure 4.8 a Helmholtz-like structure, with at least two vortices, that are transported downstream and lifted towards the centre of the duct, ending up in the core of the puff. An even clearer signature is observed in figure 4.9, the yellow dots corresponding to the center of the first two vortices. We can identify 4 vortices, the last being almost at the center of the puff. Two smaller, but similar signatures are observed more downstream above the lower wall. These structures however are not always visible (for instance, if we consider a slice orthogonal to the one we considered so far, we no longer observe the Kelvin Helmholtz

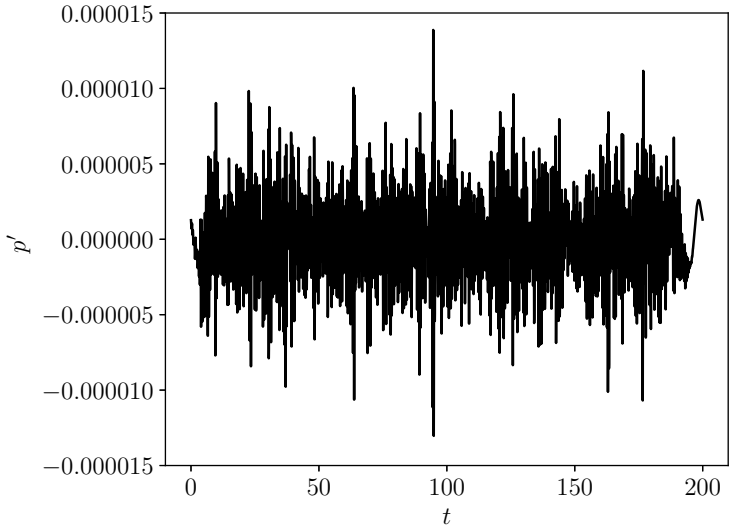

Figure 4.6: Recentered time signal of the noise generated by a turbulent puff in free space, shifted by the retarded time of the puff centroid. Listener at $x_3 = -100$, $x_{1,2} = 0.5$

vortices). In other snapshots the situation is similar, the vortices are often present in one of the sections, but their number and intensity vary.

Focusing now on the sound sources, we see that the highest peaks correspond to T_{11} and T_{22}, that radiate in the two cross-stream directions. Another important source is found at the same locations for T_{12}. We must notice that the colors are saturated to allow a clearer understanding, the maximal and minimal values in T_{11} and T_{22} are 2-3 times larger (in absolute value) than those of T_{33}. Thus the largest sound sources seem to be determined for the most part by the cross-stream components of velocity. T_{33} sources are localised at the puff core, but remain smaller compared to the cross-stream sources. The higher values of the double divergence of T_{11}, T_{22} seem related to the center of some of the vortices, namely the first (at $x_3 \sim 27$) and the third ($x_3 \sim 29$).

A-posteriori: the noise produced by a puff in free space

We first compute the acoustic pressure in the absence of walls. This calculation, although not completely sound from a physical point of view can give us some insights about the shape of the spectrum, the frequencies involved and the relative importance of the noise components.

The solutions were also computed with the listener placed laterally with respect to the puff, at

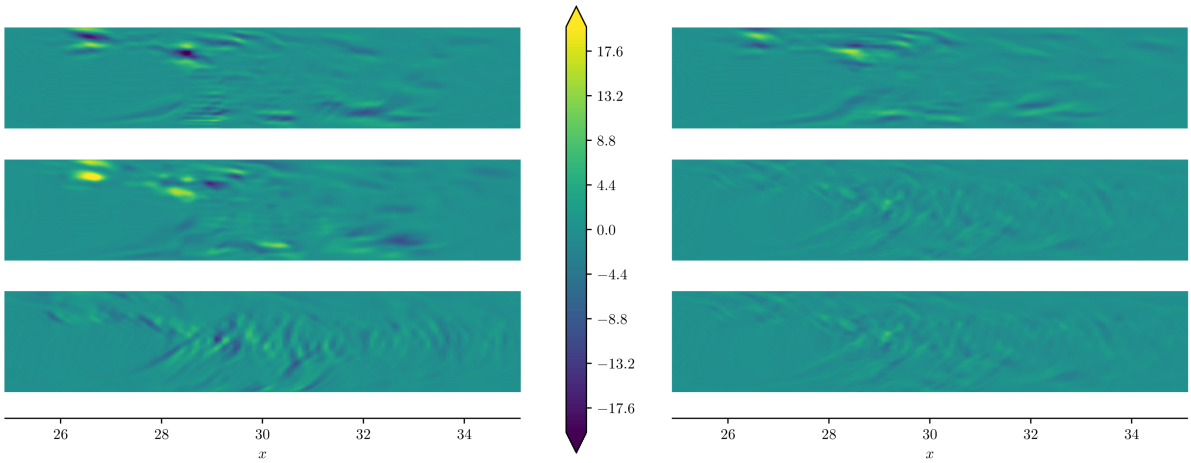

Figure 4.7: Contours of the double divergence of the Lighthill tensors computed at the x_1 mid-plane for one snapshot. Left column, from top to bottom: $\partial^2 T_{11}/\partial x_1^2, \partial^2 T_{22}/\partial x_2^2, \partial^2 T_{33}/\partial x_3^2$, right column, from top to bottom: $\partial^2 T_{12}/\partial x_1 \partial x_2, \partial^2 T_{13}/\partial x_1 \partial x_3, \partial^2 T_{23}/\partial x_2 \partial x_3$

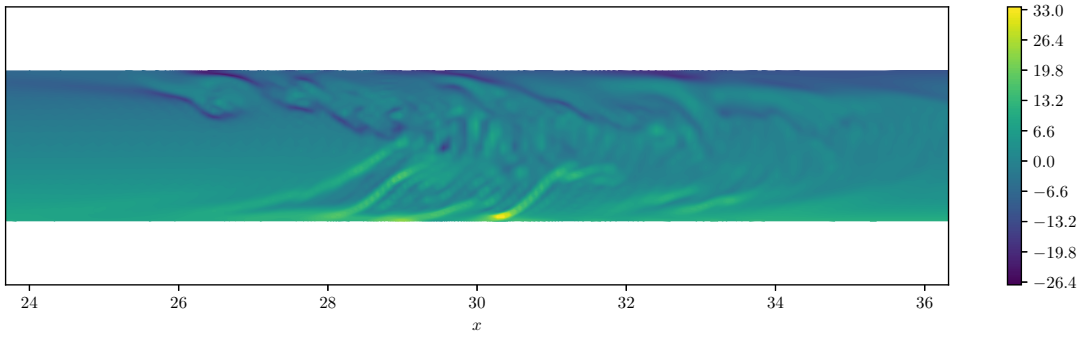

Figure 4.8: Contour plot of the x_1 component of vorticity at the x_1 mid-plane of a snapshot

$x_1 = 100$, $x_2 = 0.5$, $x_3 = 50$. The noise spectra are superposed with those in figure 4.10 and are not shown for clarity. The individual components of the noise spectrum however do present some major differences. Figure 4.11 shows the pressure fluctuation spectra of the 6 components taken separately, computed with the frequency formulation of the Lighthill's equation (4.16) for the listener positions $x_3 = -100, x_{1,2} = 0.5$ (upstream of the puff, continuous line) and $x_1 = 100, x_2 = 0.5, x_3 = 50$ (laterally from the puff, dashed line), outside of the duct walls, no noise would be radiated here in a real case. When the listener is upstream of the puff the streamwise component T_{33} dominates on the others by at least an order of magnitude. The spectrum of T_{33} is very similar to the full spectrum of figure 4.11. We notice that T_{11} and T_{22} are equivalent, as well as $T_{23} = T_{13}$, coherently with what we should

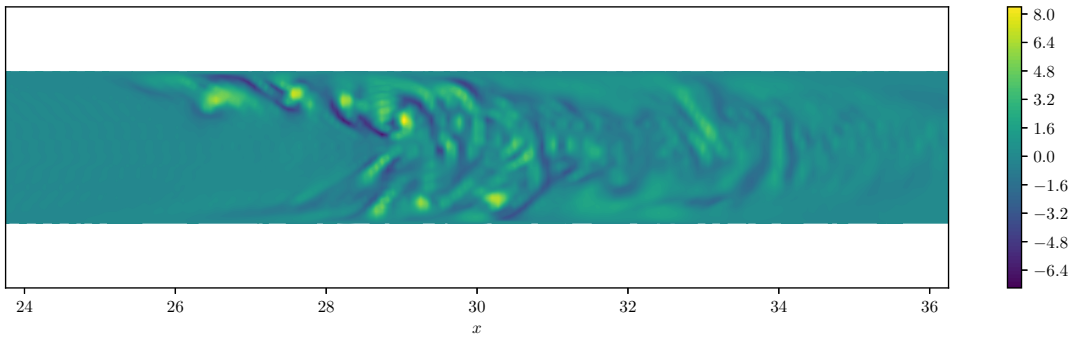

Figure 4.9: Contour plot of the x_2 component of vorticity at the x_1 mid-plane of a snapshot

expect due to symmetry. For a listener placed laterally the situation is similar, but the dominant component is T_{11}. In this case however an important contribution is given by the lateral quadrupole T_{12}, which is negligible for a listener placed upstream. The fact that the spectrum for T_{11} for the lateral listener is superposed to the spectrum of T_{33} when the listener is upstream is in contrast with the discussion in section 4.6.1, and probably indicates that the noise sources corresponding to the Kelvin Helmholtz vortices are localised events both in time and space that do not have a major influence on the noise spectrum. The stream-wise longitudinal quadrupole T_{33} is also rather important, even when the listener is not aligned with its direction. Again, this source does not appear to be among the most relevant in the sources visualisation in figure 4.6.1, but gives nonetheless an important contribution.

The noise generated by a puff in a duct of square cross section

We now compute the acoustic pressure by means of the acoustic analogy using the exact Green's function for an infinitely long square duct. We use the same routine used for the free space case and we substitute the Green's function with the tailored Green's function in equation (4.21). The number of cross stream modes is set to 7. This shall be sufficient since the range of frequencies of interest does not exceed $f = 6$ in the free space case at $Ma = 0.3$. Looking at figure 4.2 we notice that this number of cross stream modes is adequate and leaves a considerable margin. The analysis has been performed for $Ma = 0.3$ and 0.1, the considerations concerning the number of cross stream modes stand *a fortiori* for lower Mach numbers, since lower Ma implies a higher c_∞, thus a wall normal mode will need an even larger frequency not to be vanishing (see equation (4.22)). The present formulation implies two main hypotheses: the first is that the turbulent puff is stationary, or equivalently the listeners move

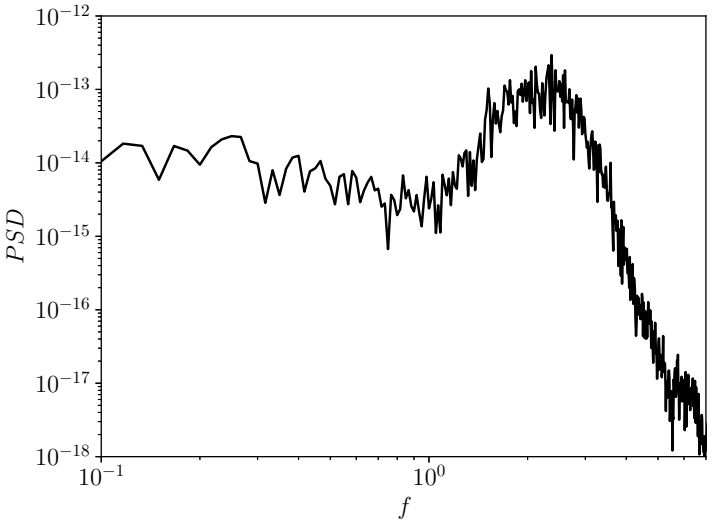

Figure 4.10: Pressure spectrum of the acoustic field generated by a turbulent puff in free space, at $x_3 = -100$, $x_{1,2} = 0.5$ and $Ma = 0.3$. Computed using the frequency formulation

with the bulk velocity. The second is that the Poiseuille velocity profile does not interact with the propagation of sound. This is probably the strongest hypothesis, and is less and less justified as Ma increases. For low Ma however we can assume that both the effects of convection and refraction are weak enough to allow the use of the present formulation (Crow, 1970).

$Ma = 0.3$

Figure 4.12 shows the pressure spectrum for a listener placed upstream at $x_3 = -150$ (left) and downstream at $x_3 = 150$ (right), computed on a grid of 16 points on the section and subsequently averaged to smoothen the result. The spectra are globally broadband, with higher noise levels for $f > 1.8$ and some clear peaks occurring at the same frequencies both upstream and downstream. The increase at this frequency is smoother for the downstream spectrum and more abrupt for the upstream one. Some other peaks are present, all of them have a very steep, vertical left side and a more gentle decrease on the right. Figure 4.13 explains the reason of this peculiar shape for the peaks. It shows the contributions of the singular components of the Lighthill tensor to the noise spectrum. T_{33} is the only component that is present throughout the whole spectrum, the others being cut-off for frequencies lower than a certain threshold. T_{11} and T_{22}, as well as T_{13} and T_{23} are equivalent, coherently with the symmetry of the problem. They contribute only for $f > 1.7$, with a very clear

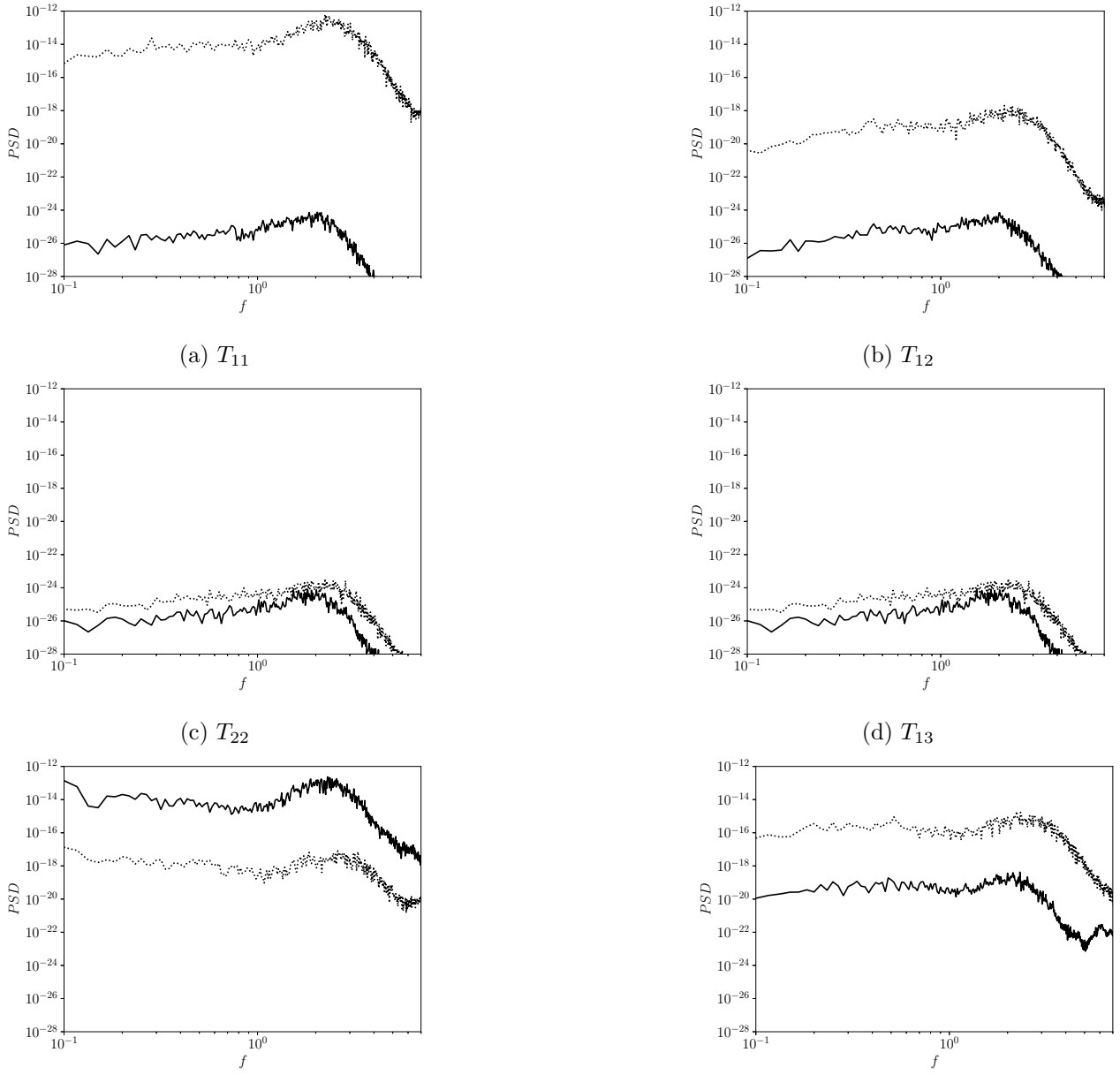

(a) T_{11} (b) T_{12}

(c) T_{22} (d) T_{13}

(e) T_{33} (f) T_{23}

Figure 4.11: Pressure fluctuations spectra for each component of the Lighthill tensor computed in a position upstream of the puff ($x_3 = -100$, $x_{1,2} = 0.5$, continuous line) and laterally from the puff, outside the duct ($x_1 = 100$,$x_2 = 0.5$, $x_3 = 0$). Turbulent puff in free space, noise computed using the frequency formulation and $Ma = 0.3$.

cut between the radiated and non radiated frequencies. In this range of frequencies the cross stream aligned longitudinal quadrupoles suddenly become dominant, hence the peak in figure 4.12. The other peak at $f \sim 2.7$ is due to T_{12}, this is the highest peak in the spectrum, that comes from the component

given by the mixed cross stream turbulent fluctuations. The differences observed between the upstream and downstream spectra in figure 4.12 are reproduced in the partial spectra. A downstream listener would observe the bump at $f \sim 2$, given by the streamwise longitudinal quadrupole T_{33}, the same bump is hardly seen by a listener placed upstream. The oscillations in the left part of the peaks are of numerical nature and only have an effect on the left side of the peaks, which is slightly made more gentle by the numerical oscillation. Such effect is totally eliminated when using a Hann window, as seen in figure 4.14. The physical part of the spectrum is perfectly consistent, the numerical oscillations are canceled, at the cost of a part of the time signal due to a stronger windowing. The vertical lines in the plots identify the cut-on frequencies relative to the modes with (m, n) couples (1,0),(1,1), (2,0), (2,1), (2,2) (or with inverted m, n, for symmetry). The location of the lines is determined by finding the frequency where k_{mn} becomes positive

$$k_{mn} = 0 = \frac{\omega^2}{c_\infty^2} = (m^2 + n^2)\left(\frac{\pi}{h}\right)^2$$

or

$$f = \frac{c_\infty}{2h}\sqrt{m^2 + n^2}$$

Figure 4.15 shows a contour of the imaginary part of the upstream sound field at $f = 0.32$ (a) and $f = 3.2$ (b). The low frequency noise is composed by planar waves, coherently with the fact that higher modes are cut-off at low frequencies, and are gradually cut-in when f increases. The longitudinal, cross stream aligned quadrupoles T_{11}, T_{22}, associated with wall normal momentum fluctuations, are suddenly propagated when the frequency threshold for the first possible cross stream mode $m = 1, n = 0$ is overcome. The same stands for the components T_{13}, T_{23}, associated with the wall normal vorticity. These contributions possibly produce semi-planar waves that can be propagated when $m = 1, n = 0$. The T_{12} component is cut-on with $(m, n) = (1, 1)$, it is associated to fluctuations of vorticity in the streamwise direction and do not produce semi-planar waves.

$Ma = 0.1$

Figure 4.16 shows the PSD of the sound generated by a turbulent puff at $Ma = 0.1$, measured by an upstream and a downstream listener (left and right plots, respectively). The difference with respect to the $Ma = 0.3$ case is clear. The upstream and downstream radiated noise differ much less, as compared to the higher Mach case. Moreover the spectrum is globally broadband and virtually no

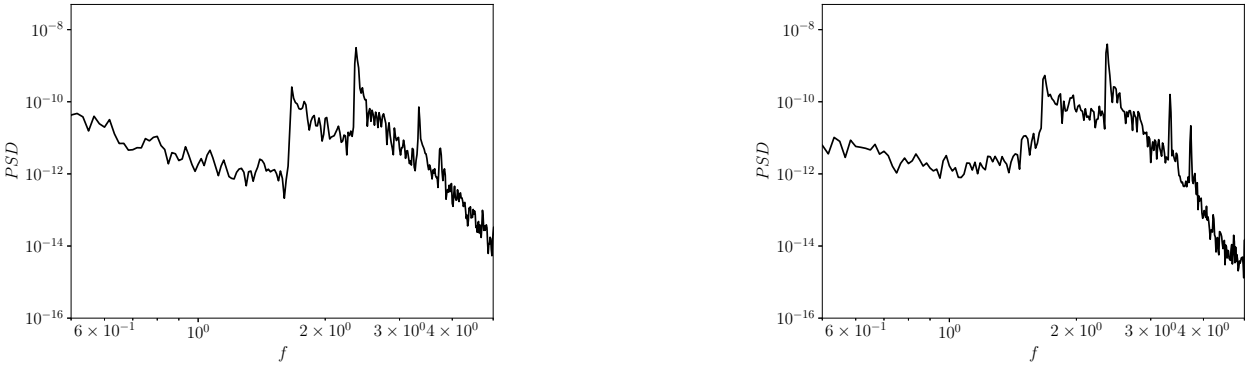

Figure 4.12: Pressure fluctuations PSD of the acoustic field generated by a turbulent puff at $Ma = 0.3$ in a duct of square cross section computed using the exact Green's function, listener placed upstream of the puff, at $x_3 = -150$ (left) and downstream, at $x_3 = 150$ (right)

major cut-on cut-off effects are noticeable in the full spectra, except for a small peak at $f \sim 5$ and an even smaller one at higher frequency. The analysis of the sound radiated by the single components of the Lighthill tensor in figure 4.17 confirms this picture. The T_{33} component is dominant along almost the whole frequency range, and the radiated noise is constituted by planar waves up to $f \sim 4.5$, where the wall normal components generate the peak observed in the full spectrum, but do not produce the major change in behaviour observed for $Ma = 0.3$. Hu et al. (2003) used a plane wave hypothesis in their computation of the sound radiation in a plane duct for Ma up to 0.1. This can be considered the limit for the plane wave hypothesis, at least in the square duct configuration, for higher Mach numbers the cross stream modes are propagated at lower frequencies and can become dominant.

Selected wavelength

For both the Mach numbers considered we do not observe the presence of a preferred frequency corresponding to a wavelength suitable for a long range communication. λ is defined as

$$\lambda = \frac{c}{f} = \frac{Ma}{U_b f}.$$

With the available database the longest wavelength that we can compute is around 30 at $Ma = 0.3$, which is close to the equilibrium length proposed by Samanta et al. (2011). The existence of an even longer equilibrium distance based on acoustic grounds cannot be excluded, however this is not what the shape of the spectrum at low frequencies suggests. Such analysis would require a longer database, or alternatively one generated with a larger time step.

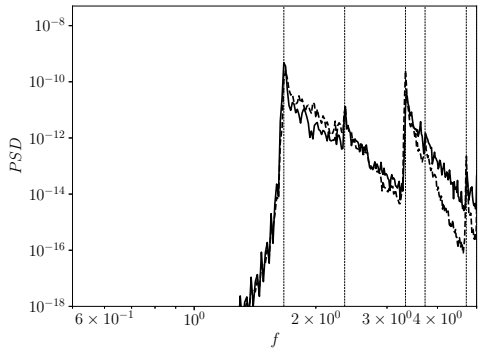

(a) T_{11}

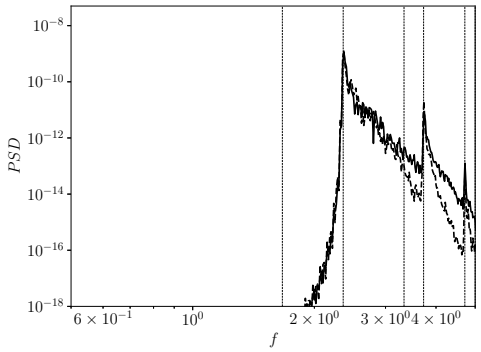

(b) T_{12}

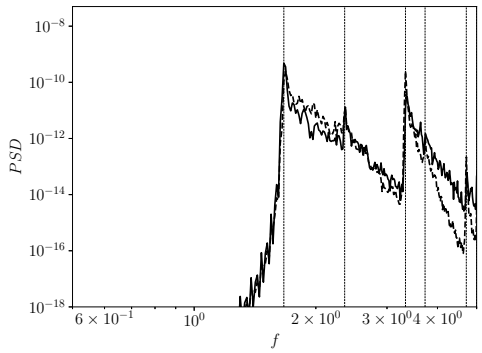

(c) T_{22}

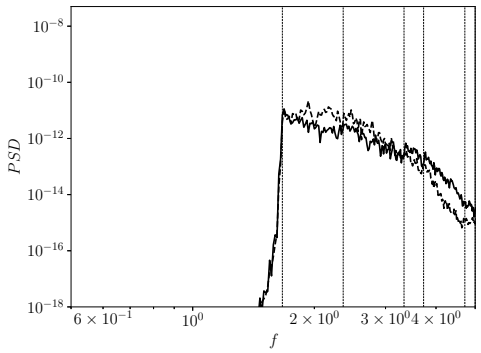

(d) T_{13}

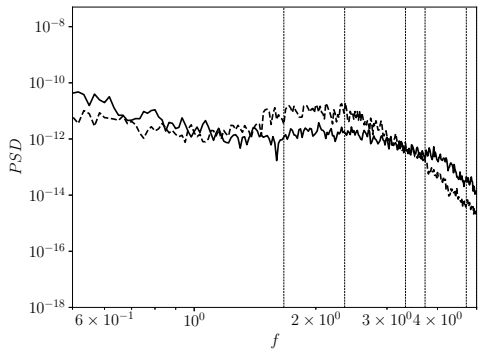

(e) T_{33}

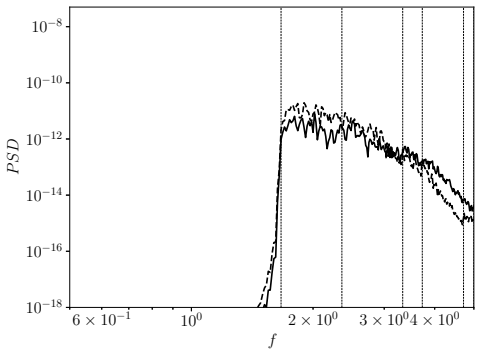

(f) T_{23}

Figure 4.13: Pressure fluctuations PSD spectra for each component of the Lighthill tensor computed at $x_3 = -150$ (continuous) and $x_3 = 150$ (dashed), $Ma = 0.3$. Turbulent puff in square duct, computed with the exact Green's function. The vertical lines indicate the cut-on frequencies for the (m, n) couples (1,0); (1,1); (2,0); (2,1); (2,2) in this order, from left to right

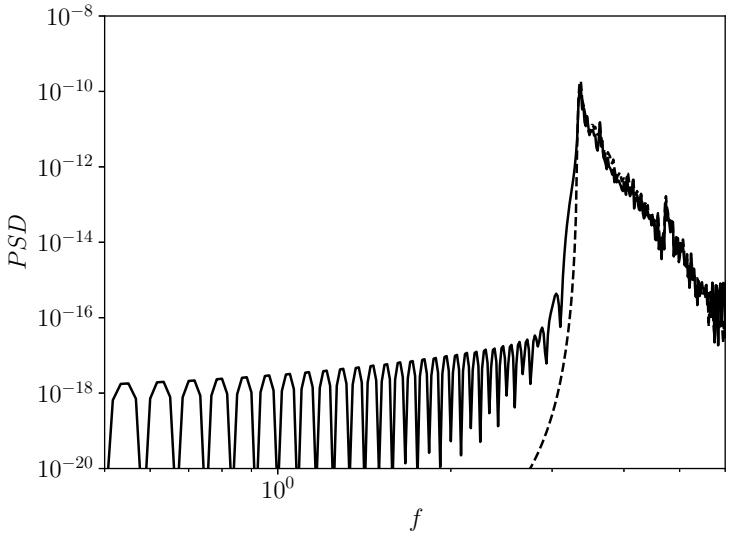

Figure 4.14: Influence of the windowing on the PSD spectrum of T_{11}. Continuous line: Tukey, dashed line: Hann.

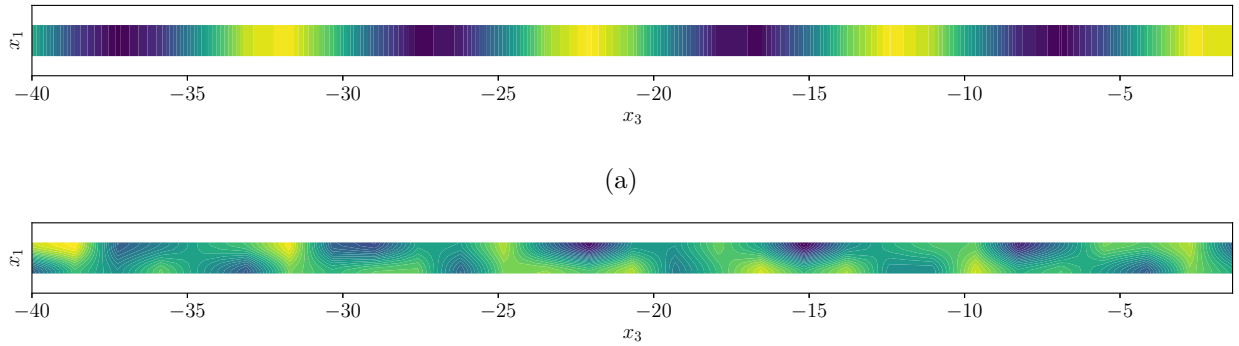

(a)

(b)

Figure 4.15: Imaginary part of the sound pressure field in frequency domain $Ma = 0.3$, (a): $f = 0.32$, (b): $f = 3.2$. The puff is not comprised in the domain, it is located on the right, outside the sheet, at $x_3 \sim 50$. The colormaps are not consistent for clarity.

Another form of acoustic interaction could be given by the high frequency peaks observed in figure 4.12. This scenario is interesting but not very likely. The acoustic radiation is very weak compared to turbulence, in order for a coupling to take place there should be an acoustic excitation of a specific, very sensitive, hydrodynamic mode. This could not be excluded *a priori*, since the planar streamwise waves are propagated at any frequency, thus a natural mode at a given frequency of a puff could be acoustically propagated and interact with the same mode of another puff, or we could have a

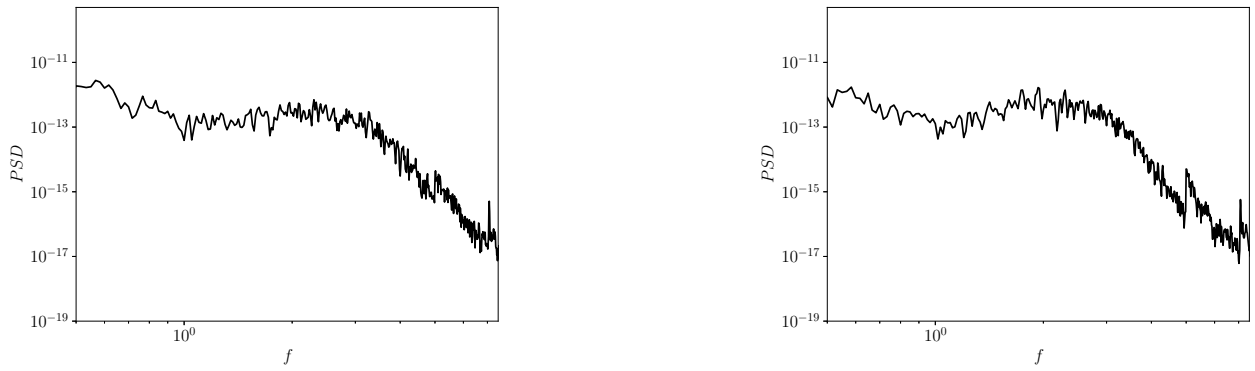

Figure 4.16: Pressure fluctuations PSD of the acoustic field generated by a turbulent puff at $Ma = 0.1$ in a duct of square cross section computed using the exact Green's function, listener placed upstream of the puff, at $x_3 = -150$ (left) and downstream, at $x_3 = 150$ (right)

synchronisation of the hydrodynamic and acoustic modes within a puff. The strong acoustic peaks in the figure on the other hand are highly dependent on the cut on-off mechanism, and are thus not inherent frequencies of the puff. Moreover the importance of these peaks depends on Ma, in a reasonable experiment the Mach number would be quite low, thus the peaks are most likely not present. The compressible simulation briefly discussed in appendix D does not exhibit any differences with respect to the incompressible one, suggesting that such phenomenon is indeed absent.

Noise intensity scaling

Figure 4.18 shows the acoustic intensity I scaling with Ma of the various contributions to the radiated noise. The markers indicate the points for which I was computed, the triangles and the squares designate the quadrupolar volume contributions of the Eulerian and of the viscous stresses respectively, while the circles indicate the dipolar viscous component. The continuous lines show functions of the kind Ma^6 while the dashed one follows Ma^4. The exponents indicate that the radiation is globally one dimensional, which is coherent with the previous results, since already at $Ma = 0.1$ the non planar components are marginal, and are negligible or absent for lower Ma. The acoustic intensity is

$$I = \int_S \int_\omega p'(\mathbf{x}, \omega) u_p(\mathbf{x}, -\omega) dS d\omega \tag{4.26}$$

in which S is the cross section and u_p is the axial particle velocity given by

$$\frac{\partial p'}{\partial x_3} + \rho \frac{\partial u_p}{\partial t} = 0$$

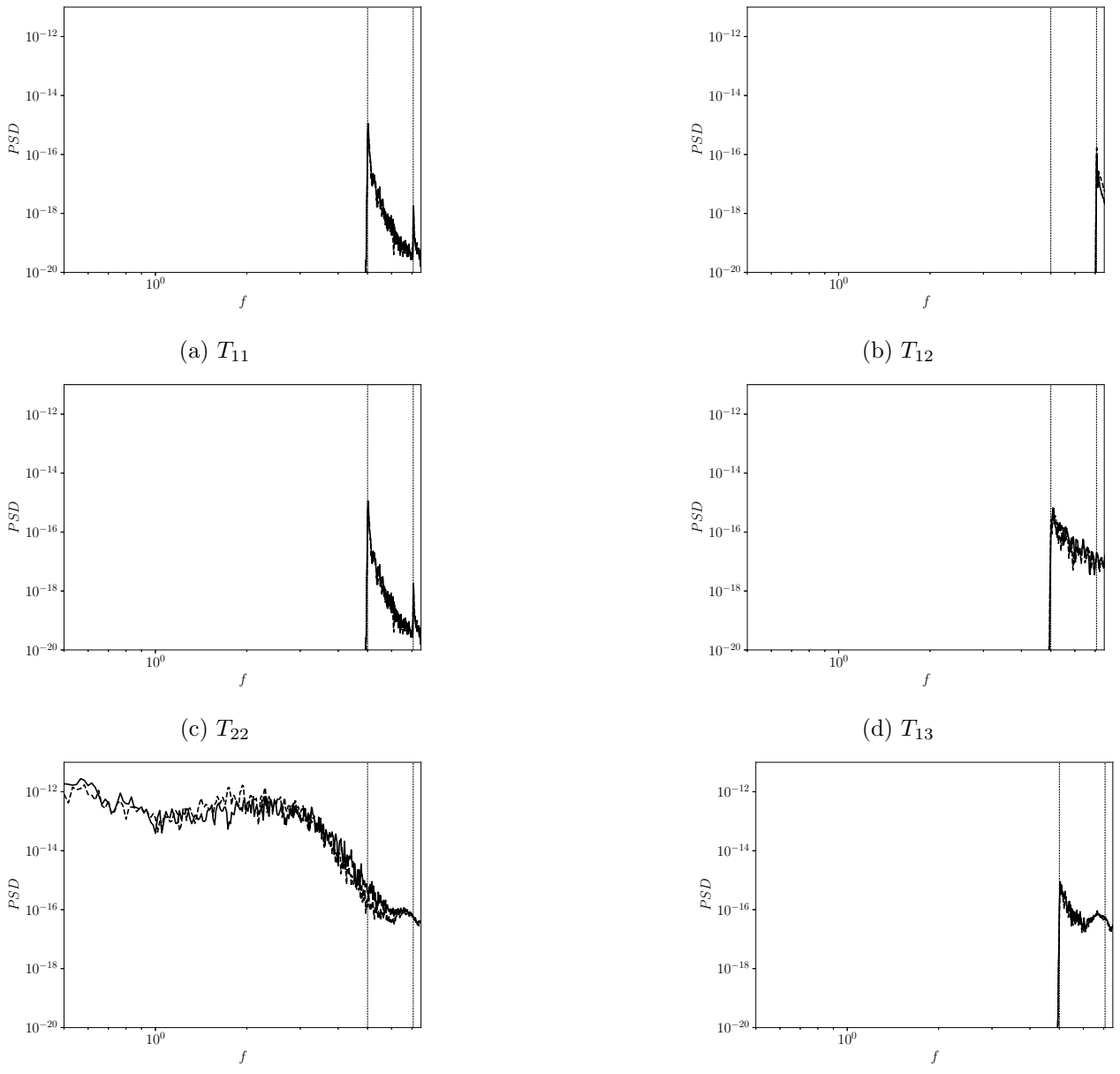

(a) T_{11} (b) T_{12}

(c) T_{22} (d) T_{13}

(e) T_{33} (f) T_{23}

Figure 4.17: Pressure fluctuations PSD spectra for each component of the Lighthill tensor computed at $x_3 = -150$ (black) and $x_3 = 150$ (red), $Ma = 0.1$. Turbulent puff in square duct, computed with the exact Green's function. The vertical lines indicate the cut-on frequencies for the (m, n) couples (1,0); (1,1) in this order, from left to right

which in Fourier space gives

$$u_p = \frac{k_{mn}}{\omega\rho} p'$$

I is computed from a grid of 16 points on the cross section, both upstream and downstream of the puff at a distance of 150 diameters using the equation above. Each contribution to the intensity is weighed by its wavenumber, thus I cannot in principle be computed just by integrating the spectrum. However if the radiation is planar we have only one contribution and

$$k_{mn}^2 = \frac{\omega}{c_\infty^2}, \qquad u_p = \frac{p}{\rho c_\infty}$$

Thus the noise intensity is the integral of the pressure spectrum.

The quadrupolar viscous component is always negligible, the scaling with Ma^6 is well respected up to $Ma = 0.3$, where possibly some 3D effects start to become visible, although the values remain well below the dominant inviscid component. The Eulerian contribution is dominant throughout almost the whole range of Ma, the dipolar component prevails only for $Ma < 2 \cdot 10^{-4}$. Such a low Ma for the crossing represents a difference with respect to previous results (Hu et al., 2003) who find $Ma = 0.1$ in the fully turbulent plane channel flow. This discrepancy may be due to the configuration or to the difference in Re, however one would expect that a lower Re would enhance the importance of viscous stresses, here on the contrary we see a lesser contribution of the viscous dipolar component. This effect may be linked to localisation and to the short range of x_3 in which the viscous stresses are strong, which is about $10/15h$, see figure 4.19.

The role of viscosity

The debate on the role of the viscous stresses in sound generation and/or propagation has been discussed in section 4.1.2. Acoustic attenuation at low frequency is based on the mechanism clarified by Howe (1995), turbulence responds quasi statically to acoustics, extracting energy from the acoustically warped 'mean' flow, thus producing an attenuation in the acoustic waves. On the contrary at high frequency the dissipation does not occur via an interaction with turbulence, but due to the bulk viscosity of the fluid, whose effect only becomes relevant if long distances (in terms of number of wavelengths) are involved. This last effect is thus important only for high frequencies and does not depend on the flow conditions. Following the procedure by Hu et al. (2003) we check whether the use of an acoustic analogy formulation not including the viscous dissipation effects is allowed. Neglecting

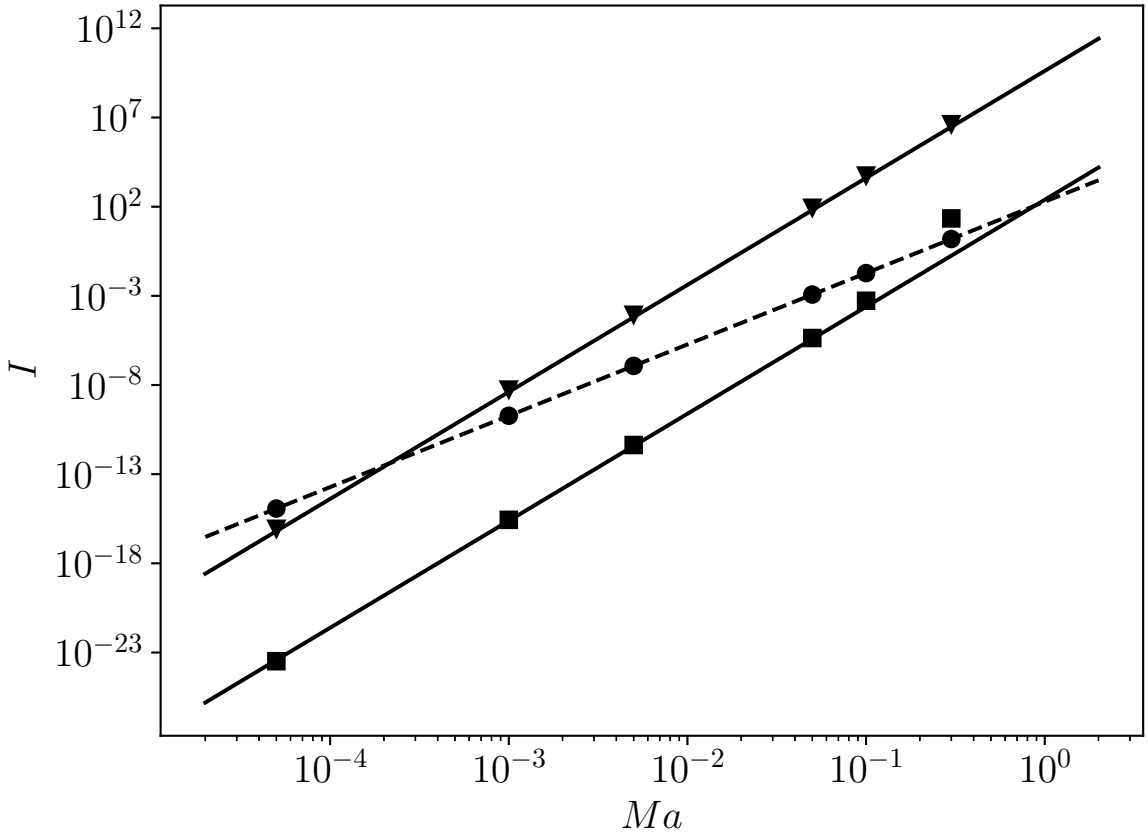

Figure 4.18: Far field sound radiation intensity contributions of the inviscid, quadrupolar component (▼), viscous, dipolar surface component (●), volumic, quadrupolar viscous component (■). The scaling lines represent functions of the kind Ma^6 (continuous) and Ma^4 (dashed).

the heat conduction of the fluid, the asymptotic values of attenuation coefficient α per wavelength λ are

$$\alpha\lambda(f \to 0) \simeq 1/f u_{\max}, \qquad \alpha\lambda(f \to \infty) \simeq \pi/\sqrt{2\sigma} \tag{4.27}$$

with

$$\sigma = 2\pi f h^2 Re_\tau$$

The quantities are scaled with the friction velocity u_τ. The lossless formulation is considered acceptable as long as the attenuation coefficient is small, namely smaller than 1. The determination of u_τ (or equivalently Re_τ) is to some degree arbitrary, since the value depends on the fraction of pipe length that we consider turbulent. Considering the whole domain would not settle the issue since the dependency would be attributed on the domain length. By assuming a puff length of $30h$ we obtain $u_\tau = 0.053$

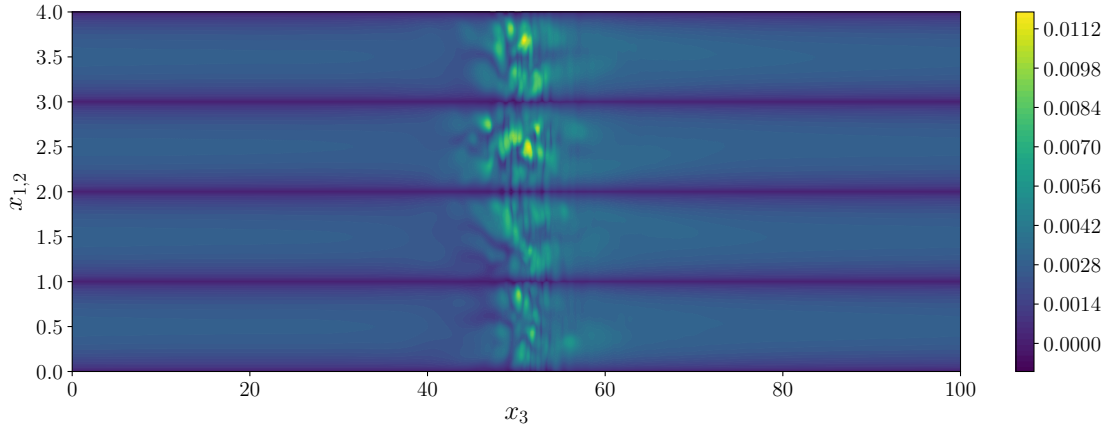

Figure 4.19: Wall viscous stress, plotted for the unfolded 4 walls. Snapshot of a turbulent puff simulation $Re = 1700$.

for a puff at $Re = 1700$, corresponding to $Re_\tau = 90$. The high frequency expression is valid for $f > 5 \cdot 10^{-3} Re_\tau$, for this frequency we have $\pi/\sqrt{2\sigma} \sim 0.14$, which is below 1 by an order of magnitude, higher frequencies give lower values of the attenuation coefficient. For the low frequency limit we calculate a threshold frequency below which the damping on the acoustic waves may be important. To consider the worst case scenario the maximum velocity is taken as the lowest centerline velocity ($u_{\max} = 0.97$), thus considering the turbulent region of the domain, and not as the global maximum velocity, which would be the laminar one. Paying attention to changing the non dimensionalisation of u_{max} to be coherent with the definitions above, while redefining U_b using the desired Ma and the properties of air at 20°C, the lower limit frequency for which a lossless formulation is applicable is $f_{\min} = 1/u_{\max}$. For $Ma = 0.3$ we obtain $f_{\min} = 2.65 \cdot 10^{-7}$, while for the crossing point $2 \cdot 10^{-4}$ we have $f_{\min} = 0.6$. This low frequency criterion however is applicable for $f < 10^{-3} Re_\tau = 0.09$ (Howe, 1995; Hu et al., 2003), therefore it cannot be applied here. This criterion determines whether or not turbulence interacts with acoustic waves extracting energy, however in the case of the puff turbulence is not present in a large part of the propagation zone, hence this analysis may not be necessary.

The conclusion that we draw from the scaling analysis, in the light of the present discussion is in accordance with Wang et al. (1996b); Hu et al. (2003) and with Landahl (1975); Shariff and Wang (2005). The viscous stresses are a noise source and do not act as a damper in this configuration, since the mechanisms involved in the damping according to Howe are either out of the frequency scope, or not applicable to the specific case due to the absence of turbulence in the noise propagation zone.

Chapter 5

Conclusions et perspectives

Conclusion

The majority of the literature considers puffs in an incompressible flow and a straight pipe configuration, only in recent years some works studied the influence of pipe curvature on transition to turbulence also discussing the effects on turbulent puffs' features by experiments (Kühnen et al., 2015) or by DNS, using the Navier-Stokes equations in polar coordinates (Rinaldi et al., 2019).

In this thesis we model the pipe curvature using an extended version of the simplified formulation by Dean and Hurst (1959). Through a dimensional analysis we justify Dean's assumptions and extend the model to unsteady, three dimensional flows in slightly bent pipes. This formulation neglects several terms of the cylindrical Navier-Stokes equations, curvature appears in the form of a single additional element in the nonlinear terms, in 3D the equations are parabolic in the streamwise direction confirming the validity of the parabolic hypothesis used by several authors (Sankar et al., 1988). The model is shown to accurately reproduce the bifurcation scenario of the 2D system in which, for increasing Dean number, the flow undergoes a double transition to chaos with stationary, periodic, aperiodic and chaotic regimes followed by a stationary region of De, and finally a new bifurcation to chaos. In 3D the model reproduces the flow development experiments by Bara et al. (1992), furthermore, when imposing a periodic boundary condition in the streamwise direction we retrieve a supercritical transition to traveling wave behavior, coherently with Watanabe and Yanase (2013). The death or survival of turbulent puffs in straight ducts depends on the flow Reynolds number, for higher Re puffs have more chances of surviving and even splitting, giving rise to new puffs, for low Re puffs tend to die more easily. The process is statistical and the Reynolds number, although controlling the probability,

is not a deterministic parameter. Curvature adds a second governing parameter, the Dean number, that together with a fixed Re determines more precisely the short term fate of puffs. The simplified model is not apt for turbulence due to the missing terms, the analysis of the effect of curvature on turbulent puffs is performed by imposing a scale separation. This approach is limited to weak bends, but has the advantage of separating the laminar effects of curvature from the turbulent features. This method could be regarded as a low cost alternative for the low curvature analyses. The approach that uses DNS with polar coordinates is in principle flawless, but results in very expensive calculations in the low curvature limit. The present method is more and more justified when curvature tends to zero, with a negligible additional computing cost with respect to the straight case.

The effects of compressibility of turbulent puffs have not been studied in the literature, due to the low Re nature of the flow which can be associated to a low Ma. We explored the hypothesis of a long distance interaction between puffs, that may be associated to an acoustic mechanism computing the noise field by means of an acoustic analogy derived from Curle's formulation. The noise is strongly affected by the geometry, the spectra computed in the theoretical free space case being radically different from the ones computed taking into account the effect of the walls. The cut on-off effects strongly alter the shape of the spectrum, inhibiting the propagation of a large part of the spectrum, which presents distinct peaks in correspondence to the cut-on frequencies. A selection in the low frequency limit is not observed, suggesting the non existence of an equilibrium distance based on acoustic grounds. In addition to characterising the acoustic field of the puff, we used this case to provide some elements of discussion to a literature argument concerning the importance of the viscous stresses in the aeroacoustic noise generation. For $Ma \sim 2 \cdot 10^{-4}$ the dipolar noise associated to the viscous stresses dominates the noise radiation, this is in qualitative agreement with the findings by Hu et al. (2003), who however considered a fully turbulent plane channel flow and retrieved a dipolar domination at a much higher Mach number: 0.01. This result may indicate that the dipolar terms dominate in a Mach number regime where the acoustic waves are damped by interaction with turbulent fluctuations Howe (1979), however the flow is turbulent only within the puff, and not in the remaining propagation zone, thus this mechanism should have a marginal importance in this specific case.

Perspectives

Several aspects would be worth further investigations. The first would probably be the compressible case. Appendix D presents a preliminar calculation of a puff using a high order compressible code (MUSICA). This analysis could be complementary to the acoustic analogy by providing a direct noise computation, clarifying the validity of the no-flow hypothesis. Moreover a compressible framework would open new possibilities, such as the analysis of the response of a turbulent puff to an acoustic forcing, that might potentially be yet another way to damp turbulence in pipes (Hof et al., 2010; Kühnen et al., 2018; Ding et al., 2020), this time not acting on the laminar inflow but on the fluctuations.

A continuation of the work concerning puffs and bent ducts would be aimed at clarifying the nature of the bifurcation to turbulence at sufficiently high curvatures. This has been recently deemed supercritical (Kühnen et al., 2015; Canton et al., 2020). It is the case, but in the light of the works from the 1980s and 90s (Winters, 1987) we know that the supercritical bifurcation occurs from a stationary flow to a periodic flow in 2D, and in 3D to a traveling wave, that is laminar. The bifurcation from the stationary solution does follow a bifurcation cascade, in which the first step is the traveling wave solution. But if we search for a bifurcation from a laminar to a turbulent flow we should probably look at the bifurcation from the traveling wave, that may remain subcritical. The formulation presented in chapter 3 could provide a valuable tool, separating the laminar effects of curvature and turbulence. Another aspect to explore may be that of particle separation for sorting devices. Adding a passive scalar to the model would allow the study of the role of Dean vortices in the localisation on the section of particles with different weights. The model can be extended to include the influence of temperature gradients along the cross section by adding a buoyancy term and an equation for temperature. The effect would be analogous to the one given by curvature, with the formation of counter rotating vortices for the any non-zero temperature gradients.

A more applied branch of this work could be that of considering the fluid-structure interaction between the puffs and the pipe. There are several sources of excitation for the pipe, depending on the structural characteristics and on the fluid. At the Reynolds numbers at which puffs exist we may have frequencies related to the period of puff passage, to the puff turbulent frequencies or to acoustics. Curvature can also be a key ingredient in the study of puffs and turbulence; in chapter 3 we showed

that for relatively low Dean numbers puffs consistently relaminarise. In a practical application this low curvature may seem negligible, but in some cases it can be sufficient to strongly influence the flow. The following section gives some quantitative examples, namely concerning the pipe vibration and curvature.

Quantitative examples

Vibration of a cantilever pipe with flowing air

As a quantitative example of vibrations in pipe flow we consider a pipe of square cross section fixed on a wall on one side, and free to oscillate on the other, as depicted in figure 5.1. Following Meirovitch

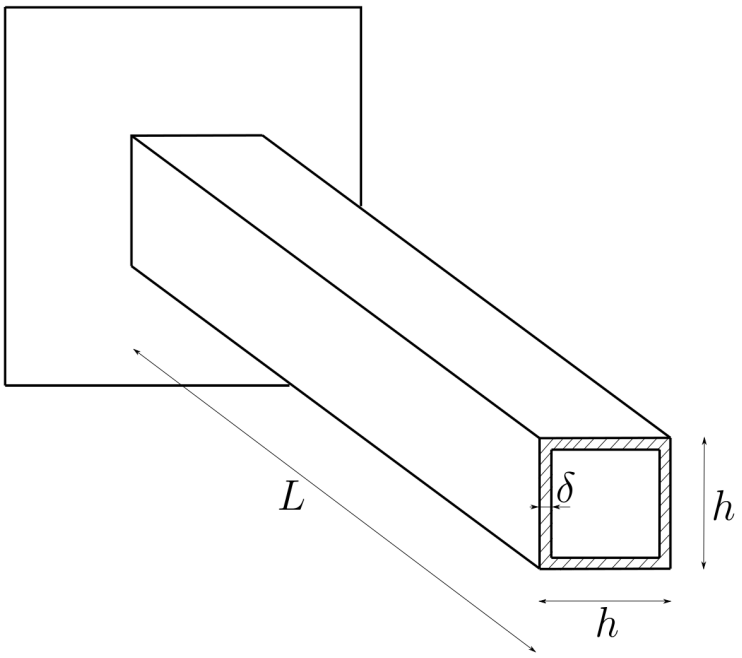

Figure 5.1: Sketch of the cantilever pipe of square cross section

(1967), the governing equation is

$$\frac{d^2}{dx^2}\left[EI\frac{d^2Y(x)}{dx^2}\right] = \omega m(x)Y(x) \tag{5.1}$$

Table 5.1: Details of the pipe geometries 1, 2, 3, 4 (in metres)

	h	L	δ
1	0.1	1	$2 \cdot 10^{-3}$
2	0.05	1	$2 \cdot 10^{-4}$
3	0.01	1	$2 \cdot 10^{-4}$
4	0.1	4	$2 \cdot 10^{-3}$

Table 5.2: First natural frequency (in Hertz) of the cantilever for pipes built with the geometries 1,2,3,4 and different materials (steel and copper)

	steel	copper
1	116.97	82.89
2	58.96	41.77
3	11.70	8.29
4	7.31	5.18

where E is the Young modulus of the material, m is the mass per unit length, and ω is the pulsation. I is the moment of inertia, that is dependent on the cross section of the beam. In the case of a duct of square cross section with duct side h and wall width δ it is

$$I = \frac{h^4}{12} - \frac{(h-\delta)^4}{12}$$

A closed form solution is found by imposing the boundary conditions (nil displacement and derivative at $x = 0$, and nil second and third derivative of displacement at $x = L$) The natural frequencies of a cantilever beam are

$$f = \frac{1}{2\pi}\omega_{nf} = \alpha_n^2\sqrt{\frac{EI}{mL^4}} = \alpha_n^2\sqrt{\frac{EI}{A_p\rho_p L^4}}$$

with A_p, ρ_p being the external pipe section and material density (the subscript p stands for pipe). The first values of the infinite series of α_n are

$$\alpha_n = 1.875,\ 4.694,\ 7.885,\ 10.996,\ 14.137,\ 17.279,\ ...$$

We will consider different pipe geometries (indicated with the subscripts 1,2,3,4) and two materials: steel and copper. The details of the geometries are summarized in table 5.1

Steel has a Young modulus $E = 2.1 \cdot 10^{11} Pa$ and density $\rho_p = 7850 kg/m^3$, while copper has $E = 1.2 \cdot 10^{11} Pa$ and $\rho_p = 8933 kg/m^3$. Table 5.2 shows the first natural frequencies in the cases considered. Assuming $Re = 1700$ and air as the working fluid ($\nu = 1.52 \cdot 10^{-5}$) we can compute the flow bulk velocity U_b, the minimal puff distance is around $D = 30h$, assuming a constant distance between puffs we can

calculate the frequency of the puffs crossing a given pipe section. $f = (D/U_b)^{-1} = (D/(\nu Re/h))^{-1}$. The puff passage frequencies for the three geometries are reported in table 5.3,the only geometry for which the frequency of puff passage may excite the natural pipe mode is number 3. The flow velocity is considerable for a diameter of $1cm$, but remains reasonable for an industrial application, this implies that low Reynolds number flows in the industry (e.g. electronics, microfluidics) might be subjected to vibrations caused by the passage of puffs. Another source of excitation of the structural modes could in principle be represented by turbulence and by the acoustic noise produced by it. We start analysing the highest velocity case (geometry number 3) for which U_b is 2.58 (always for air and $Re = 1700$, and considering a copper pipe). The non dimensional frequency corresponding to the first natural vibration mode is $fU_b/h = 8.29 \times 2.58/0.01 \sim 2139$, this frequency is much higher than any of the frequencies present in the puff's turbulence or noise spectra, that are of $\mathcal{O}(1)$ (see figures 4.12) this is the lowest of the pipe natural frequencies, thus turbulence or acoustics are not able to trigger any vibrational mode. For the lowest velocity cases we have $fU_b/h = 82.89 \times 0.26/0.1 \sim 215$ (geometry 1) and $fU_b/h = 5.18 \times 0.26/0.1 \sim 13$ (geometry 4, that presents a larger pipe length). We see that the pipe length deeply affects the natural vibration frequency, while for geometry 1 this is larger than the values present in the turbulence or acoustic spectra, for geometry 4 the values are slightly larger but comparable with the flow frequencies, meaning that the puffs' turbulence may trigger the duct structural modes.

Table 5.3: Puff passing frequencies (in Hertz) and flow bulk velocities (m/s), computed for the three geometries considered

	f	U_b
1	0.09	0.26
2	0.35	0.52
3	8.61	2.58
4	0.09	0.26

Influence of a small duct curvature on a puff

In chapter 3 we showed that curvature can radically influence the shape of puffs and inhibit turbulence. In particular a turbulent puff at $Re = 1500$ is long-lived for $De = 30$ and consistently dies after $\mathcal{O}(10)$ time units for $De = 40$. For an experimentalist it would be of interest to relate these non dimensional quantities to real life lengths and speeds. Supposing we perform an experiment

using a pipe with $h = 10mm$ (Samanta et al. (2011) used a circular pipe with the same diameter), for $Re = 1500$ and $De = 30$ the curvature radius is $R = 25m$, and $R = 14$ for $De = 40$. For a pipe length of $1m$, assuming a perfectly circular curvature this corresponds to deviations of about 5 and $7mm$ from the nominal straight line, which may be present even in a rather finely assembled setup. Such curvature would probably not be acceptable in an experiment, but it might be present in a more industrial application. We know that in a square duct at these condition the puff would be deformed or relaminarise due to the effect of curvature at $De = 40$. In an industrial application this phenomenon might be exploited to reduce drag in a pipe by inhibiting turbulence.

Bibliography

K. Avila, D. Moxey, A. de Lozar, M. Avila, D. Barkley, and B. Hof. The onset of turbulence in pipe flow. *Science*, 333(6039):192–196, 2011. ISSN 0036-8075.

C. Bailly and C. Bogey. Contributions of computational aeroacoustics to jet noise research and prediction. *International Journal of Computational Fluid Dynamics*, 18:481–491, 08 2004.

C. Bailly and D. Juvé. Numerical solution of acoustic propagation problems using linearized euler equations. *AIAA Journal*, 38(1):22–29, 2000.

P. R. Bandyopadhyay. Aspects of the equilibrium puff in transitional pipe flow. *Journal of Fluid Mechanics*, 163:439–458, 1986.

B. Bara, K. Nandakumar, and J. H. Masliyah. An experimental and numerical study of the dean problem: flow development towards two-dimensional multiple solutions. *Journal of Fluid Mechanics*, 244:339–376, 1992.

D. Barkley. Theoretical perspective on the route to turbulence in a pipe. *Journal of Fluid Mechanics*, 803:P1, 2016.

D. Barkley. Taming turbulent fronts by bending pipes. *Journal of Fluid Mechanics*, 872:1–4, 2019.

D. Barkley and L. S. Tuckerman. Computational study of turbulent laminar patterns in couette flow. *Physical review letters*, 94(1):014502, 2005.

D. Barkley, B. Song, V. Mukund, G. Lemoult, M. Avila, and B. Hof. The rise of fully turbulent flow. *Nature*, 526(7574):550–553, 2015.

A. Bayliss, A. Class, and B. Matkowsky. Roundoff error in computing derivatives using the chebyshev

differentiation matrix. *Journal of Computational Physics*, 116(2):380–383, Feb. 1995. ISSN 0021-9991.

S. A. Berger, L. Talbot, and L. S. Yao. Flow in curved pipes. *Annual Review of Fluid Mechanics*, 15 (1):461–512, 1983.

O. Botella. On the solution of the navier-stokes equations using chebyshev projection schemes with third-order accuracy in time. *Computers & Fluids*, 26(2):107–116, 1997.

J. Canton, P. Schlatter, and R. Örlü. Modal instability of the flow in a toroidal pipe. *Journal of Fluid Mechanics*, 792:894–909, 2016.

J. Canton, R. Örlü, and P. Schlatter. Characterisation of the steady, laminar incompressible flow in toroidal pipes covering the entire curvature range. *International Journal of Heat and Fluid Flow*, 66:95 – 107, 2017. ISSN 0142-727X.

J. Canton, E. Rinaldi, R. Örlü, and P. Schlatter. Critical point for bifurcation cascades and featureless turbulence. *Physical Review Letters*, 124(1):014501, 2020.

M. Chantry, L. S. Tuckerman, and D. Barkley. Turbulent–laminar patterns in shear flows without walls. *Journal of Fluid Mechanics*, 791:R8, 2016.

K. Cheng and M. Akiyama. Laminar forced convection heat transfer in curved rectangular channels. *International Journal of Heat and Mass Transfer*, 13(3):471–490, 1970.

K. C. Cheng, R. C. Lin, and J. W. Ou. Fully developed laminar flow in curved rectangular channels. *Journal of Fluids Engineering, Transactions of the ASME*, 98:41–48, 03 1976.

A. J. Chorin. Numerical solution of the navier-stokes equations. *Mathematics of computation*, 22(104): 745–762, 1968.

K. Cieślicki and A. Piechna. Can the Dean number Alone Characterize Flow Similarity in Differently Bent Tubes? *Journal of Fluids Engineering*, 134(5), 05 2012. ISSN 0098-2202. 051205.

D. Coles. Transition in circular couette flow. *Journal of Fluid Mechanics*, 21(3):385–425, 1965.

D. Coles and C. Van Atta. Measured distortion of a laminar circular couette flow by end effects. *Journal of Fluid Mechanics*, 25(3):513–521, 1966.

T. Colonius and S. K. Lele. Computational aeroacoustics: progress on nonlinear problems of sound generation. *Progress in Aerospace Sciences*, 40(6):345 – 416, 2004. ISSN 0376-0421.

P. Croaker, N. Kessissoglou, and S. Marburg. A cfd-bem coupling technique for low mach number flow induced noise. In *Proc Acoustics*, pages 17–20, 2013.

S. C. Crow. Aerodynamic sound emission as a singular perturbation problem. *Studies in Applied Mathematics*, 49(1):21–46, 1970.

N. Curle. The influence of solid boundaries upon aerodynamic sound. *Proceedings of the Royal Society of London. Series A. Mathematical and Physical Sciences*, 231(1187):505–514, 1955.

P. Daskopoulos and A. Lenhoff. Flow in curved ducts: bifurcation structure for stationary ducts. *Journal of Fluid Mechanics*, 203:125–148, 1989.

H. G. Davies and J. E. Ffowcs Williams. Aerodynamic sound generation in a pipe. *Journal of Fluid Mechanics*, 32(4):765–778, 1968.

A. De Lozar and B. Hof. An experimental study of the decay of turbulent puffs in pipe flow. *Philosophical Transactions of the Royal Society A: Mathematical, Physical and Engineering Sciences*, 367 (1888):589–599, 2009.

W. Dean. Xvi. note on the motion of fluid in a curved pipe. *The London, Edinburgh, and Dublin Philosophical Magazine and Journal of Science*, 4(20):208–223, 1927.

W. Dean. Lxxii. the stream-line motion of fluid in a curved pipe (second paper). *The London, Edinburgh, and Dublin Philosophical Magazine and Journal of Science*, 5(30):673–695, 1928.

W. R. Dean and S. Chapman. Fluid motion in a curved channel. *Proceedings of the Royal Society of London. Series A, Containing Papers of a Mathematical and Physical Character*, 121(787):402–420, 1928.

W. R. Dean and J. M. Hurst. Note on the motion of fluid in a curved pipe. *Mathematika*, 6(1):77–85, 1959.

S. Dennis and M. NG. Dual solutions for steady laminar flow through a curved tube. *The Quarterly Journal of Mechanics and Applied Mathematics*, 35(3):305–324, 1982.

Z. Ding, E. Marensi, A. Willis, and R. Kerswell. Stabilising pipe flow by a baffle designed using energy stability. *Journal of Fluid Mechanics*, 902, 2020.

P. Drazin and W. Reid. Hydrodynamic stability, 1981.

Y. Duguet and P. Schlatter. Oblique laminar-turbulent interfaces in plane shear flows. *Physical review letters*, 110(3):034502, 2013.

Y. Duguet, P. Schlatter, and D. S. Henningson. Formation of turbulent patterns near the onset of transition in plane couette flow. *Journal of Fluid Mechanics*, 650:119, 2010a.

Y. Duguet, A. P. Willis, and R. R. Kerswell. Slug genesis in cylindrical pipe flow. *Journal of Fluid Mechanics*, 663:180–208, 2010b.

U. Ehrenstein and R. Peyret. A chebyshev collocation method for the navier–stokes equations with application to double-diffusive convection. *International Journal for Numerical Methods in Fluids*, 9(4):427–452, 1989.

J. Eustice and J. Larmor. Flow of water in curved pipes. *Proceedings of the Royal Society of London. Series A, Containing Papers of a Mathematical and Physical Character*, 84(568):107–118, 1910.

J. Ffowcs Williams and D. L. Hawkings. Sound generation by turbulence and surfaces in arbitrary motion. *Philosophical Transactions for the Royal Society of London. Series A, Mathematical and Physical Sciences*, pages 321–342, 1969.

F. R. S. G. I. Taylor. The criterion for turbulence in curved pipes. *Proceedings of the Royal Society of London A: Mathematical, Physical and Engineering Sciences*, 124(794):243–249, 1929. ISSN 0950-1207.

X. Gloerfelt and J. Berland. Turbulent boundary-layer noise: direct radiation at mach number 0.5. *Journal of Fluid Mechanics*, 723:318–351, 2013.

E. Greshilov and M. Mironov. Experimental evaluation of sound generated by turbulent flow in a hydrodynamic duct. *SPhAc*, 29:275–280, 1983.

J.-L. Guermond, P. Minev, and J. Shen. An overview of projection methods for incompressible flows. *Computer methods in applied mechanics and engineering*, 195(44-47):6011–6045, 2006.

D. B. Haidvogel and T. Zang. The accurate solution of poisson's equation by expansion in chebyshev polynomials. *Journal of Computational Physics*, 30(2):167–180, 1979.

P. Haldenwang, G. Labrosse, S. Abboudi, and M. Deville. Chebyshev 3-d spectral and 2-d pseudospectral solvers for the helmholtz equation. *Journal of Computational Physics*, 55(1):115–128, 1984.

H. H. Hariri and T. Akylas. The wall-shear-stress contribution to boundary-layer noise. *The Physics of fluids*, 28(9):2727–2729, 1985.

F. J. Harris. On the use of windows for harmonic analysis with the discrete fourier transform. *Proceedings of the IEEE*, 66(1):51–83, 1978.

H. Hinrichsen. Non-equilibrium critical phenomena and phase transitions into absorbing states. *Advances in Physics*, 49(7):815–958, 2000.

B. Hof, A. De Lozar, M. Avila, X. Tu, and T. M. Schneider. Eliminating turbulence in spatially intermittent flows. *science*, 327(5972):1491–1494, 2010.

M. Howe. Contributions to the theory of aerodynamic sound, with application to excess jet noise and the theory of the flute. *Journal of Fluid Mechanics*, 71(4):625–673, 1975.

M. Howe. The role of surface shear stress fluctuations in the generation of boundary layer noise. *Journal of Sound and Vibration*, 65(2):159–164, 1979.

M. Howe. The damping of sound by wall turbulent shear layers. *The Journal of the Acoustical Society of America*, 98(3):1723–1730, 1995.

Z. Hu, C. L. Morfey, and N. D. Sandham. Sound radiation in turbulent channel flows. *Journal of Fluid Mechanics*, 475:269–302, 2003.

Z. Hu, C. L. Morfey, and N. D. Sandham. Sound radiation from a turbulent boundary layer. *Physics of Fluids*, 18(9):098101, 2006.

H. Ito. Friction Factors for Turbulent Flow in Curved Pipes. *Journal of Basic Engineering*, 81(2): 123–132, 06 1959. ISSN 0021-9223.

H. Ito. Laminar flow in curved pipes. *ZAMM - Journal of Applied Mathematics and Mechanics / Zeitschrift für Angewandte Mathematik und Mechanik*, 49(11):653–663, 1969.

B. Joseph, E. P. Smith, and R. J. Adler. Numerical treatment of laminar flow in helically coiled tubes of square cross section. part i. stationary helically coiled tubes. *AIChE Journal*, 21(5):965–974, 1975.

A. Kalpakli Vester, R. Örlü, and P. H. Alfredsson. Turbulent Flows in Curved Pipes: Recent Advances in Experiments and Simulations. *Applied Mechanics Reviews*, 68(5), 09 2016. ISSN 0003-6900.

T. Kambe. Influence of viscosity on aerodynamic sound emission in free space. *Journal of sound and vibration*, 95(3):351–360, 1984.

A. Kolmogorov. The Local Structure of Turbulence in Incompressible Viscous Fluid for Very Large Reynolds' Numbers. *Akademiia Nauk SSSR Doklady*, 30:301–305, Jan. 1941.

V. Koschatzky, J. Westerweel, and B. J. Boersma. A study on the application of two different acoustic analogies to experimental piv data. *Physics of Fluids*, 23(6):065112, 2011.

J. Kühnen, M. Holzner, B. Hof, and H. Kuhlmann. Experimental investigation of transitional flow in a toroidal pipe. *Journal of Fluid Mechanics*, 738:463–491, 2014.

J. Kühnen, M. Holzner, B. Hof, and H. C. Kuhlmann. Experimental investigation of transitional flow in a toroidal pipe. *Journal of Fluid Mechanics*, 738:463–491, 2014.

J. Kühnen, P. Braunshier, M. Schwegel, H. C. Kuhlmann, and B. Hof. Subcritical versus supercritical transition to turbulence in curved pipes. *Journal of Fluid Mechanics*, 770:R3, 2015.

J. Kühnen, B. Song, D. Scarselli, N. B. Budanur, M. Riedl, A. Willis, M. Avila, and B. Hof. Destabilizing turbulence in pipe flow. *Nature Physics*, 14, 04 2018.

J. Kühnen, B. Song, D. Scarselli, N. B. Budanur, M. Riedl, A. P. Willis, M. Avila, and B. Hof. Destabilizing turbulence in pipe flow. *Nature Physics*, 14(4):386–390, 2018.

J. Kühnen, D. Scarselli, and B. Hof. Relaminarization of pipe flow by means of 3d-printed shaped honeycombs. *Journal of Fluids Engineering*, 141(11), 2019.

M. T. Landahl. Wave mechanics of boundary layer turbulence and noise. *The Journal of the Acoustical Society of America*, 57(4):824–831, 1975.

M. J. Lighthill. On sound generated aerodynamically i. general theory. *Proceedings of the Royal Society of London. Series A. Mathematical and Physical Sciences*, 211(1107):564–587, 1952.

E. R. Lindgren. Propagation velocity of turbulent slugs and streaks in transition pipe flow. *The Physics of Fluids*, 12(2):418–425, 1969.

A. S. Lyrintzis. Review: The Use of Kirchhoff's Method in Computational Aeroacoustics. *Journal of Fluids Engineering*, 116(4):665–676, 12 1994. ISSN 0098-2202.

R. W. MacCormack. The effect of viscosity in hypervelocity impact cratering. *Journal of spacecraft and rockets*, 40(5):757–763, 2003.

P. Martínez-Lera, C. Schram, H. Bériot, and R. Hallez. An approach to aerodynamic sound prediction based on incompressible-flow pressure. *Journal of Sound and Vibration*, 333(1):132–143, 2014.

D. J. McConalogue and R. S. . Srivastava. Motion of a fluid in a curved tube. *Proceedings of the Royal Society of London. Series A. Mathematical and Physical Sciences*, 307(1488):37–53, 1968.

P. A. J. Mees, K. Nandakumar, and J. H. Masliyah. Secondary instability of flow in a curved duct of square cross-section. *Journal of Fluid Mechanics*, 323:387–409, 1996.

L. Meirovitch. *Fundamentals of vibrations*. McGraw Hill, 1967.

B. E. Mitchell, S. K. Lele, and P. Moin. Direct computation of the sound from a compressible co-rotating vortex pair. *Journal of Fluid Mechanics*, 285:181–202, 1995.

D. Modesti, S. Pirozzoli, and F. Grasso. Direct numerical simulation of developed compressible flow in square ducts. *International Journal of Heat and Fluid Flow*, 76:130 – 140, 2019. ISSN 0142-727X.

R. N. Mondal, Y. Kaga, T. Hyakutake, and S. Yanase. Bifurcation diagram for two-dimensional steady flow and unsteady solutions in a curved square duct. *Fluid Dynamics Research*, 39(5):413, 2007.

C. Morfey. Amplification of aerodynamic noise by convected flow inhomogeneities. *Journal of Sound and Vibration*, 31(4):391–397, 1973.

C. Morfey. The role of viscosity in aerodynamic sound generation. *International Journal of Aeroacoustics*, 2(3):225–240, 2003.

C. Morfey, S. Sorokin, and G. Gabard. The effects of viscosity on sound radiation near solid surfaces. *Journal of fluid mechanics*, 690:441–460, 2012.

V. Mukund and B. Hof. The critical point of the transition to turbulence in pipe flow. *Journal of Fluid Mechanics*, 839:76–94, 2018.

J. Nikuradse. Untersuchungen über turbulente strömungen in nicht kreisförmigen rohren. *Ingenieur-archiv*, 1(3):306–332, 1930.

M. Norouzi and N. Biglari. An analytical solution for dean flow in curved ducts with rectangular cross section. *Physics of Fluids*, 25, 05 2013.

F. Obermeier. Aerodynamic sound generation caused by viscous processes. *Journal of Sound and Vibration*, 99(1):111–120, 1985.

S. A. Orszag. On the elimination of aliasing in finite-difference schemes by filtering high-wavenumber components. *Journal of the Atmospheric sciences*, 28(6):1074–1074, 1971.

A. Pierce. *Acoustics: An Introduction to Its Physical Principles and Applications*, volume 34, pages 316–317. Acoustical Society of America, 06 1989.

A. Pinelli, M. Uhlmann, A. Sekimoto, and G. Kawahara. Reynolds number dependence of mean flow structure in square duct turbulence. *Journal of fluid mechanics*, 644:107–122, 2010.

S. Pirozzoli, D. Modesti, P. Orlandi, and F. Grasso. Turbulence and secondary motions in square duct flow. *Journal of Fluid Mechanics*, 840:631–655, 2018.

A. Powell. Aerodynamic noise and the plane boundary. *The Journal of the Acoustical Society of America*, 32(8):982–990, 1960.

A. Powell. Theory of vortex sound. *The Journal of the Acoustical Society of America*, 36(1):177–195, 1964.

L. Prandtl. The generation of vortices in fluids of small viscosity. *The Aeronautical Journal*, 31(200): 718–741, 1927.

A. Prigent, G. Grégoire, H. Chaté, and O. Dauchot. Long-wavelength modulation of turbulent shear flows. *Physica D: Nonlinear Phenomena*, 174(1-4):100–113, 2003.

V. Priymak and T. Miyazaki. Direct numerical simulation of equilibrium spatially localized structures in pipe flow. *Physics of Fluids*, 16(12):4221–4234, 2004.

O. Reynolds. Xxix. an experimental investigation of the circumstances which determine whether the motion of water shall be direct or sinuous, and of the law of resistance in parallel channels. *Philosophical Transactions of the Royal Society of London*, 174:935–982, 1883.

E. Rinaldi, J. Canton, and P. Schlatter. The vanishing of strong turbulent fronts in bent pipes. *Journal of Fluid Mechanics*, 866:487–502, 2019.

D. Ruelle and F. Takens. On the nature of turbulence. *Les rencontres physiciens-mathématiciens de Strasbourg-RCP25*, 12:1–44, 1971.

D. Samanta, A. De Lozar, and B. Hof. Experimental investigation of laminar turbulent intermittency in pipe flow. *Journal of fluid mechanics*, 681:193–204, 2011.

R. Sankar, K. Nandakumar, and J. Masliyah. Oscillatory flows in coiled square ducts. *The Physics of fluids*, 31(6):1348–1359, 1988.

C. Schram. A boundary element extension of curle's analogy for non-compact geometries at low-mach numbers. *Journal of Sound and Vibration - J SOUND VIB*, 322:264–281, 04 2009.

R. Shanthini and K. Nandakumar. Bifurcation phenomena of generalized newtonian fluids in curved rectangular ducts. *Journal of Non-newtonian Fluid Mechanics*, 22:35–60, 12 1986.

K. Shariff and M. Wang. A numerical experiment to determine whether surface shear-stress fluctuations are a true sound source. *Physics of Fluids*, 17(10):107105, 2005.

H.-Y. Shih, T.-L. Hsieh, and N. Goldenfeld. Ecological collapse and the emergence of travelling waves at the onset of shear turbulence. *Nature Physics*, 12(3):245–248, 2016.

M. Shimizu and S. Kida. A driving mechanism of a turbulent puff in pipe flow. *Fluid Dynamics Research*, 41(4):045501, 2009.

W. Y. Soh. Developing fluid flow in a curved duct of square cross-section and its fully developed dual solutions. *Journal of Fluid Mechanics*, 188:337–361, 1988.

A. Sommerfeld. *Ein beitrag zur hydrodynamischen erklaerung der turbulenten fluessigkeitsbewegungen.* 1908.

B. Song, D. Barkley, B. Hof, and M. Avila. Speed and structure of turbulent fronts in pipe flow. *Journal of Fluid Mechanics*, 813:1045–1059, 2017.

K. R. Sreenivasan and P. J. Strykowski. Stabilization effects in flow through helically coiled pipes. *Experiments in Fluids*, 1(1):31–36, Mar 1983. ISSN 1432-1114.

K. Takeishi, G. Kawahara, H. Wakabayashi, M. Uhlmann, and A. Pinelli. Localized turbulence structures in transitional rectangular-duct flow. *Journal of Fluid Mechanics*, 782:368–379, 2015.

T. Tatsumi and T. Yoshimura. Stability of the laminar flow in a rectangular duct. *Journal of Fluid Mechanics*, 212:437–449, 1990.

G. I. Taylor. Viii. stability of a viscous liquid contained between two rotating cylinders. *Philosophical Transactions of the Royal Society of London. Series A, Containing Papers of a Mathematical or Physical Character*, 223(605-615):289–343, 1923.

R. Temam. Une méthode d'approximation de la solution des équations de navier-stokes. *Bulletin de la Société Mathématique de France*, 96:115–152, 1968.

L. N. Trefethen. *Spectral methods in MATLAB*. SIAM, 2000.

L. N. Trefethen, A. E. Trefethen, S. C. Reddy, and T. A. Driscoll. Hydrodynamic stability without eigenvalues. *Science*, 261(5121):578–584, 1993.

L. S. Tuckerman. Computational challenges of nonlinear systems. In *Emerging Frontiers in Nonlinear Science*, pages 249–277. Springer, 2020.

L. S. Tuckerman, M. Chantry, and D. Barkley. Patterns in wall-bounded shear flows. *Annual Review of Fluid Mechanics*, 52, 2020.

M. Van Dyke. Extended Stokes series: laminar flow through a loosely coiled pipe. *Journal of Fluid Mechanics*, 86(1):129–145, 1978.

F. Waleffe. On a self-sustaining process in shear flows. *Physics of Fluids*, 9(4):883–900, 1997.

L. Wang and T. Yang. Bifurcation and stability of forced convection in curved ducts of square cross-section. *International Journal of Heat and Mass Transfer*, 47(14):2971 – 2987, 2004. ISSN 0017-9310.

L. Wang and T. Yang. Periodic oscillation in curved duct flows. *Physica D: Nonlinear Phenomena*, 200(3):296 – 302, 2005. ISSN 0167-2789.

M. Wang, S. K. Lele, and P. Moin. Computation of quadrupole noise using acoustic analogy. *AIAA Journal*, 34(11):2247–2254, 1996a.

M. Wang, S. K. Lele, and P. Moin. Sound radiation during local laminar breakdown in a low-mach-number boundary layer. *Journal of Fluid Mechanics*, 319:197–218, 1996b.

T. Watanabe and S. Yanase. Bifurcation study of three-dimensional solutions of the curved square-duct flow. *Journal of the Physical Society of Japan*, 82(7):074402, 2013.

M. Watrigant. *Investigation des méthodes d'estimation en aéroacoustique automobile par résolution temporelle rapide des équations intégrales*. PhD thesis, Poitiers, 2010.

C. M. White. Streamline flow through curved pipes. *Proceedings of the Royal Society of LondonContaining Papers of a Mathematical and Physical Character*, 123(792):645–663, 1929.

K. H. Winters. A bifurcation study of laminar flow in a curved tube of rectangular cross-section. *Journal of Fluid Mechanics*, 180:343–369, 1987.

I. Wygnanski, M. Sokolov, and D. Friedman. On transition in a pipe. part 2. the equilibrium puff. *Journal of Fluid Mechanics*, 69(2):283–304, 1975.

I. J. Wygnanski and F. H. Champagne. On transition in a pipe. part 1. the origin of puffs and slugs and the flow in a turbulent slug. *Journal of Fluid Mechanics*, 59(2):281–335, 1973.

S. Yanase, N. Goto, and K. Yamamoto. Stability of dual solutions of the flow in a curved circular tube. *Journal of the Physical Society of Japan*, 57(8):2602–2604, 1988.

S. Yanase, N. Goto, and K. Yamamoto. Dual solutions of the flow through a curved tube. *Fluid Dynamics Research*, 5(3):191, 1989.

Appendix A

Python program for the solution of the 2D Dean problem

Pages 137 and 138 contain the source code used to generate the data concerning the 2D results shown in chapter 3. This version of the code mostly contains the calculating core of the program, while the most part of the post-processing was not included for clarity. Some quantities of interest are however added for validation purposes (the streamwise pressure gradient and the dissipations in streamwise x and cross-flow directions y, z). The reader is encouraged to run the program and compare the results obtained with those reported in table A.1.

$N_y \times N_z$	Δt	T	dP/dx	ε_u	ε_{vw}
101×101	$1 \cdot 10^{-6}$	0.20132	-44.5091	44.5066	11.43055
31×31	$1.2 \cdot 10^{-5}$	0.2013	-44.513	44.5130	11.43557

Table A.1: Comparison between two calculations at $De = 150$, the quantities reported are averaged over one time period. The coarser space (N, number of grid points) and time discretisations (third line of the table) are those used in the rest of the paper, the finer simulation is used as a benchmark. Very little differences are observed in the results: the period T varies of a quantity compatible with the dt itself, the average pressure gradient dP/dx and the streamwise and span wise dissipations ε_u,ε_{vw} exhibit very limited differences. The differences between the streamwise pressure gradient (equal to the energy injection if $U_b = 1$) and the streamwise dissipation indicate the level of convergence of the respective calculations.

The error in the oscillation period is of the same order of the time-step, the differences in the streamwise pressure gradient and streamwise and cross-stream dissipations averaged on one time period are below 5%, despite a more than ten-fold increase in the number of grid points and a 12-times finer time-step. The agreement between the average dissipation and pressure gradient in the streamwise

direction testifies the convergence of the calculations.

The simulation is initialized with the laminar solution plus a random velocity field, thus the initial transient exhibits little differences from run to run. The 'functions' file is composed by four methods, inserted in a class for practicality. The 'constBulk' method uses a bisection algorithm to iteratively calculate the streamwise pressure gradient required to maintain the target streamwise bulk velocity ($U_b = 1$ in the present paper). The 'Chebyshev' method is used to define the grid, the derivation matrices for velocity and pressure and the integration weights. The other two methods are auxiliaries for the 'Chebyshev' method. The first part of the 'main' file serves as initialization, here we define the operators for derivations and integrations in y and z, the extrapolation (c_i, d_i) and the time integration (a_1, b_i) coefficients. Finally we set the initial condition with the laminar flow solution in a straight duct ($Ulam$), with some additional random noise.

The following part is the actual time loop. In the first part we compute the right-hand-side term (explicit) of the equations, then the solution is updated for the next time-steps before calculating the new predicted velocity field. This is then corrected to enforce the divergence free condition following the prediction-projection method by Chorin and Temam. As a last step of the loop the streamwise pressure gradient is calculated using the bisection method mentioned above, and the streamwise velocity is corrected as well. The code can be copy-pasted and saved in two files: *main.py* and $functions.py$, in the same folder. Particular attention must be paid on accurately copying the indentations, which are essential in a python program. The present results were obtained by running the program on a linux machine using the Anaconda distribution of python version 3.6.4. The code also works on python 2.7 (a test was run on the Anaconda distribution of python 2.7.16).

Main

```
import numpy as np
from functions import functions_cl as ff

De=150  ;   dt=1e-5

Ny = 31; Nz = Ny
#  Chebyshev collocation method, operators definition
cc=ff()
[Y,D1,D2,Dpy,WY]=cc.Chebyshev(Ny)
Y=(1-Y)/2; WY=-WY/2; D1=D1*2
y = Y[1:-1]; Wy = WY[1:-1]; Dy = -D1[1:Ny-1,1:Ny-1]; D2y = 4*D2[1:Ny-1,1:Ny-1]; Dpy=-2*Dpy; Ay = np.dot(Dy,Dpy)
[Ey_u,Qy_u] = np.linalg.eig(D2y); invQy_u=np.linalg.inv(Qy_u);  Ey_u=(np.tile(Ey_u, [Nz-2,1])).T
[Ey_p,Qy_p] = np.linalg.eig(Ay);  invQy_p=np.linalg.inv(Qy_p);  Ey_p=(np.tile(Ey_p, [Nz-2,1])).T
Dz=np.transpose(Dy); D2z=np.transpose(D2y); Dpz=np.transpose(Dpy); Az=np.transpose(Ay);
Qz_u=np.transpose(Qy_u);  invQz_u=np.transpose(invQy_u);  Ez_u=np.transpose(Ey_u);
Qz_p=np.transpose(Qy_p);  invQz_p=np.transpose(invQy_p);  Ez_p=np.transpose(Ey_p);

d1 = 4.;d2 = -6.;d3 = 4.;d4 = -1.                           # extrapolation coefficients
c1 = 2.;c2 = -1.;c3 = 0.;c4 = 0.                            # lower order for pressure
a1 = 25/12.;b1 = -4.;b2 = 3.;b3 = -4/3.;b4 = 1/4.;sig = a1/dt  # Backward Euler

# initializing flow field
Ulam =np.dot(np.dot( Qy_u,( np.dot (  np.dot( invQy_u,(-np.ones((Ny-2,Nz-2))) ) , invQz_u)/(Ey_u+Ez_u)) ),Qz_u)
Ulam = Ulam/( np.transpose(Wy).dot(Ulam).dot(Wy) )
Px=Wy.dot(Dy[0,:].dot(Ulam))*4
uf1=np.copy(Ulam)+np.random.rand(Ny-2,Ny-2)*1e-2; uf2=np.copy(uf1);uf3=np.copy(uf1);uf4=np.copy(uf1);
vf1=np.zeros((Ny-2,Ny-2)); vf2=np.copy(vf1); vf3=np.copy(vf1); vf4=np.copy(vf1)
wf1=np.zeros((Ny-2,Ny-2)); wf2=np.copy(wf1); wf3=np.copy(wf1); wf4=np.copy(wf1)
pf1=np.zeros((Ny-2,Ny-2)); pf2=np.copy(pf1); pf3=np.copy(pf1); pf4=np.copy(pf1)

timeEnd=1   ;k=0          ;U=np.zeros((Ny,Nz))
time=[0]    ;Px_time=[0]  ;V=np.zeros((Ny,Nz))
dissip_u=[0];dissip_vw=[0];W=np.zeros((Ny,Nz))
# ------------------------
#   starting time loop
while time[-1] < timeEnd:
    k+=1
    u=d1*uf1+d2*uf2+d3*uf3+d4*uf4
    v=d1*vf1+d2*vf2+d3*vf3+d4*vf4
    w=d1*wf1+d2*wf2+d3*wf3+d4*wf4
    p=c1*pf1+c2*pf2+c3*pf3+c4*pf4
    # -----  calculating right hand side  ----- #
    rhs_u = -( b1*uf1+b2*uf2+b3*uf3+b4*uf4 )/dt +De*(-v*(Dy.dot(u)) -w*(u.dot(Dz)))
    rhs_v = -( b1*vf1+b2*vf2+b3*vf3+b4*vf4 )/dt +De*(-v*(Dy.dot(v)) -w*(v.dot(Dz)) +u**2) - Dpy.dot(p)
    rhs_w = -( b1*wf1+b2*wf2+b3*wf3+b4*wf4 )/dt +De*(-v*(Dy.dot(w)) -w*(w.dot(Dz)))       - p.dot(Dpz)
    # ---------------  update  ---------------- #
    uf4=np.copy(uf3); uf3=np.copy(uf2); uf2=np.copy(uf1);
    vf4=np.copy(vf3); vf3=np.copy(vf2); vf2=np.copy(vf1);
    wf4=np.copy(wf3); wf3=np.copy(wf2); wf2=np.copy(wf1);
    pf4=np.copy(pf3); pf3=np.copy(pf2); pf2=np.copy(pf1);
    # -------------  prediction  ------------- #
    uf1 = Qy_u.dot( (invQy_u.dot(rhs_u).dot(invQz_u)) / (sig-Ey_u-Ez_u) ).dot(Qz_u)
    vf1 = Qy_u.dot( (invQy_u.dot(rhs_v).dot(invQz_u)) / (sig-Ey_u-Ez_u) ).dot(Qz_u)
    wf1 = Qy_u.dot( (invQy_u.dot(rhs_w).dot(invQz_u)) / (sig-Ey_u-Ez_u) ).dot(Qz_u)
    # -------------  projection  ------------- #
    div = Dy.dot(vf1)+wf1.dot(Dz)
    RHSP = sig*div + Ay.dot(p) + p.dot(Az)
    pf1 = Qy_p.dot( ((invQy_p.dot(RHSP)).dot(invQz_p))/(Ey_p+Ez_p)).dot(Qz_p)
    vf1 -=  1.0/sig*Dpy.dot((pf1-p))
    wf1 -=  1.0/sig*(pf1-p).dot(Dpz)
    Px = ff.constBulk(Px,Qy_u,invQy_u,Ey_u,Qz_u,invQz_u,Ez_u,sig,Wy,rhs_u)
    uf1 = np.dot( Qy_u,( ( np.dot( invQy_u,(rhs_u-Px ) ).dot(invQz_u) )/(sig-Ey_u-Ez_u) ) ).dot(Qz_u)

    if( k % 200  ) == 0:
      time.append(k*dt) ; Px_time.append(Px)
      # ------------------------  calculating dissipation  ------------------------ #
      # ----  derivative is non zero on boundary -> adding the implicit point  ---- #
      U[1:-1,1:-1]=u;   V[1:-1,1:-1]=v;   W[1:-1,1:-1]=w
      dissip_u.append(WY.dot((D1.dot(U))**2 + (U.dot(D1.T))**2).dot(WY) )
      dissip_vw.append(WY.dot((D1.dot(V))**2+(D1.dot(W))**2+(V.dot(D1.T))**2+(W.dot(D1.T))**2).dot(WY))
      # ---------------------------------------------------------------------------- #
      divafter=Dy.dot(v)+w.dot(Dz)
      print('time: '+str('%0.3f'%time[-1])+ ' str-wise dissip:'+str('%0.3f'%dissip_u[-1])+
              ' div before/after proj: ' +str('%0.3e'%np.abs(div).max()) +'/'+
              str('%0.3e'%np.abs(divafter).max()) +' u bulk error:'+str('%0.3e'%(Wy.dot(uf1).dot(Wy)-1)))

print('average stream-wise dissipation: '+str('%0.5f'%(np.asarray( dissip_u [100:] ).mean())))
print('average stream-wise press grad : '+str('%0.5f'%(np.asarray( Px_time  [100:] ).mean())))
print('average span-wise   dissipation: '+str('%0.5f'%(np.asarray( dissip_vw[100:] ).mean())))
```

Functions

```
import numpy as np
class functions_cl:
    # ----------------------------------------
    # generation of grid and derivation matrices
    @staticmethod
    def cheb(N):
        if N == 0:
            D = 0
            x = 1
            ll=(D,x)
            return ll
        x = np.cos( np.pi*np.arange(N+1)/float(N) )
        c=np.ones(N+1)
        c[[0,-1]]=2
        c=c*(-1)**(np.arange(N+1))
        X = np.transpose(np.tile(x,[N+1,1]) )
        dX = X-np.transpose(X)
        # off-diagonal entries
        D  =  np.outer(c ,1/c) / (dX+np.eye(N+1))
        # diagonal entries
        D  = D -  np.diag(np.sum( np.transpose(D),0 ))
        return D,x
    @staticmethod
    def clencurt(N):
        # CLENCURT  nodes x (Chebyshev points) and weights w
        #           for Clenshaw-Curtis quadrature
        theta = np.pi*np.arange(N+1)/N
        w = np.zeros(N+1)
        ii = range(1,N)
        v = np.ones(N-1)
        if np.mod(N,2)==0:
            w[0] = 1./(N**2-1)
            w[N] = w[0]
            for k in np.arange (1,N/2):
              v = v - 2*np.cos(2*k*theta[ii])/(4*k**2-1)
            v = v - np.cos(N*theta[ii])/(N**2-1)
        else:
            w[0] = 1./N**2
            w[N] = w[0]
            for k in np.arange (1,(N-1)/2+1):
                v = v -    2*np.cos(2*k*theta[ii])  /  (4*k**2-1)
        w[ii] = 2.*v/N
        return w

    def Chebyshev(self,Ny):
        [Dy,y] = self.cheb(Ny-1)
        D2y = np.dot(Dy,Dy)
        Wy = self.clencurt(Ny-1)
        #Wy = ChebyshevCl.clencurt(Ny-1)
        #  see Botella, Dpy : derivative matrix without implicit BC
        c = (np.sin(  np.pi*(np.arange(1,Ny-1))/(Ny-1)    )**2) *(-1) ** np.arange(1,Ny-1)
        X = np.transpose(np.tile(y[1:Ny-1],[Ny-2,1]))
        dX = X-np.transpose(X)
        # off-diagonal entries
        D0 = np.outer((1./c),c)/(dX+(np.eye(Ny-2)))
        # diagonal entries
        Dpy = D0 - np.diag(np.sum(D0,1))
        return (y,Dy,D2y,Dpy,Wy)

    # -----------------------------------
    #   Bisection method for mean flow
    @staticmethod
    def constBulk(Px,Qy_u,invQy_u,Ey_u,Qz_u,invQz_u,Ez_u,sig,Wy,rhs_u):
        Px1=Px-.2;  uf1 = np.dot( Qy_u.dot( ( invQy_u.dot(rhs_u-Px) ) ).dot(invQz_u)/(sig-Ey_u-Ez_u) , Qz_u);
        Q1=np.dot(np.dot(Wy,uf1),Wy);
        Px2=Px+.2;  uf1 = np.dot( Qy_u.dot( ( invQy_u.dot(rhs_u-Px) ) ).dot(invQz_u)/(sig-Ey_u-Ez_u) , Qz_u);
        Q2=np.dot(np.dot(Wy,uf1),Wy);
        iter=1; Q=(Q2+Q1)/2;
        while abs(Q-1) > 1e-14:
            Px = (Px1+Px2)/2;
            uf1 = np.dot( Qy_u.dot( (invQy_u.dot((rhs_u-Px)) ).dot(invQz_u) / (sig-Ey_u-Ez_u) ) , Qz_u )
            Q=np.dot( np.dot(Wy,uf1),Wy )
            if Q>1:
                Px1=Px
            else:
                Px2=Px
            iter+=1
            if iter >=300:
                break
        return Px
```

Appendix B

The McCormack scheme

Equations (3.5) are of parabolic nature in x, we have a purely convective flow. Any perturbation is transported downstream and does not affect the upstream flow. To solve them we use a modified version of the solver described in chapter 2 that takes advantage of the method proposed by MacCormack (2003). This scheme consists in computing the solution in two steps, prediction and correction.

For simplicity we present here the solution for one of the components of the velocity field, the solution for the others is analogous, except for some terms that are not present in the equations that do not alter the application of the algorithm. The equation for v of (3.5) can be written as

$$\frac{\partial v}{\partial t} + \frac{\partial^2 v}{\partial y^2} + \frac{\partial^2 v}{\partial z^2} = u\frac{\partial v}{\partial x} + \mathcal{R} \tag{B.1}$$

The linear terms are moved on the left hand side of the equation, since they will be solved implicitely, the pressure and non linear terms are moved to the right hand side of the equation and all but the x derivative terms are lumped into the term $\mathcal{R}$ for clarity. The derivatives in the wall normal directions in $\mathcal{R}$ are performed using the Chebyshev operators (see section 2.1.5.1).

The predictor step

The tentative $\overline{v_i^{n+1}}$ solution is computed by solving the above equation. The subscripts $i, i+1$ indicate the position in the streamwise direction, the superscripts $n, n+1$ indicate the time step. The derivatives in the streamwise direction x is performed using a first order upwind Euler scheme. The time integration is computed with a first order backward Euler scheme.

The discretised equation reads

$$\frac{\overline{v_i^{n+1}} - v_i^n}{\Delta t} - \left(\frac{\partial^2}{\partial y^2} + \frac{\partial^2}{\partial z^2}\right)\overline{v_i^{n+1}} = -u_i^n \frac{v_i^n - v_{i-1}^n}{\Delta x} + \mathcal{R}^n \tag{B.2}$$

or

$$\left(-\Delta t\frac{\partial^2}{\partial y^2} - \Delta t\frac{\partial^2}{\partial z^2} + 1\right)\overline{v_i^{n+1}} = v_i^n - \Delta t\overbrace{\left(u_i^n \frac{(v_i^n - v_{i-1}^n)}{\Delta x} + \mathcal{R}^n\right)}^{\mathcal{S}^n} \tag{B.3}$$

The superscript n indicates that the terms are computed using the value at the n^{th} time-step, which is known. This equation can be solved to find $\overline{v_i^{n+1}}$.

The corrector step

In this step we correct $\overline{v_i^{n+1}}$ by solving

$$\left(-\Delta t\frac{\partial^2}{\partial y^2}-\Delta t\frac{\partial^2}{\partial z^2}+1\right)v_i^{n+1}=v_i^{n+1/2}-\frac{\Delta t}{2}\overline{\mathcal{S}^{n+1}} \tag{B.4}$$

where

$$v_i^{n+1/2}=\frac{v_i^n+\overline{v_i^{n+1}}}{2}$$

and $\mathcal{S}^{n+1}$ is the quantity $\mathcal{S}$ computed with the predicted velocities. The pressure for correction needed to enforce the divergence free condition is retrieved using the method described in section 2.1.4.1. However in this set of equation the diffusion term in x is missing, this makes the application of the method much less effective. The values of divergence do not reach machine precision, but are nonetheless kept within reasonable limits (order 10^{-6}).

Appendix C

Linear stability analysis of a weakly curved duct flow

The linear stability analyses performed in this thesis have the only objective of determining whether the flow is stable or unstable at a given Dean number. A thorough stability analysis of the flow in a toroidal pipe is provided by Canton et al. (2016). Here we use the simplest of the methods to find the most unstable mode: we solve the linearised equation for long enough times, until the most amplified (or least damped) mode emerges from the others.

The linearized equations

In order to write a linearized form of equations (3.5) we decompose the velocity field as

$$u(x,y,z,t) = U(y,z,t) + u'(x,y,z,t) \tag{C.1}$$

Where U and u' are a base flow and the fluctuations with respect to the base flow. The linearized equations read

$$\begin{aligned}
&\frac{\partial u'}{\partial x} + \frac{\partial v'}{\partial y} + \frac{\partial w'}{\partial z} = 0 \\
&\frac{\partial u'}{\partial t} + De\left(U\frac{\partial u'}{\partial x} + v'\frac{\partial U}{\partial y} + V\frac{\partial u'}{\partial y} + w'\frac{\partial U}{\partial z} + W\frac{\partial u'}{\partial z}\right) = \frac{\partial^2 u'}{\partial y^2} + \frac{\partial^2 u'}{\partial z^2} \\
&\frac{\partial v'}{\partial t} + De\left(U\frac{\partial v'}{\partial x} + v'\frac{\partial V}{\partial y} + V\frac{\partial v'}{\partial y} + w'\frac{\partial V}{\partial z} + W\frac{\partial v'}{\partial z} - 2Uu'\right) = -\frac{\partial p'}{\partial z} + \frac{\partial^2 v'}{\partial y^2} + \frac{\partial^2 v'}{\partial z^2} \\
&\frac{\partial w'}{\partial t} + De\left(U\frac{\partial w'}{\partial x} + v'\frac{\partial W}{\partial y} + V\frac{\partial w'}{\partial y} + w'\frac{\partial W}{\partial z} + W\frac{\partial w'}{\partial z}\right) = -\frac{\partial p'}{\partial z} + \frac{\partial^2 w'}{\partial y^2} + \frac{\partial^2 w'}{\partial z^2}
\end{aligned}$$

The solution of the linear problem is exponential in time, the disturbances can be expressed as

$$u'(x,y,z,t) = \sum_{j=1}^{n} U_j(y,z,t)e^{\lambda t} \tag{C.3}$$

where λ_j is the j^{th} mode, U_j is the eigenmode associated to the complex eigenvalue $\lambda_j = \sigma_j + i\omega_j$, σ_j and ω_j being the growth rate and pulsation. Due to the exponential growth of the disturbances, for large enough t the most amplified mode (or equivalently the less dampened one) will be much larger than the other ones. We exploit this to retrieve

$$\begin{aligned}\frac{\partial K}{\partial t} =& \frac{1}{2V}\frac{\partial}{\partial t}\int_V \left(u'^* u' + v'^* v' + w'^* w'\right) dV = \\ & \frac{1}{V}\int_V \left(u'^*\frac{\partial u'}{\partial t} + v'^*\frac{\partial v'}{\partial t} + w'^*\frac{\partial w'}{\partial t}\right) dV = (\sigma + i\omega)\frac{1}{V}\int_V \left(u'^* u' + v'^* v' + w'^* w'\right) dV\end{aligned}$$

Hence

$$\sigma + i\omega = \left[\int_V \left(u'^* u' + v'^* v' + w'^* w'\right) dV\right]^{-1} \int_V \left(u'^*\frac{\partial u'}{\partial t} + v'^*\frac{\partial v'}{\partial t} + w'^*\frac{\partial w'}{\partial t}\right) dV \tag{C.4}$$

where the superscript * indicates the complex conjugate. By monitoring the evolution in time of the energy, eventually we observe a stabilisation of its slope which becomes a power law, thus linear in a log-scaled plot. This indicates that the leading mode has prevailed on the others, the value of the eigenmode can be calculated from (C.4). This method is effective, but requires a control on the value of the perturbations, that are not damped by non linear effects when they grow very large. The numbers involved may go beyond the values representable in a double precision framework, and must therefore be re-normalised when they are too big (or too small).

A way of avoiding such problem is to compute not the solution for the velocity fluctuation u' (say), but instead of the eigenmode of the leading mode. Using (C.3) the time derivative of u' (which is now the eigenmode) is $(\sigma + i\omega)u'$. The time derivative is left in the equation, and will fall to zero when the calculation converges. The momentum equation for u' (e.g.) becomes

$$(\sigma + i\omega)u' + \frac{\partial u'}{\partial t} + De\left(U\frac{\partial u'}{\partial x} + v'\frac{\partial U}{\partial y} + V\frac{\partial u'}{\partial y} + w'\frac{\partial U}{\partial z} + W\frac{\partial u'}{\partial z}\right) = \frac{\partial^2 u'}{\partial y^2} + \frac{\partial^2 u'}{\partial z^2} \tag{C.5}$$

and the eigenvalue is computed as

$$(\sigma + i\omega)_{i+1} = (\sigma + i\omega)_i + \left[\int_V \left(u'^* u' + v'^* v' + w'^* w'\right) dV\right]^{-1} \int_V \left(u'^*\frac{\partial u'}{\partial t} + v'^*\frac{\partial v'}{\partial t} + w'^*\frac{\partial w'}{\partial t}\right) dV \tag{C.6}$$

with i indicating the iteration. As the simulation progresses the velocity components converge to a stationary value, thus the time derivatives both in (C.5) and (C.6) tend to zero, making the eigenvalue converge as well.

Appendix D

Compressible simulations

A preliminary study was made with the aim of computing puffs in a compressible framework. The compressible code is MUSICA, it a Fortran code based on a 10^{th} order finite difference scheme for spatial discretisation and on a six step Runge-Kutta scheme in time. For more details on the numerics see for instance Gloerfelt and Berland (2013). The puff was transferred by interpolation from an incompressible computation using a spectral interpolation method.

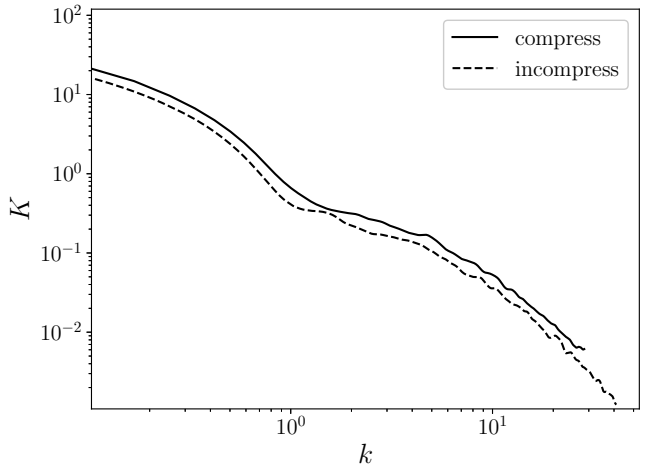

Figure D.1: cross section averaged kinetic energy spectra comparison between compressible and incompressible simulations. Puff computed on a domain of $L = 300h$, $Re = 1700$. The compressible simulation is set on $Ma = 0.3$.

The code is dimensional and based on the conservative quantities, good deal of work was devoted to obtaining a long lived puff. The computations were performed for air with reference temperature 20^oC and $Ma = 0.3$. The problems encountered were mainly given by some strong spurious fluctuations probably given by the energy component. This is linked to the pressure in the incompressible case, by supposing initially uniform temperature and density one can initialise the energy field. The field however is not a solution of the equations, the transient can produce strong perturbations that can

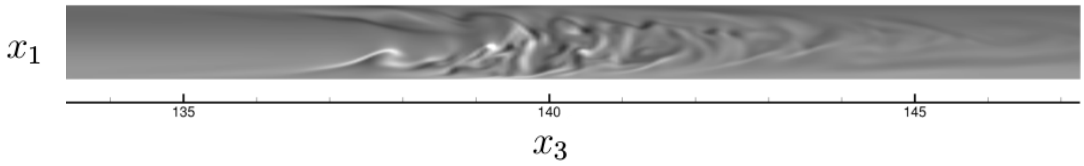

Figure D.2: Insantaneous vorticity field from a compressible simulation at $Ma = 0.3$. Puff computed on a domain of $L = 300h$, $Re = 1700$.

easily kill the puff. The artificial dissipation needed to be finely adjusted, a too strong value eventually resulted in a relaminarisation, whereas with too little dissipation the computation diverged. The viscosity was kept constant. The grid was composed of $128 \times 128 \times 5880 \sim 96 \cdot 10^6$ points for a domain length of $300h$. Figure D.1 shows a comparison between the kinetic energy streamwise wavenumber spectra computed with the compressible and incompressible codes. The compressible result was non-dimensionalised *a posteriori*. The agreement is good, a slightly higher frequency change in slope is observed for the compressible case. The vorticity field in figure D.2 looks very much the same as that shown for instance in figure 2.4, computed with an incompressible formulation.

Leonardo RIGO

Turbulent puffs in square duct flow: acoustic radiation and effects of curvature

Résumé : L'apparition de la turbulence dans une conduite à faible nombre de Reynolds se localise sous la forme de *puffs* turbulents. Dans la littérature, les *puffs* sont classiquement étudiés dans des conditions nominales, qui correspondent à un écoulement incompressible dans une conduite droite de section circulaire. Cette thèse vise à étudier l'influence de faibles variations par rapport à ces conditions nominales. En particulier, on considère une conduite de section carrée et on introduit une faible courbure d'une part et on étudie le rayonnement acoustique d'autre part. Dans une première partie les caractéristiques du *puff* dans une conduite carrée sans courbure et sans effet de compressibilité sont présentées. Dans une seconde partie, les effets de courbure sont analysés à partir d'un modèle d'équations obtenu par une analyse dimensionnelle. Le modèle est validé pour des écoulements laminaires; les comparaisons par rapport à des données numériques et expérimentales de la littérature sont satisfaisantes. Le *puff* turbulent est calculé en utilisant deux systèmes d'équations couplés basés sur une séparation d'échelles. Les caractéristiques du *puff* turbulent sont qualitativement en accord avec les données publiées. Enfin, le bruit en champ lointain généré par le *puff* est calculé à l'aide d'une analogie acoustique, ce qui permet d'exclure un rôle possible de l'acoustique dans l'interaction à grande échelle entre les *puffs*. Cette étude fournit par ailleurs des résultats sur le rôle des contraintes visqueuses dans la génération de bruit. Cette configuration est en effets un cas très bien posé, car les effets des composantes visqueuses sur l'acoustique sont mieux visibles à faibles nombres de Mach et de Reynolds.

Mots clés : puff turbulent, intérmittence, aéroacoustique, canal courbé

Abstract : The first occurrence of turbulence at low Reynolds number in pipe flows takes the form of streamwise localised patches named turbulent puffs. In the literature puffs are usually studied in the nominal conditions of incompressible flow in straight circular pipes. This thesis aims at investigating the influence that slight deviations from those nominal conditions have on puffs computed in a square duct configuration. For this purpose we introduce a slight curvature of the pipe on the one hand and we analyse the acoustic field of the puff on the other hand. Curvature effects are analysed by means of a laminar model obtained as an extension of the work by Dean. This model is validated against numerical and experimental literature data, providing satisfactory results. The turbulent puff in a curved pipe is computed with an additional set of equations based on scale separation, the curvature effects on turbulence are in qualitative agreement with the data available in the literature. The far-field noise field generated by a puff is computed by means of an acoustic analogy, in addition to characterising the acoustic field produced, this analysis excludes a role of acoustics in a hypothetical long range interaction between puffs. Moreover this study provides some elements to the literature concerning the role of the viscous stresses to the sound generation. This configuration provides a very well posed case for such analysis, since the effects of viscous stresses on acoustics are most visible at low Mach and Reynolds numbers.

Keywords : turbulent puffs, intermittency, aeroacoustics, curved duct